

Mechanical Properties of Complex Biological Systems
using AFM-Based Force Spectroscopy

A Dissertation presented to
the Faculty of the Graduate School
University of Missouri-Columbia

In Partial Fulfillment
Of the Requirements for the Degree
Doctor of Philosophy

By
John Stephen Graham

Dr. Henry White, Dissertation Supervisor

December 2005

The undersigned, appointed by the Dean of the Graduate School, have examined the dissertation entitled:

MECHANICAL PROPERTIES OF COMPLEX BIOLOGICAL SYSTEMS
USING AFM-BASED FORCE SPECTROSCOPY

Presented by John Stephen Graham

A candidate for the degree of Doctor of Philosophy

And hereby certify that in their opinion it is worthy of acceptance.

Henry W. White


Pete Pfeife

Michael V. Henzl





ACKNOWLEDGEMENTS

I would like to thank the following people for their various contributions to this work (in no particular order): Dr. Charlotte L. Phillips, Dr. Anthony N. Vomund, Sam Potts, Mingzhai Sun, Wonchul Shin, Dr. Balazs Hegedus, Dr. Gabriel Hosu, Karoly Jakob, Dr. Gabor Forgacs, Ying Zhang, Yannick Miron, Dr. Cora-Jean Edgell, Chris Martin, Stephanie Robinson, Sherry Long, Pauline Baron, my committee: Dr. Henry White, Dr. Shi-Jei Chen, Dr. Gabor Forgacs, Dr. Michael T. Henzl, Dr. Peter Pfeifer and Dr. Michel Grandbois.

ABSTRACT

An atomic force microscope (AFM) was designed and built to study the mechanical properties of small collagen fibrils and the plasma membrane of living cells. Collagen is a major component of bone, skin and connective tissues, and is abundant in the extracellular matrix (ECM). Because of its abundance, an understanding of how disease affects collagen mechanics is crucial in disease prevention efforts. Two levels of type I collagen structure were investigated, subfibrils (on the order of 1 μm in length) and longer fibrils. Comparisons were made between measurements of wild-type (wt) collagen and collagen from the mouse model of osteogenesis imperfecta (OI). Significant differences between OI and wt collagen were observed, primarily that intermolecular bonds in OI collagen fibrils are weaker than in wt, or not ruptured, as in the case of OI subfibrils. As cells interact with collagen in the ECM, the mechanical properties of the plasma membrane are also of great interest. Membrane tethers were extracted from living cells under varied conditions in order to assess the contributions of membrane-associated macromolecules such as the actin cytoskeleton and the glycocalyx, and intracellular signaling. Tether extraction force was found to be sensitive to all of these altered conditions, suggesting that tether extraction may be used to monitor various cellular processes.

LIST OF ILLUSTRATIONS

Figure		Page
1.1	AFM detection methods.....	2
1.2	AFM cantilever geometry.....	4
1.3	Force device illustration.....	6
1.4	Power spectrum analysis method.....	8
1.5	Example results of data filtering techniques.....	11
1.6	Examples of power spectrum filtering.....	12
1.7	Images of cellular scaffolding.....	15
1.8	Schematic of freely jointed chain definition.....	16
1.9	Schematic of wormlike chain definition.....	20
1.10	Schematic of polymer brush.....	26
1.11	Example polysaccharide force profiles.....	27
1.12	Illustration of B and Z DNA helices.....	28
1.13	Example DNA force profile.....	30
1.14	Illustration of protein secondary structures.....	31
1.15	Example protein force profile (titin).....	32
2.1	Collagen assembly hierarchy.....	39
2.2	Collagen monomer and <i>D</i> -stagger.....	40
2.3	Collagen banding pattern and AFM scan of fibril.....	40
2.4	Collagen microfibril structure.....	41

2.5	Covalent cross-links in collagen.....	43
2.6	Axial charge distribution in collagen <i>D</i> -period.....	44
2.7	AFM scan of acid-solubilized collagen.....	46
2.8	AFM scans of reconstituted collagen fibrils.....	48
3.1	Macroscopic collagen fiber force profile.....	54
3.2	AFM scans of gap stretching in collagen fiber.....	55
3.3	Force profiles of model human collagen subfibrils.....	58
3.4	Force profile of peeling collagen fibrils from substrate...	60
3.5	Measurement of discrete extensions in force profile of model human collagen subfibril.....	60
3.6	Stress-strain curve of model human collagen subfibril...	67
3.7	Force profiles of mouse-tail collagen subfibrils.....	69
3.8	Force profiles of mouse-tail collagen fibrils.....	72
3.9	Measurement of discrete extensions in force profile of mouse-tail collagen fibrils.....	72
3.10	Axial charge distributions in collagen <i>D</i> -period: comparison of OIM and wildtype collagen.....	73
3.11	Structure of [tris(hydroxymethyl)phosphine]-alanine....	81
3.12	AFM scans of nodes in gold-collagen mesh.....	82
3.13	AFM scan of folds in gold-collagen mesh.....	83
3.14	AFM scans of dense gold-collagen mesh.....	86

4.1	Schematics of plasma membrane and extraction of membrane tethers with an AFM.....	91
4.2	Example force profile of tether extraction.....	98
4.3	Fluorescence image of tether extraction with an AFM....	98
4.4	Force profiles of tether extraction with forces.....	100
4.5	Schematic of labeled tether extraction geometry.....	102
4.6	Constant extension force-time data of tether extraction.....	105
4.7	Plot of time versus relaxation rate of constant extension data.....	105
4.8	Force profiles of tether extraction at 1000nm/sec.....	107
4.9	Example of membrane reservoir size measurement.....	112
4.10	Schematic of membrane leaflet slippage due to tether extraction.....	115
4.11	Schematic of general tether extraction geometry and equilibrium position.....	115
4.12	Histogram of tether force for untreated cells.....	117
4.13	Schematic of effect of latrunculin and hyaluronidase treatment on cells.....	118
4.14	Histogram of tether force for latrunculin treated cells.....	118

4.15	Histogram of tether force for hyaluronidase treated cells.....	119
4.16	Schematic of a likely tether extraction geometry for an AFM experiment.....	122
4.17	Multi-peak histograms of tether extraction forces.....	124
4.18	Average force versus time plot for thapsigargin treatment.....	130
4.19	Histogram of tether forces after thapsigargin treatment at 37 °C.....	131
4.20	Plot of force versus point number demonstrating random fluctuations in tether forces for thapsigargin treated cells.....	132
4.21	Histogram of tether forces after thapsigargin treatment at 25 °C.....	133

LIST OF TABLES

Table	Page
1.1.....	24
4.1.....	111

TABLE OF CONTENTS

ACKNOWLEDGEMENTS.....	ii
ABSTRACT.....	iii
LIST OF ILLUSTRATIONS.....	iv
LIST OF TABLES.....	viii
Chapter	
1. AFM and Force Spectroscopy Background.....	1
1.1 AFM Development.....	1
1.2 The Force Device.....	6
1.3 Force Spectroscopy.....	13
1.3.1 Motivation for Force Spectroscopy.....	13
1.3.2 Models of Polymer Mechanics.....	16
1.4 Manipulations of Biological Macromolecules and Results.....	24
1.4.1 Investigation of Polysaccharides with AFM.....	25
1.4.2 Investigation of Nucleic Acids with AFM, Laser Tweezers & Magnetic Tweezers.....	28
1.4.3 Investigation of Proteins with AFM & Laser Tweezers.....	31
1.4.4 Introduction to FS Studies of Collagen.....	33

2. Review of Collagen Biochemistry and in vivo Mechanics...	35
2.1 Role of Collagen in Bone, Connective Tissues and Diseases.....	35
2.2 Collagen Structure (including cross-linking).....	38
2.2.1 Overview of Structure.....	38
2.2.2 From Monomers to Subfibrils.....	42
2.2.3 Cross-Linking.....	43
2.2.4 In Vitro Production of Collagen Fibrils.....	46
2.2.5 Materials and Methods.....	50
3. Mechanical Properties of Collagen Fibrils.....	52
3.1 Force Spectroscopy Studies of Collagen Fibrils.....	52
3.1.1 Background.....	52
3.1.2 Force Spectroscopy of Model Human Type I Collagen Subfibrils.....	56
3.1.3 Comparison of Wildtype and OIM Mouse Tail Collagen Subfibrils and Fibrils.....	68
3.1.4 Summary of Fibril Stretching Results.....	75
3.2 Exploiting Collagen Mechanics in the Production of a Self-Assembled Material.....	77
3.2.1 Motivation and Background.....	77
3.2.2 Materials and Methods.....	79
3.2.3 Characterization of the Nanomaterial.....	80

4. Cell Membrane Mechanics: The Effect of the Glycocalyx and Intracellular Processes.....	89
4.1 Motivation and Background.....	89
4.1.1 Materials and Methods.....	96
4.1.2 Formation and Dynamics of Membrane Tethers.....	97
4.2 Influence of the Cytoskeleton, the Glycocalyx and Intracellular Signaling on Tether Formation.....	114
4.2.1 Tether Forces, the Cytoskeleton and the Glycocalyx.....	114
4.2.2 Summary: Overview of Tether Dynamics.....	126
4.2.3 Tether Force Measurement: Application to Monitoring Intracellular Processes.....	128
References.....	136
Vita.....	164

CHAPTER 1:

AFM and Force Spectroscopy Background

1.1 AFM Development

The original atomic force microscope (AFM) was developed in 1985 by Binnig, Quate and Gerber [1] in answer to a call for greater versatility in atomic scale imaging. Falling on the heels of the development of the scanning tunneling microscope (STM) that relied on electron tunneling between the surface and the probe, the AFM was developed to allow atomic scale imaging of non-conducting surfaces without modification

of the sample surface. While other powerful techniques were available for small-scale surface imaging¹, their lateral and vertical resolutions were low and highly coupled. An investigator was therefore required to sacrifice resolution in one dimension to obtain reasonable resolution in the other. The AFM significantly reduced the coupling, allowing finer resolution in both dimensions.

Using the common method of measuring the displacement of a spring of known force constant to determine an applied force, the original AFM was a modification of the STM. A gold-foil lever of low force constant with a diamond tip was used to allow maximum deflection at a given force. Since the STM tip could register changes in position of 10^{-4} Å, it was a good choice for measuring the deflection of the lever (Figure 1.1A). Attachment of piezoelectric actuators to the

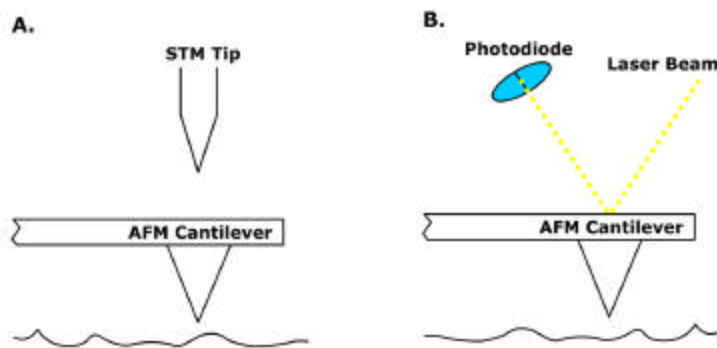


Figure 1.1.
A. Schematic of the original AFM detection method showing the STM tip as the detector.
B. Schematic of the optical lever method of detecting cantilever deflection.

¹ These are the stylus profilometer (1000Å lateral and 10Å vertical resolution) and the scanning capacitance microscope (5000Å lateral and 2Å vertical resolution). See [1] and references 8-11 therein.

sample stage, lever and STM probe allowed several modes of operation. All modes operated on the same principle, using a feedback loop to maintain a constant force between the diamond tip and the sample. Considering the amplitude of the noise and the thermal drift in the data, Binnig et al estimated a possible lateral resolution between 1 and 100Å and a vertical resolution of less than 1Å, a 10-fold increase in resolution from the other known techniques.

Contemporary AFMs operate on the same principle of maintaining constant force between the tip and the sample, although the method of detection has been simplified considerably [2]. Cantilever deflection is now measured using the optical lever method, in which the STM tip is replaced by a laser beam that is reflected from the back of the cantilever onto a two or four-sector photodiode [3] (Figure 1.1B). Changes in voltage registered by the photodiode are used to determine the force applied to the surface and to supply the feedback loop. The feedback loop now maintains a constant force by controlling a single piezoelectric element, either modulating the sample position or the position of the cantilever. This major advance significantly reduced drift and sensitivity to thermal fluctuations, thereby enhancing resolution. Advances in microfabrication techniques have also improved resolution by allowing for better control of the

resonance frequencies of the cantilevers [4, 5]. For a rectangular cantilever, the resonance frequency is given by:

$$f = C\sqrt{\frac{k}{m}}, \quad (1.1)$$

where C is a material and size-dependent constant, k is the cantilever force constant and m is its mass [6]. Ideally, a cantilever with a high resonance frequency is desired to eliminate noise from thermal and mechanical disturbances. A balance must be maintained between the force constant and the mass of the cantilever to control the signal to noise ratio [6]. The majority of cantilevers in use today are made from silicon nitride (Si_3N_4), which has a lower density and higher rigidity than the original gold cantilever [4]. This allows for manufacture of cantilevers with low mass and force constant and relatively high resonance frequencies. Today, the most commonly used cantilevers are triangular (Figure 1.2). The triangular design was conceived in order to reduce torsional effects as the cantilever is moved across the

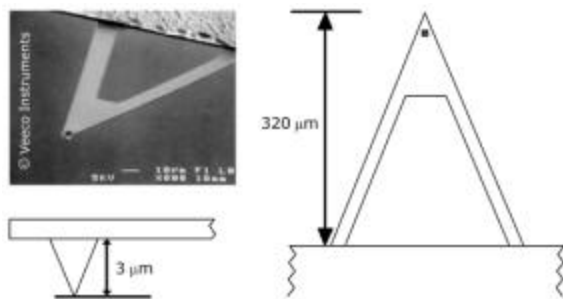


Figure 1.2. Electron micrograph of a triangular cantilever. Schematics show the length and tip height of the most frequently used cantilever. *Micrograph used with permission of Veeco Instruments.*

surface [7], although it has recently been suggested that this design may actually promote torsional effects [8]. Cantilevers with force constants as low as 0.006N/m are currently available allowing piconewton-scale forces to be probed [9]. These advances extend the utility of the AFM to the probing of biological systems, which are often soft structures requiring low contact force for topographical imaging.

A typical AFM study requires no surface modification, such as the preparation of a conducting surface for electron microscopy or STM, since the sample is probed through mechanical contact. With the optical lever detection method, biological systems may be scanned in aqueous solution approximating physiological conditions. While this was attempted using the STM probe detector, it was found that the fluid environment adversely affected the tunneling current [10]. Under ambient conditions, the sample and cantilever surfaces have layers of hydration through which meniscus forces cause the tip to adhere to the sample [11]. These capillary forces prevent the setpoint² from being properly minimized adversely affecting resolution. In aqueous solution, the capillary forces essentially disappear, offering an added advantage to the fluid AFM technique. Images of enzymatic activity on lipids [12], functioning membrane proteins [13], surface-adsorbed

² The setpoint is the desired value of the constant force between the cantilever tip and the surface.

fibrillar proteins [14, 15] and surface-adsorbed DNA [16] and RNA[17] have been produced with the AFM. While topographical imaging is extremely useful for characterization of biological systems, it is limited in what it can reveal. It was realized that there were significant opportunities available by changing the operating mode of the AFM. The approach was to operate the AFM in a one-dimensional mode normal to the surface to probe the binding strengths and mechanical properties of biological systems [18]. This mode of operation has come to be called force spectroscopy.

1.2 The Force Device

Most commercially available AFM's are designed for scanning in the x-y plane and are difficult to operate in force mode. For this reason, we had to design a custom device to function only in force mode. It consists of an aluminum body with a 1-D piezoelectric actuator near

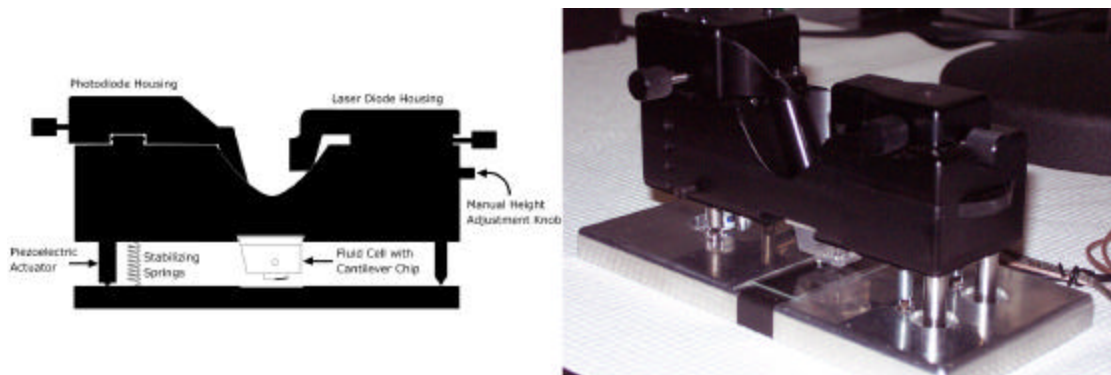


Figure 1.3. Labeled schematic of the force device (left) and a photograph (right).

one end that acts as a lever to lift the device away from the surface (Figure 1.3). The position of the piezoelectric actuator within the body is adjustable allowing for a wide variation in sample height. Near the other end are two manually adjustable "feet" that serve as the pivot point for the device while in operation. The laser and photodiode housings are mounted on adjustable x-y micro stages that confine the housings to the horizontal plane. Restricting the motion of the photodiode and laser to the horizontal ensures that the laser beam is confined to the vertical plane and that the photodiode remains perpendicular to the beam path. This arrangement helps to eliminate noise from stray laser light due to the beam striking the cantilever and photodiode at oblique angles. Further reduction of noise was accomplished by replacing the AC laser diode with a DC diode. This modification eliminated the need for an external laser driver reducing the number of devices driven by the 60 Hz power supply.

Since the force device was custom built in our lab, the control and acquisition software had to be developed as well. Computer interface hardware for custom applications is available through companies such as National Instruments. Ultimately, a practical

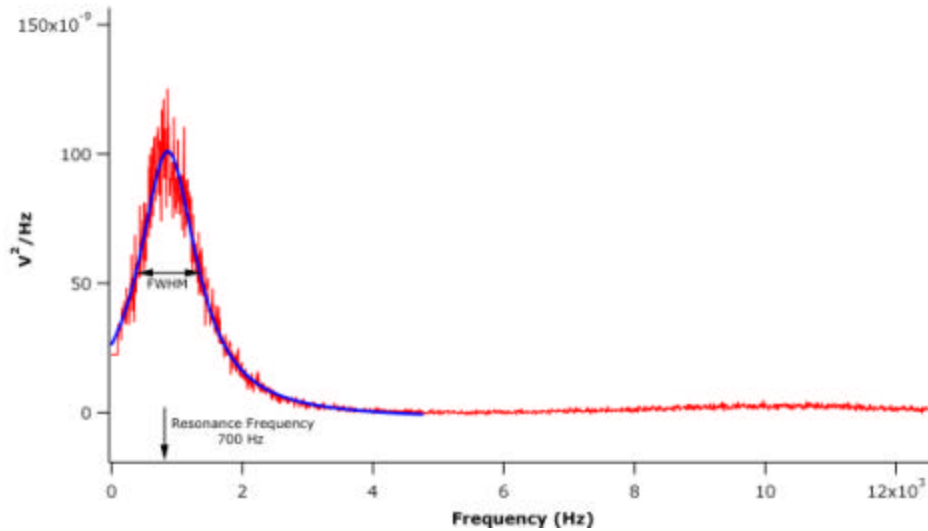


Figure 1.4. Example of a resonance peak in the power spectrum of a typical AFM cantilever. A Lorentzian fit and the parameters for determining the Q -factor are shown.

computer interface system relies on the software. The control and data acquisition program was designed using National Instruments' LabView software. This software allows the development of control programs with a user-friendly interface and the ability to easily modify the program for evolving applications and environmental factors influencing the noise level in the acquired data.

One environmental factor influencing noise levels is the noise due to the electronics of the control hardware. Electronic noise is primarily an obstacle while attempting to calibrate the cantilever. To calibrate the cantilever, it is necessary to determine the thermal energy of its natural fluctuations and obtain information allowing the conversion of voltage data to force data. The thermal energy data is obtained by recording the power spectrum of the cantilever's thermal

fluctuations [19]. Within the power spectrum will be a peak centered on the natural frequency of the cantilever (700Hz in liquid for the most commonly used cantilever; Figure 1.4). The area under the resonance peak gives the power of the cantilever fluctuations in units of V^2 that then must be combined with data relating voltage to extension. A voltage-extension ratio is obtained by recording a voltage-extension curve using a surface with higher rigidity than the cantilever (Figure 1.5A). This data is primarily affected by the noise due to the thermal fluctuations of the cantilever, which can be reduced by applying a lowpass filter to the signal (Figure 1.5B). The slope of the segment of the curve representing the deflection of the cantilever will give a value in Vm^{-1} that, in combination with the power spectrum area, can be used to determine the force constant for the cantilever [19-21]:

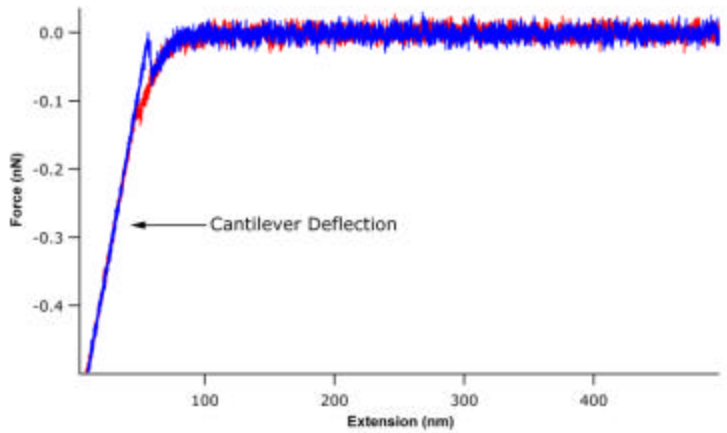
$$k = 0.8k_bT \frac{slope^2}{Q \times area} \quad (1.2)$$

where k_bT is the Boltzmann factor and Q is the quality factor, or simply Q -factor. The Q -factor is typically found as a parameter of the simple harmonic oscillator model (SHO) and is a measure of system damping that will account for coupling of the modes of cantilever vibrations. A fit of spectral data is used to determine the Q -factor, which is defined as the resonance frequency divided by the full width

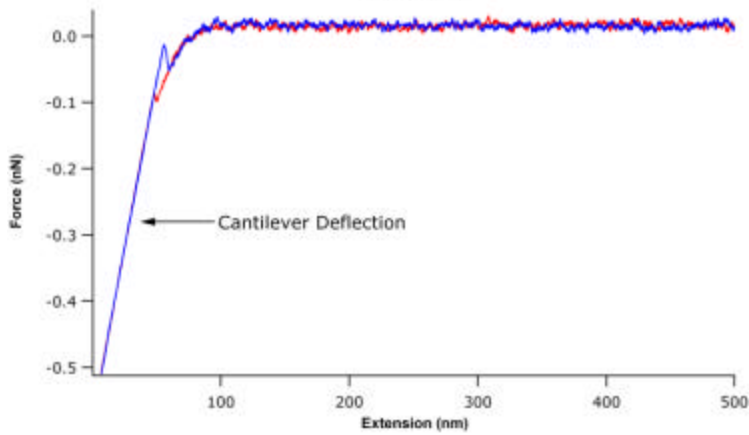
at half maximum (Figure 1-4). For the most frequently used cantilever, the resonance frequency in liquid is 700Hz, and the low frequency extremes of the spectrum are cut off. This truncation renders the SHO extremely difficult to use and, since the Q -factor is often of order 1, an unsatisfactory model [20]. For this reason, the spectra are fit to a Lorentzian in order to obtain the Q -factor (Figure 1-4), and the area is then determined directly from the data rather than the fit.

Further difficulties arise in analyzing the resonance peak when the noise levels are high (Figure 1.6A), and it may even be impossible to identify the peak. Application of a highpass filter will facilitate identification of the resonance peak by reducing the size of the low frequency spike (Figure 1.6B). Even with this improvement, electronic noise introduces transient spikes, visible in each panel of figure 1.6, that can only be eliminated by minimizing the necessary control electronics (Figure 1.6C bottom curve). High quality hardware filters with versatile frequency control can be extremely expensive and are complicated to construct. Simple hardware filters have limited control capabilities allowing for little flexibility in their application. Elimination of the hardware lowpass and highpass filters by replacing them with a digital software filter allows for simplification of the control circuitry.

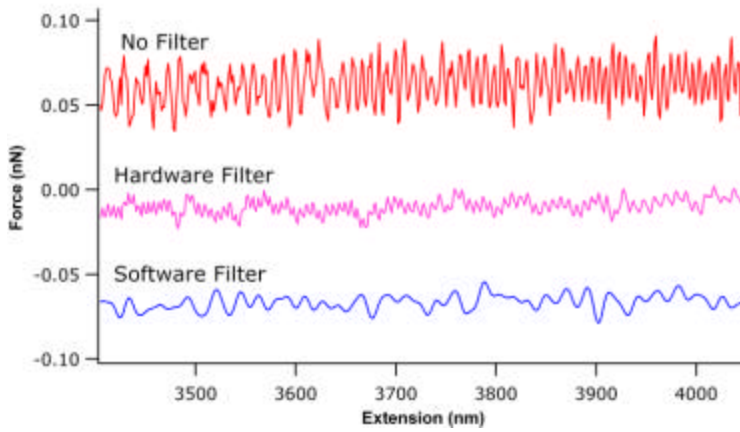
Figure 1.5.



A. Example of deflection data with no filtering.



B. Example of deflection data with hardware filtering.



C. Example comparing unfiltered and filtered data.

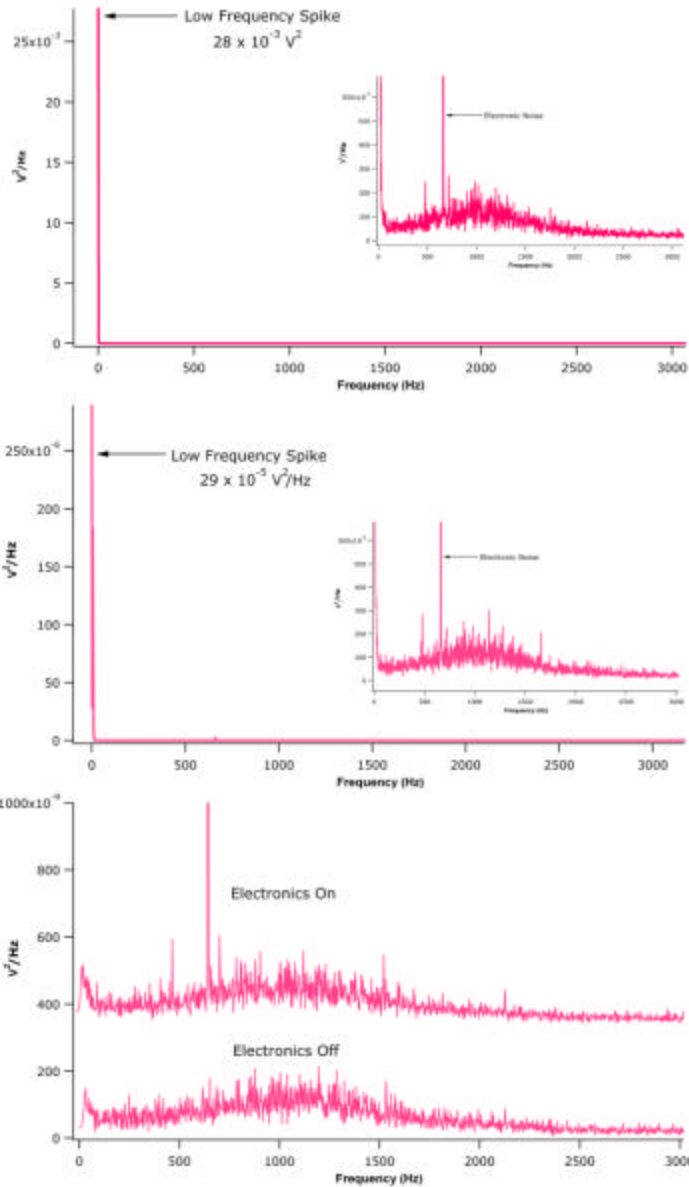


Figure 1.6.

A. Example power spectrum with no filtering. Inset is an enlargement of the spectrum from 0 to 3000 Hz.

B. Example power spectrum data using the hardware filter. Notice the resolution is better but still quite low. Inset is an enlargement of the spectrum from 0 to 3000 Hz.

C. Example power spectra using digital software filter. Note the absence of the low frequency spike and the spikes due to the electronics.

Digital software filters increase the signal-to-noise ratio and provide greater control over the filtering frequency, so that the filter may be tailored to meet the needs of the specific experiment. Figure 1.6C shows the result of the digital highpass filter demonstrating the elimination of the low frequency spike and the improved resolution of the power spectrum resonance peak. The result of applying the lowpass filter (in an extreme manner) to the data signal is shown in figure 1.5C. Since the information desired in an experiment occurs at low frequencies and the lowpass filter only targets high frequencies, it is clear that prudent application of the digital filter will facilitate identification of intramolecular events occurring at forces closer to the limit of resolution governed by the intrinsic mechanical properties of the cantilever.

1.3 Force Spectroscopy

1.3.1. Motivation for Force Spectroscopy

Biological systems are extremely complex, dynamic and constantly interacting with their immediate environment. Many of these interactions involve binding of molecules at interfaces between various compartments. Force spectroscopy (FS) has been used to probe

several specific binding interactions. Work has included the probing of red blood cells [22], integrin-fibronectin interactions [23] and the binding forces of cadherins [24]. These interactions are dynamic and have a specific *in situ* role. Macromolecular constituents of the cytoskeleton as well as components of the extracellular matrix (ECM) possess mechanical properties that serve to regulate interactions between the more active components. Any or all of the cytoskeletal and ECM components may become damaged by disease and fail to perform their natural functions resulting in tissue failure and possibly premature death of the organism. Investigations of bulk tissues have provided a large body of information regarding the mechanical properties of connective tissues. The importance of tissue studies should not be underestimated, but the bulk mechanical properties of tissue studies do not provide significant insight into the intrinsic mechanical properties of the individual components. Much as the mechanical properties of each component used in the construction of a building need to be known in order to produce a sturdy structure, characterization of the mechanical properties of each tissue component is needed to understand the origin of the macroscopic properties. There are many biological macromolecules with structural and

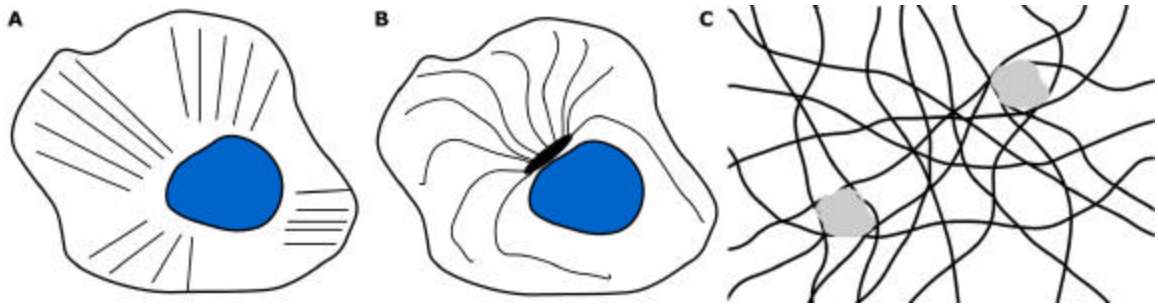


Figure 1.7. Confocal microscopy images of fluorescently labeled **A.** the actin cytoskeleton, **B.** the microtubule network and **C.** a collagen matrix with two cells embedded (white spots). [25]

mechanical roles in both the cytoskeleton and the ECM. All of these macromolecules warrant investigation via force spectroscopy.

The primary components of the cytoskeleton and ECM are large polymeric structures. The cytoskeleton contains actin filaments and microtubules composed of tubulin [26] that provide support, aid cellular motility and facilitate intracellular transport (Figure 1.7A&B). Both actin and tubulin have been investigated using AFM-based techniques [27-29]. The ECM contains polymeric structures such as hyaluronic acid, fibronectin and collagen, each of which imparts structural and/or mechanical properties to tissues [30] (Figure 1.7C). The theoretical investigation of polymer mechanics has a long history that has led to well-developed mechanical models of polymer dynamics.

1.3.2. Models of Polymer Mechanics

There is an extensive theoretical literature regarding the physical properties of polymers from which two primary models of polymer elasticity have emerged. Each model assumes different dynamics for the polymer chain; the freely jointed chain (FJC) assumes the polymer to be a chain of rigid rods connected by freely rotating joints, and the wormlike chain (WLC) approaches a uniform flexibility over the length of the polymer.

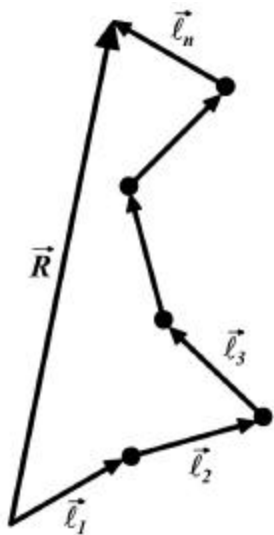


Figure 1.8. Schematic of the freely jointed chain model, with the end-to-end vector \vec{R} and Kuhn vectors $\vec{\ell}$.

The Freely Jointed Chain (FJC)

The FJC is a model based on the random walk problem [31]. The model assumes the polymer is composed of a number N , of rigid segments of length ℓ (figure 1.8). Representing each segment as a

vector $\vec{\ell}$ independently oriented in an external field \vec{F} leads to the mathematical starting point for the model, the Langevin function which is often presented as a description of independently oriented magnetic dipoles in an external field [32, 33]:

$$\Lambda(a) = \coth(a) - \frac{1}{a} . \quad (1.2)$$

The influence of the external field defines the argument a :

$$a := \frac{\vec{F} \cdot \vec{\ell}}{kT} , \quad (1.3)$$

with \vec{F} being the force experienced by the polymer and kT the Boltzmann factor. To formulate the model the average end-to-end distance, \vec{R} , is considered, where $\vec{R} = \sum_{n=1}^N \vec{a}_n \vec{\ell}_n$. The average extension s

in terms of the Langevin function is given as:

$$s = n\ell\Lambda(a) , \quad (1.4)$$

and is a description of the degree of entropy of the chain. The FJC model was formulated as a general model of the fluctuations of polymers in solution. The application of force spectroscopy essentially constrains the system to one dimension so that the vector notation may be dropped. Furthermore, for the case where $n \ll N$, the leading term in (1.4) becomes $N\ell = L$, the full 1-D length of the chain called the contour length. The contour length is an important parameter as it

is the intrinsic property most readily extracted from experimental data.

With this simplification, the practical FJC model becomes:

$$s = L \zeta \coth \zeta \frac{F \ell}{kT} - \frac{kT}{F \ell} \zeta^{-3}. \quad (1.5)$$

For historical reasons, ℓ is called the Kuhn length and it is the largest statistically independent segment of the chain. In 1942, Kuhn and Grun described the FJC model in terms of the excluded volume effect in which the long-range interactions of individual segments are considered [34]. Here, "long-range" refers to the separation of the segments along the 1-D chain rather than in higher-dimensional space, and the excluded volume effect accounts for the fact that each segment occupies a volume of space and other segments are forbidden to enter that space. Importantly, the Kuhn segment does not necessarily refer to a monomer in the chain. For instance, a polymer may have two adjoining monomers that are prevented from moving independently due to steric considerations, in which case the dimer may be the Kuhn segment. While the FJC model assumes each Kuhn segment to be rigid, in reality the bonds between the atoms are elastic. In the early to middle 1990's the model was extended to account for bond elasticity.

First proposed in 1992 [35] and realized in 1996 [36] the modified FJC model considers the extensibility of the Kuhn segments:

$$l\mathbf{C} = l + \frac{F}{k_{seg}}, \quad (1.6)$$

where $l\mathbf{C}$ is the extended Kuhn segment, F is the force applied to extend the segment and k_{seg} is the elasticity, or force constant, of a Kuhn segment in N/m. The ratio F/k_{seg} is the additional extension beyond the entropic regime. If n Kuhn segments are stretched, equation 1.6 becomes:

$$nl\mathbf{C} = nl + \frac{nF}{k_{seg}}. \quad (1.7)$$

Recalling that nl becomes the contour length, L , in the limit in which all Kuhn segments are counted, the Kuhn segment extension can be written:

$$L\mathbf{C} = L + \frac{nF}{k_{seg}}. \quad (1.8)$$

Substituting equation 1.8 for L in equation 1.5, the extended FJC model is obtained [37]:

$$s = \frac{\mathbf{C}}{\mathbf{C}} \coth \frac{\mathbf{C}}{\mathbf{C}} \frac{\mathbf{C}}{\mathbf{C}} \frac{F l \mathbf{C}}{k T \mathbf{C}} - \frac{k T \mathbf{C}}{F l \mathbf{C}} L + \frac{n F \mathbf{C}}{k_{seg} \mathbf{C}}. \quad (1.9)$$

Incorporated explicitly in this model is the elasticity of a single Kuhn segment. This segment elasticity can be reconciled with macroscopic parameters such as the Young's modulus by defining a "stretch" modulus of the entire chain as $E = YA$, where Y is Young's modulus and A is the cross-sectional area. Realizing that the segment elasticity is just $k_{seg} = E/\ell$, the original presentation of the extended FJC model is recovered [36]:

$$s = L \left[\frac{F \ell}{kT} \coth \left(\frac{F \ell}{kT} \right) - \frac{kT}{F \ell} \right] + \frac{F \ell}{E} \quad (1.10)$$

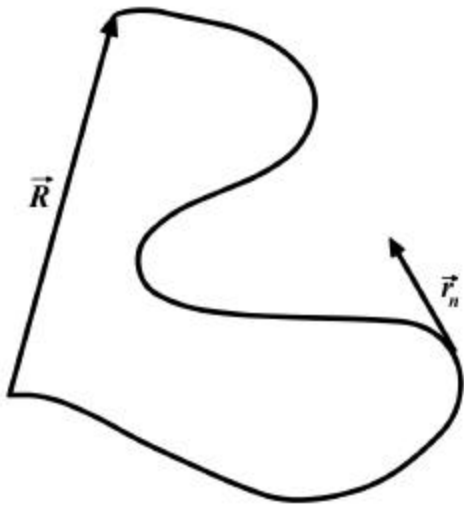


Figure 1.9. Schematic of the wormlike chain model, with end-to-end vector \vec{R} and tangent vectors \vec{r}_n .

The Wormlike Chain (WLC)

As with the freely jointed chain, the wormlike chain considers the end-to-end distance \vec{R} , with the difference that it is here the sum of

vectors \vec{r} tangent to the chain (Figure 1.9). Also considered here is an extension s and unit tangent vectors are defined as:

$$\vec{u}(s) = \frac{d\vec{r}}{ds}. \quad (1.11)$$

The conformation of the WLC is defined in terms of the Boltzmann distribution of the bending energy $U(\vec{u}(s))$ [38]:

$$Y(\vec{u}) = \exp\left[-\frac{U(\vec{u})}{kT}\right] = \exp\left[-\frac{1}{2} p \int_0^L ds \frac{d\vec{u}}{ds} \cdot \frac{d\vec{u}}{ds}\right], \quad (1.12)$$

where kT is the Boltzmann factor and:

$$p = \frac{E}{kT}, \quad (1.13)$$

is called the persistence length after Kratky and Porod who developed the model in 1949 [39]. The persistence length is defined as the longest segment below which the chain can be considered a rigid rod. This becomes clear by considering the flexural rigidity E in equation (1.13), and noting that the more rigid a polymer, the longer its persistence length will be. It is important to realize that the persistence length is not the same as the Kuhn length but is directly related by $2p = \ell$, where ℓ is the Kuhn length as above [40]. The relationship between p and ℓ can be readily deduced by comparing

the definitions of the rms polymer length for the FJC and WLC models.

For the FJC the rms length is [41]:

$$\langle r^2 \rangle = n\ell^2 \quad (1.14)$$

where in the limit $n \gg N$, $N\ell = L$ and the Kuhn length can be defined as:

$$\frac{\langle r^2 \rangle}{L} = \ell. \quad (1.15)$$

For the WLC, the ratio (1.15) is:

$$\frac{\langle r^2 \rangle}{L} = 2p \left[1 - \frac{p}{L} \left(1 - e^{-L/p} \right) \right] \quad (1.16)$$

and assuming a long polymer chain in which $L \gg p$, the right-hand side of (1.16) is simply $2p$. Equating (1.15) and (1.16) gives the expected result, $2p = \ell$. This basic relationship suggests that the models are linked in a more fundamental way. Indeed, it was shown that both the FJC and the WLC models can be derived from the freely rotating Gaussian chain [42]. This entropic model is the most commonly used and was first described in closed form in 1982 [43]. The first application to force-extension experiments was in 1994 by

Bustamante et al [44] in the asymptotic form:

$$F = \frac{kT}{p} \frac{1}{4} \left(\frac{s}{L} \right)^2 + \frac{s}{L}, \quad (1.15)$$

where F is the force applied, L is the contour length, and s is the extension. As with the basic FJC model the WLC assumes inextensibility and relies on the persistence length as the sole measure of deformability. Since the WLC only considers the entropic contribution to the free energy of the chain, it will fail when used beyond the low-force regime. Up to this point, the contour length L has referred to the total end-to-end distance for a fully elongated chain assuming inextensibility. Since the internal bonds are extensible, it is possible to stretch molecules beyond their entropic contour length. The entropic contour length, L_0 , may therefore be considered to be an approximate boundary value separating the entropic and enthalpic regimes. Beyond the entropic regime, the contour length L becomes a function of the external tension. For DNA this transition occurs at forces above $10kT/nm = 41pN$, beyond which the extensibility of the chain must be considered [45]. A revised model was provided by Odijk in 1995 by considering extensible polymer chains under tension [46].

The Odijk model, in a manner similar to the extended FJC, is defined in terms of the extension and the chain elasticity:

$$s = L_0 \left[1 - \frac{1}{2} \frac{kT}{Fp} \left(\frac{F}{kT} \right)^2 + \frac{F}{K} \right], \quad (1.16)$$

where K is the elasticity of the chain. This model has been shown to correspond to the Kratky-Porod model in the entropic regime [47]. The different forms of the WLC and FJC models are summarized in table 1.1.

It is important to note that while both the freely jointed chain and the wormlike chain models may provide valuable descriptions of particular systems, they are none the less idealizations. As such, the FJC and WLC models ignore important contributions due to solvent effects and intramolecular interactions. Accurate mechanical descriptions of nonlinear and compound polymeric materials will require modification of these models or an altogether fresh approach.

Table 1.1. Summary of the freely jointed and wormlike chain models.

Model	Standard Formulation	Extended Formulation
Freely-Jointed Chain (FJC)	$s = L \left(\coth \left(\frac{FL}{kT} \right) - \left(\frac{kT}{FL} \right) \right)$	$s = \left(\coth \left(\frac{FL}{kT} \right) - \left(\frac{kT}{FL} \right) \right) \left(L + \frac{uF}{k_{\text{ext}}} \right)$
Wormlike Chain (WLC)	$F = \left(\frac{kT}{p} \right) \left(\frac{1}{4 \left(1 - \frac{s}{L} \right)^2} - \frac{1}{4} + \frac{s}{L} \right)$	$s = L_0 \left(1 - \frac{1}{2} \left(\frac{kT}{Fp} \right)^2 \right) + \frac{F}{K}$

1.4. Manipulations of Biological Molecules and Results

The investigation of the physical properties of polymers, both natural and synthetic, has commanded the attention of numerous researchers for many years. The advent of force spectroscopy has supplied a new perspective to the quest to define macroscopic properties based on intrinsic molecular interactions. In particular, the contribution to the understanding of physical properties of biological systems has been significant, and continues to impact most areas of biological research. Force spectroscopy investigations of polysaccharides, nucleic acids, and proteins have contributed to both our understanding of polymeric systems in general and our understanding of biological systems. Contributing to the immediate goal, reproduction of previous force spectroscopy investigations of biological macromolecules allows for the testing of our force device by assessing the accuracy of the data using the models presented in section 1.3.2.

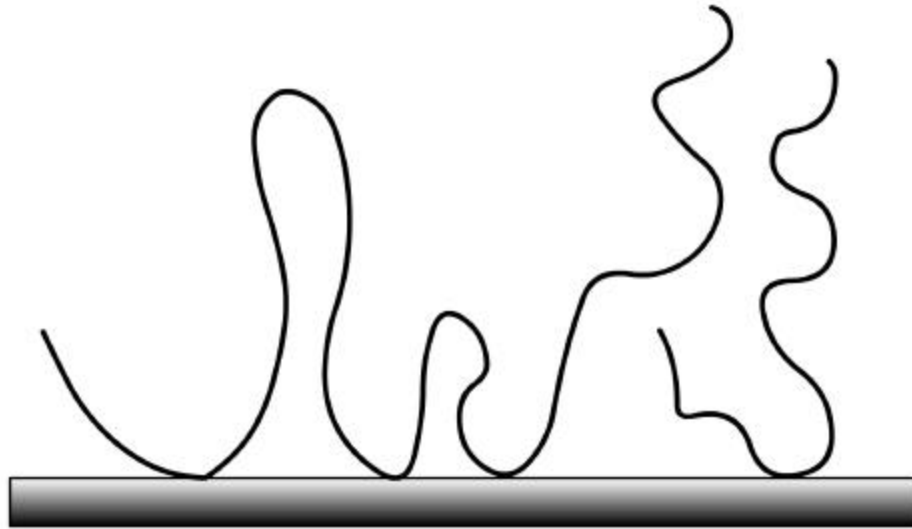


Figure 1.10. Schematic of a polymer brush structure formed by adsorption to a substrate.

1.4.1. Investigation of Polysaccharides with AFM

Polysaccharides are ubiquitous macromolecules many of which play natural mechanical roles. Since most polysaccharides adopt no regular secondary conformations in their natural environment, the investigation of their mechanical properties is out of reach of many techniques. When adsorbed to a substrate, polysaccharides will form a brush-like structure [48] (Figure 1.10) that facilitates their attachment to the AFM cantilever. The possibility of FS studies of polysaccharides was first demonstrated using dextran, an α 1,6-linked polysaccharide with a pronounced transition occurring at approximately 850pN [49, 50]. Importantly the forces measured in FS experiments are sensitive to the duration of the event, which is in turn dependent upon the force

constant of the cantilever and the rate at which the cantilever is moved [51]. Force-extension data for β -linked polysaccharides show only the entropic elasticity contribution, while α -linked polysaccharides such as carboxymethyl amylose exhibit a characteristic profile that has been shown to be due to the transition of the pyranose rings from the chair to the boat conformation [52-54] (Figure 1.11A). At first glance this seems counterintuitive, however it is not the pyranose ring conformation *per se* that accounts for the elongation, rather it is the separation between the glycosidic oxygen atoms. Experiments on pectin, an α 1,4-linked polysaccharide, have demonstrated that a two-step transition from the chair conformation to an inverted chair conformation can be obtained. The first transition occurs at approximately 300pN and the second at 800-900pN [55]. It has further been shown that the transition profiles are characteristic of the type of glycosidic linkage and that individual polysaccharides may be identified in a mixture [50]. The mechanical properties of

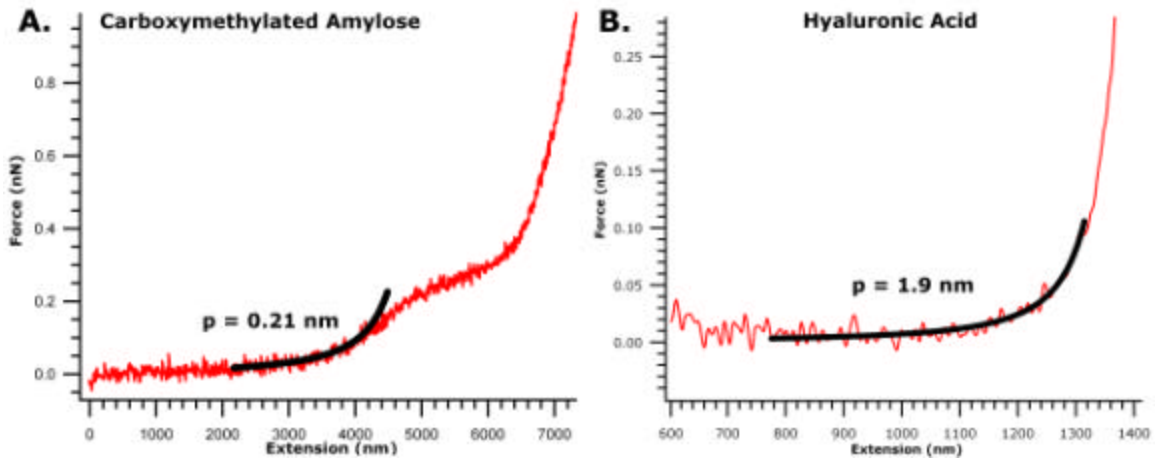


Figure 1.11. Representative force curves for A. carboxymethylated amylose and B. hyaluronic acid. Wormlike chain fits are included and the extracted persistence length is noted.

polysaccharides such as hyaluronan, the backbone molecule of the glycocalyx [56-58], have been analyzed using an optical trap [47] and are here measured using the AFM (Figure 1.11B). Hyaluronan interacts with the extracellular matrix and may be involved in the regulation of the motility of cells; in particular, cancer cells have been shown to exhibit altered mobility in the presence of excess hyaluronan [59-61]. Therefore, knowledge of the mechanical properties of natural polysaccharides will contribute to the understanding of dynamic mechanical processes involving intercellular interactions.

1.4.2. Investigation of Nucleic acids with AFM, Laser Tweezers & Magnetic Tweezers

The investigation of DNA and RNA mechanics represents the next structural level of polymer dynamics. Ribonucleic acid and single-stranded DNA consist of four nitrogenous bases attached to a phosphorylated sugar backbone. In itself, this represents a new level of mechanical behavior and, since RNA, and single-stranded DNA, will form hairpin loops as the bases associate with their complements, there is immediately an additional level of organization about which force spectroscopy studies have provided new insight. Adding to the structural roster is the fact that DNA naturally forms double stranded

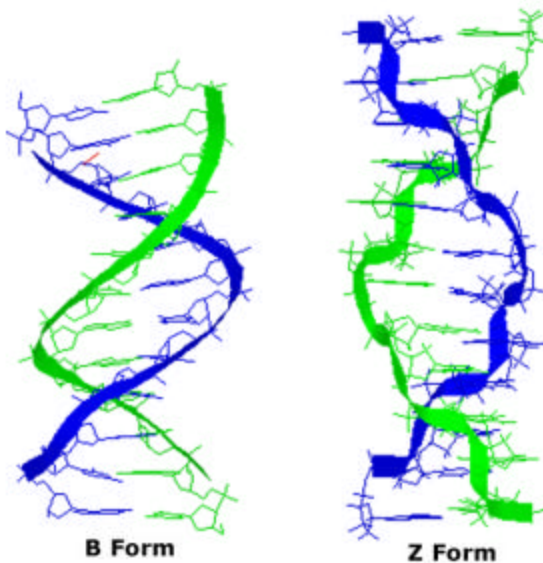


Figure 1.12. Illustration of two varieties of DNA double helices. Illustration from [62].

helical complexes of different pitch and orientation [62, 63] (Figure 1.12). It has been shown that the type of helix, A, B or Z, is detectable by FS techniques [64, 65]. The helical structures are further compacted by proteins called histones adding another level of organizational forces that can be measured by force spectroscopy. Not only does the investigation of double-stranded DNA provide important information regarding the dynamics of compound polymers it also presents an opportunity to investigate the forces at play in the most fundamental process of life.

The earliest FS investigations of DNA utilized magnetic tweezers [35]. Subsequent work using optical techniques measured the

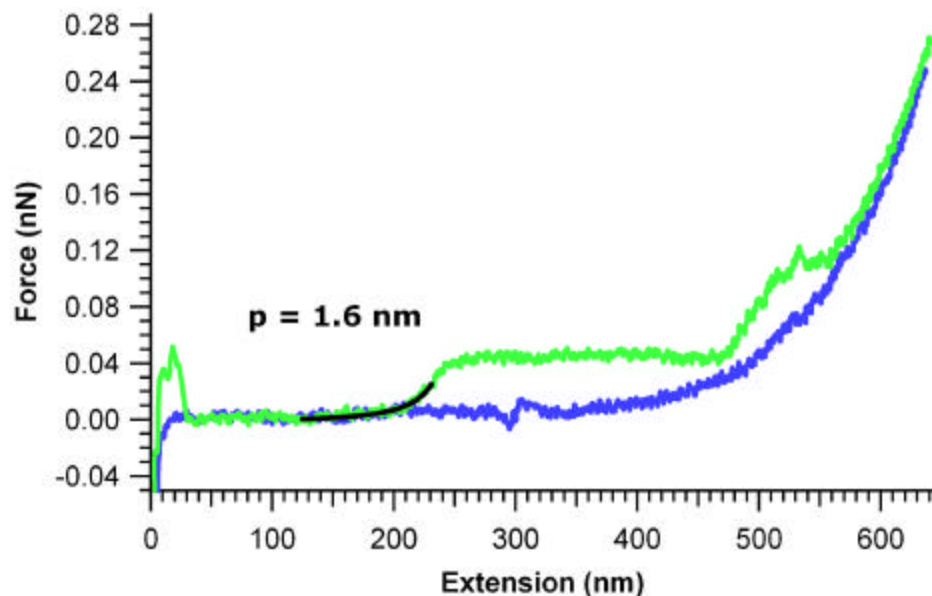


Figure 1.13. Representative force profile for dsDNA. Note the two transitions indicating unwinding of the helix and melting of the double strand respectively. A wormlike chain fit is included.

elasticity of both single- and double-stranded DNA (dsDNA) [36, 66]. These studies inspired the investigation of relaxation modes in extended DNA molecules resulting in a conceptual framework applying to any extended macromolecule [67]. The first investigation of DNA mechanics via AFM-based force spectroscopy showed a transition beyond that shown in previous work at a force of 150pN [68], which was subsequently demonstrated to be the melting of the double-strand [65]. A representative force curve for dsDNA, produced with our force device, is presented in figure 1.13. Additional work explored the base pair and velocity dependence of the force required to denature the double strand [69]. The mechanical properties of single-stranded DNA exposed in AFM experiments has inspired theoretical analysis of the denaturation of RNA [70] and FS studies of single RNA molecules[71]. Subsequent work explored the binding and condensation forces of DNA [72]. Investigations of the mechanical properties of single DNA molecules has led to a greater understanding of the forces and energies involved in cellular processes, particularly the modulation of protein-DNA interactions by mechanical forces [73-75] and the structural state of the DNA strand. It has also provided a knowledge base for studies of the creation of DNA-based nanotechnology [76, 77].

1.4.3. Investigation of Proteins with AFM & Laser Tweezers

While the interaction of nucleic acids with proteins is extremely important from a mechanical point of view, many proteins have intrinsic structural and mechanical properties that have crucial natural roles and lend themselves to investigation using AFM-based force spectroscopy. Proteins are long chains of amino acids that form secondary α -helical and various β -type structures which are connected via random loops [78, 79] (Figure 1.14). The secondary structures often organize into tertiary and quaternary assemblies. The unfolding of these structures will show a characteristic pattern when subject to longitudinal forces, as with the muscle proteins titin (Figure 1.15) and

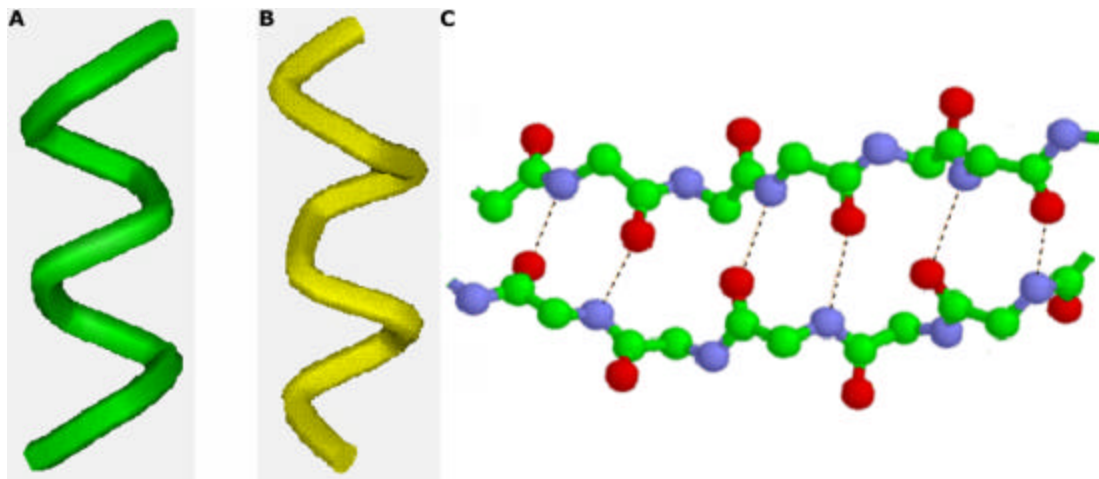


Figure 1.14. Illustration of an α -helical structure (left) and a β -sheet (right). Illustration from [78, 79].

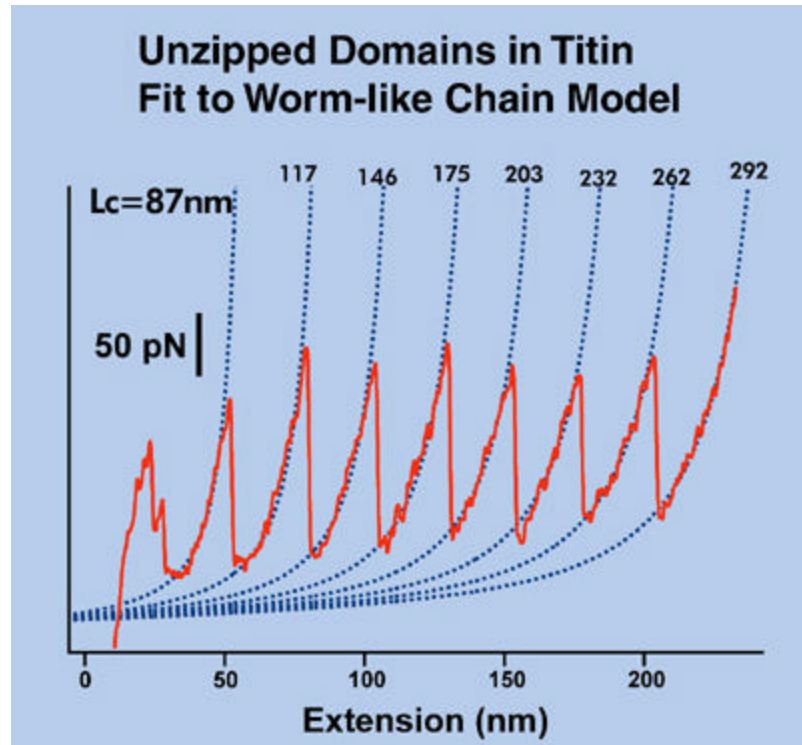


Figure 1.15. Force curve taken with the Asylum Research MFP-1D™ with a protein molecule composed of tandem repeats of a Titin module tethered to the cantilever. The solid curve shows the experimental data and the broken curves show the fits to the Worm-like chain model. The numbers next to the fits indicate the contour length obtained from the fit. *Data courtesy of Dr. J. Clarke, S. Fowler and A. Steward of Cambridge University, UK. Used with permission of Asylum Research.*

tenascin [80-82]. In the cases where the unfolding events are too close together to differentiate, recombinant techniques allow for insertion of extra amino acids to form longer random loop regions to separate the organized domains and allow for discrete measurements of unfolding events. Recombinant manipulations also allow for the investigation of specific protein domains [83, 84]. These mechanical and genetic manipulations are important constituents in the quest to identify the molecular mechanisms responsible for the resilience and compliance of biological systems.

Since many proteins play *in vivo* mechanical roles, investigation of their intrinsic mechanical properties has major implications for understanding the interactions of microscopic and submicroscopic cellular and extracellular components [85-89]. Of particular interest is one subject of the present work, the mechanical properties of the fibrous extracellular matrix protein type I collagen.

1.4.4. Introduction to Force Spectroscopy Studies of Collagen

Comprising 25% of the protein mass of mammals, collagen is a ubiquitous connective tissue component that is responsible for regulation of motion and structural integrity [90]. Many studies have been performed on collagenous tissues providing a strong understanding of the macroscopic mechanical properties [91-94]. In order to understand the origin of the macroscopic properties, investigations must proceed to the microscopic and submicroscopic domains. Collagenous tissues are formed from collagen fibers assembled from a basic collagen monomer [95]. The collagen monomer is a tertiary protein structure that has yet to be examined by single molecule force spectroscopy. Bridging the gap between the biochemical studies of monomeric collagen and macroscopic

mechanical studies requires the investigation of the fibrillar structural level, a level on which very few investigations have so far focused. The force regime available to AFM-based force spectroscopy is on the scale necessary to probe collagen fibril mechanics.

CHAPTER 2:

Review of Collagen Biochemistry and in vivo Mechanics

2.1 Role of Collagen in Bone, Connective Tissues and Diseases

The role of type I collagen in the extracellular matrix is primarily the regulation of structure. The flexibility of skin and tissues in the cardiopulmonary system is provided by the protein elastin. The fibers formed from elastin have a very large extensibility that is limited by the stiffer collagen fibrils [96]. This elastic limitation helps preserve

the shapes of organs so that they may properly perform their functions without serious damage. In a complementary role, collagen in bone provides a rigid framework for the attachment of independent tissues. Connections between bones are formed by collagen-containing ligaments that help stabilize the joints and tissues are attached to bones by collagenous tendons. In order for tissues to provide a useful function, the force produced by their flexure must be transmitted to a rigid structure; the tendons perform this function. Through these varied but related roles, collagen is responsible for the dynamic nature and the long-term structural integrity of many organisms. Because of the extensive physiological role played by collagen, diseases in which it is affected are often serious, and understanding the specific molecular contributions to the mechanical properties of collagenous tissues will enhance our understanding of the pathologies of such diseases.

Many diseases of genetic origin affect connective tissues. Of particular interest are those that have an effect on the cross-linking properties of the compromised tissue such as osteogenesis imperfecta (OI) [97]. Indications of OI include brittle bones as well as weakened arterial walls, which will promote the development of aneurisms. Altered cross-linking is detectable early in the progression of OI suggesting that there is ample time for tissue failure as well as

therapeutic treatment. Many investigations have focused on the mechanical properties of tissues and macroscopic collagen fibers. Few investigations, apart from ensemble measurements via x-ray diffraction [93], have been performed on the microscopic or molecular levels of collagen organization. To investigate the lower organizational levels, collagen must be dissolved and reconstituted in vitro to produce the particular level of interest, herein the fibrillar levels.

Force spectroscopy investigations of reconstituted collagen fibrils will be presented in chapter 3. Since the mechanical properties of fibrils are directly affected by their molecular organization, it is crucial that current knowledge of collagen assembly be understood in order to interpret the force spectroscopy data. The following section provides a detailed overview of collagen assembly beginning with collagen polypeptides and ending with macroscopic fibers. Much discussion is focused on the microscopic and submicroscopic levels of organization, the levels of interest in the subsequent force spectroscopy investigations.

2.2 Collagen Structure (including cross-linking)*

2.2.1 Overview of Structure

The most abundant collagen in mammalian connective tissues and bones is type I, with various other types playing regulatory roles. The most abundant amino acid in the type I collagen polypeptide is glycine, which occurs in every third position. In the sequence gly-X-Y, alanine, proline and hydroxyproline are most often found in the X and Y positions. Other amino acids are also found in these positions, such as lysine, which plays an important role in fibril growth, stabilization and mechanics.

There are two types of polypeptide chains in type I collagen, the $\alpha 1(I)$ and $\alpha 2(I)$ chains (Figure 2.1a). The $\alpha 2(I)$ chain is approximately 90 residues shorter than the $\alpha 1(I)$ chain. Both chain types form left-handed helical secondary structures that wind together in a right-handed fashion forming a tertiary triple-helical structure composed of two $\alpha 1(I)$ chains and one $\alpha 2(I)$ chain (Figure 2.1b).

* The information for this section is primarily from references [98, 99] Exceptions are noted.

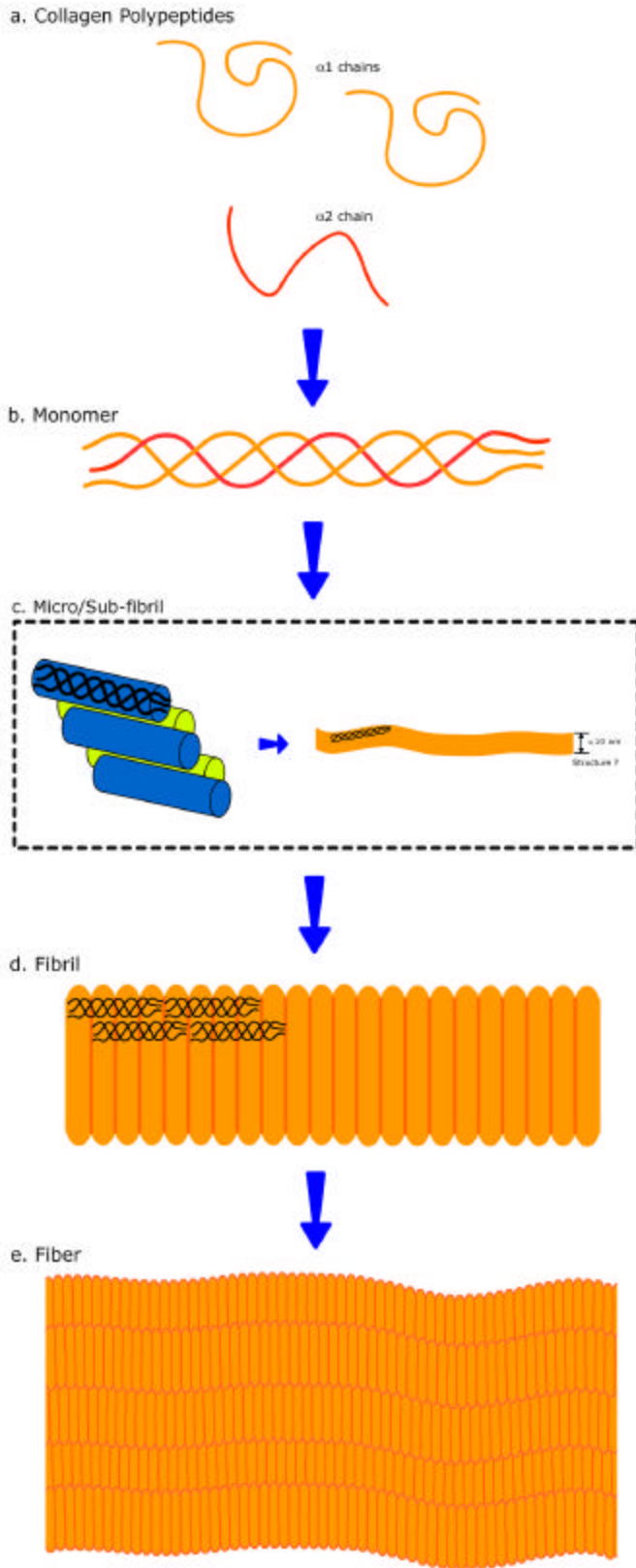


Figure 2.1. Schematic of the hierarchical assembly of collagenous tissues. Collagen polypeptides (a) intertwine to form the collagen monomer (b). Monomers arrange into microfibrils then subfibrils (c). Subfibrils arrange to form fibrils (d) that continue assembly to form fibers (e) and eventually tissues.

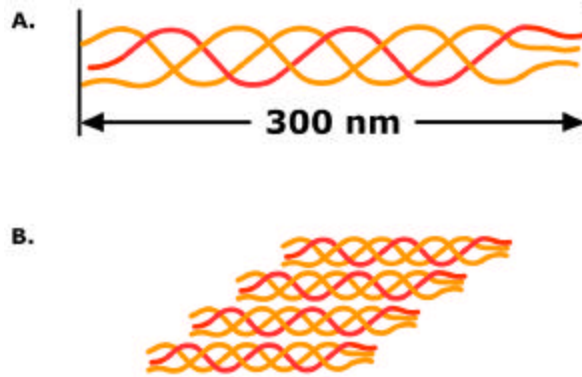


Figure 2.2. **A.** Schematic of collagen monomer. **B.** 2-D schematic of *D*-staggered “microfibril” arrangement illustrating the degree of monomer overlap.

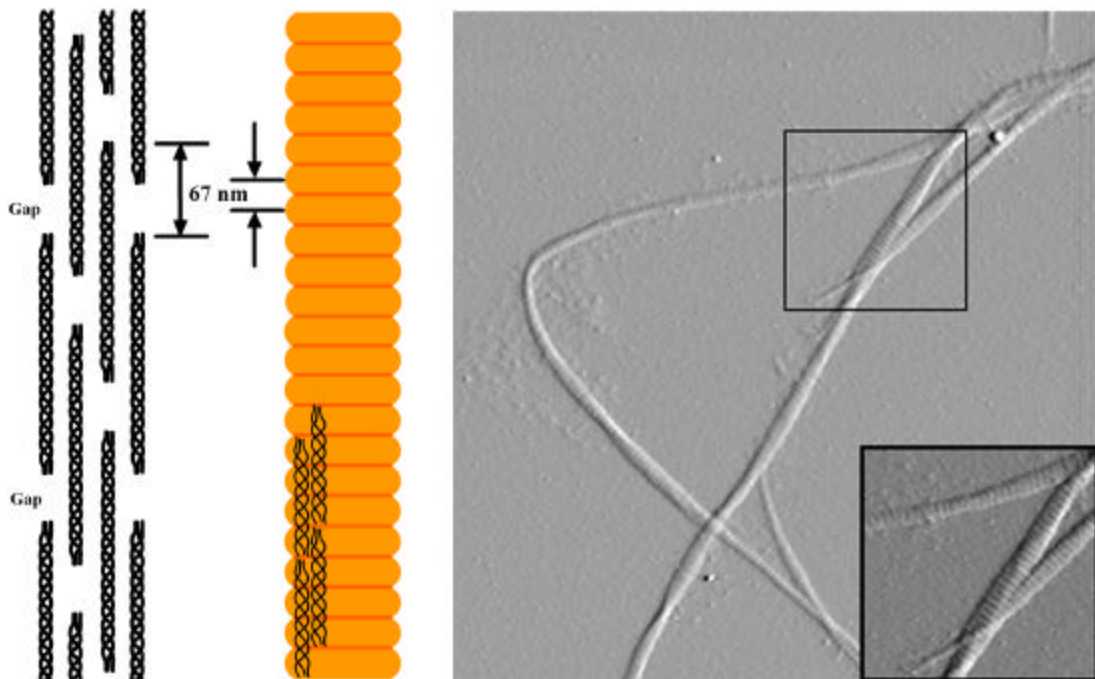


Figure 2.3. Schematic longitudinal cross-section of a collagen fibril illustrating the 67nm banding region and an AFM topograph of reconstituted type I collagen fibrils adsorbed to mica with the banding pattern visible. The AFM scan was acquired under ambient conditions using a Nanoscope III from Digital Instruments.

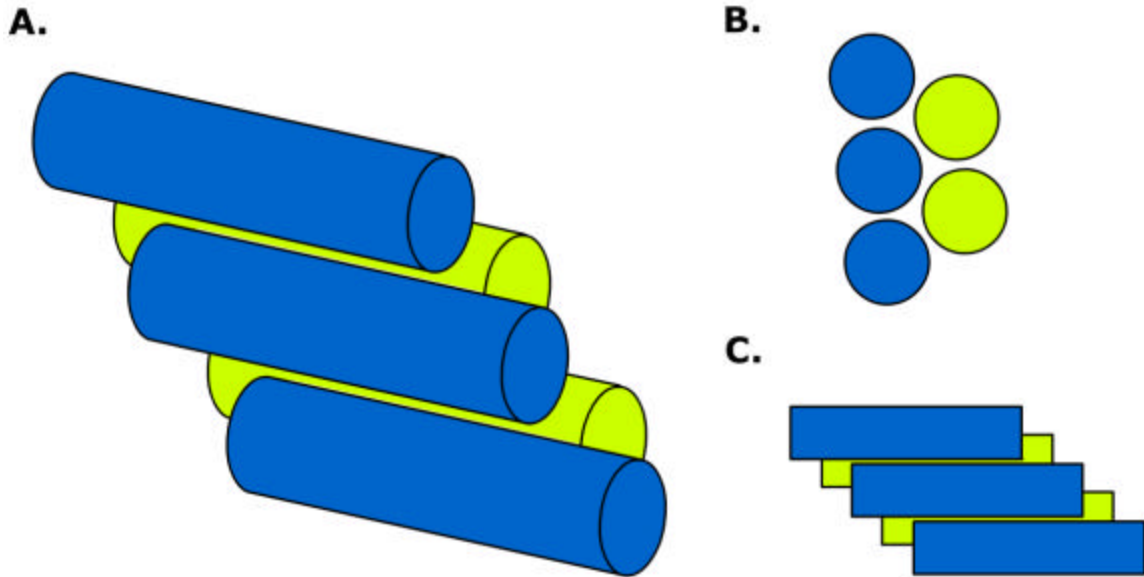


Figure 2.4. Schematics of monomer packing in a “microfibril”. **A.** Perspective view of a microfibrillar bundle. **B.&C.** End and side views respectively.

The triple-helical monomers arrange in a staggered fashion forming microfibrils 5nm in cross-sectional diameter and 450nm long which proceed to form sub-fibrils of approximately 10nm cross-sectional diameter and 1 μ m in length (Figure 2.1c) [100]. Sub-fibrils assemble laterally and longitudinally into fibrils of 20nm to 200nm in cross-sectional diameter (Figure 2.1d). The structure of the sub-fibrils is still unresolved, but evidence suggests that they are stable structures having 10nm cross-sections [101, 102]. Sub-fibrils and fibrils are stabilized by interstitially-bound phosphate and sulfate ions, as well as covalent cross-links catalyzed by the enzyme lysyl oxidase [103-105]. Macroscopic fibers are formed via lateral assembly of many fibrils and are the fundamental units of tissues (Figure 2.1e).

2.2.2 From Monomers to Sub-Fibrils

The fibril-forming triple-helical monomers are 300nm long and 1.5nm in diameter [106]. Under physiological conditions, type I collagen monomers are capable of entropically driven assembly into fibrils [104, 107]. The monomers first assemble into a quarter-staggered conformation as indicated in figure 2.2. This so-called *D*-staggering is widely believed to be responsible for the observed 67nm banding pattern of native type I collagen fibrils. This banding pattern is present in reconstituted collagen fibrils as shown in figure 2.3. Under physiological conditions, spontaneous formation of these *D*-staggered assemblies, called microfibrils, is driven by hydrophilic interactions that may be largely due to charged regions in the nonhelical telopeptide regions of the monomers [100, 108]. Evidence suggests that these microfibrils are composed of five monomers arranged into a bundle as illustrated in figure 2.4 [109, 110]. Aggregation continues laterally and longitudinally until a fibril is formed. The precise manner in which this aggregation occurs is still unknown. What is clear is that growth occurs through some combination of lateral and longitudinal aggregation. While surface charges are sufficient to promote aggregation of microfibrils into larger constructs, they are not

sufficient to promote fibril growth. Longitudinal growth is likely promoted by the formation of covalent cross-links [100, 111] that also provide structural stability in tissues in conjunction with interstitially bound phosphates and sulfates [105].

2.2.3 Cross-Linking

Several types of cross-links are found in collagen fibrils. Included are intra-monomeric disulfide bridges, glycosydic cross-links formed via nonenzymatic glycation during aging [112, 113] and as a result of diabetes [113, 114], and interstitial phosphate and sulfate cross-links [105]. Perhaps the most important cross-links are the covalent linkages promoted by the activity of the enzyme lysyl oxidase. Lysyl oxidase catalyzes the deamination of the ϵ -amino group from lysine and hydroxylysine residues, forming reactive aldehydes [103].

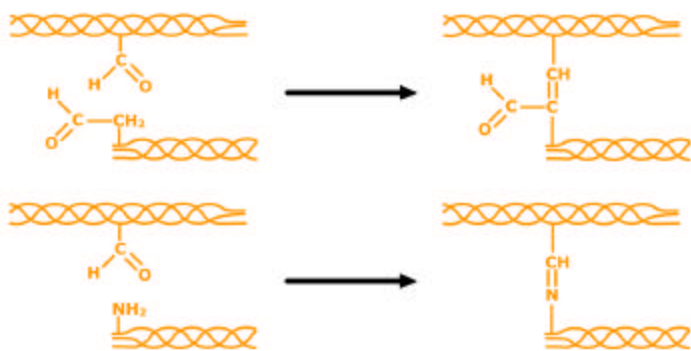


Figure 2.5. Schematics of covalent cross-links found in collagen. TOP: Aldol linkage. BOTTOM: Schiff base linkage.

These enzymatically-produced aldehydes, in conjunction with free amino groups along the length of the monomer, provide the opportunity for two types of covalent cross-links to form. Condensation between two aldehydes produces an aldol cross-link and condensation involving an aldehyde and a free amino group will produce a Schiff base cross-link [115], as illustrated in figure 2.5. These enzymatically promoted cross-links may be responsible for the differing mechanical properties of wildtype (wt) collagen and collagen produced in diseases such as osteogenesis imperfecta (OI).

Charges on collagen monomers are important for promoting aggregation, but they also serve to facilitate important noncovalent cross-links. Phosphate and sulfate ions will assume interstitial positions within a fibril in regions having a net charge [105]. Figure 2.6 is a schematic based on figure 8 in reference [105] illustrating the

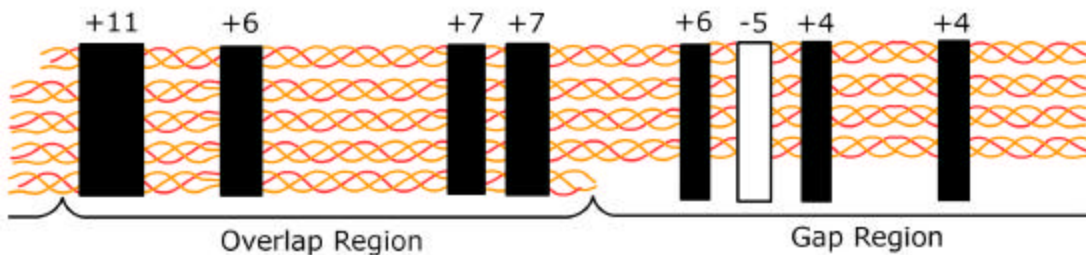


Figure 2.6. Schematic illustrating axial charge distributions in wildtype collagen fibrils. Eight charged regions provide potential binding locations for multivalent ions such as phosphate and sulfate ions.

distribution of axial charge density in collagen fibrils. There are eight charged regions where multivalent ions may bind. Such ionic cross-links will add stability to fibrils, in addition to providing restrictions on longitudinal deformations.

It is important to realize that much of the information presented above is the result of work that is quite old. Within the limitations of available measurement techniques, the results are sound. Recent work has suggested that important modifications to the models of assembly and cross-linking are needed. The observed banding pattern for instance may arise from contributions other than the geometric arrangement of collagen monomers. New evidence suggests that α_1 -acid glycoprotein may contribute to the structural integrity of collagen fibers and, in fulfilling this role, may have an effect on the observed banding pattern [116]. Better knowledge of collagen structure is also needed to fully understand the process of acid reduction and reconstitution and the role played by cross-links.

2.2.4 In Vitro Production of Collagen Fibrils

Cross-links stabilizing the fibrils are of reducible and irreducible forms, so it is likely that the process of reconstitution is not the reassembly of monomers alone, but the assembly of monomers and

larger sub-fibrillar aggregates that were maintained by irreducible bonds. The aggregates may act as nucleation sites for fibril production, as is believed to be necessary [100]. Recent evidence shows that, in low pH/low salt collagen solutions, monomers are in equilibrium with larger aggregates, an observation supporting the conclusion that irreducible bonds restrict the ability to obtain a solution of monomers from mature tendon [100, 117]. After dissolving collagen in acetic acid, AFM scans were performed that confirm the presence of intact fibrils, (Figure 2.7) and force spectroscopy data of acid solutions of

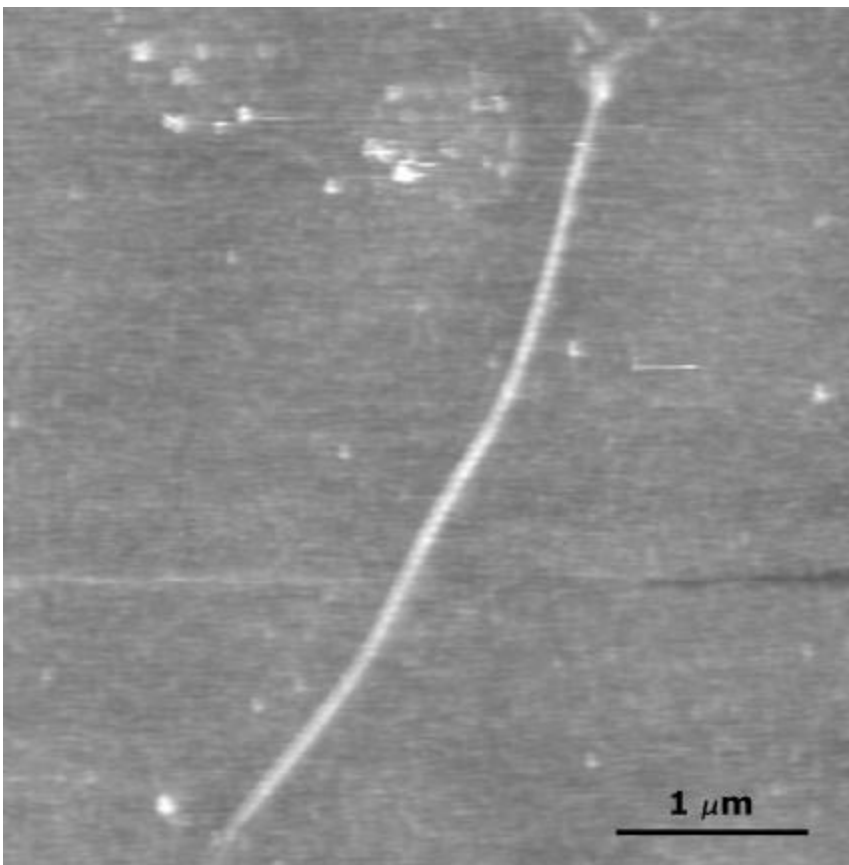


Figure 2.7. AFM scan of acid-solubilized collagen made under ambient conditions showing that a large fibril remains. Solution was deposited onto mica and allowed to dry, then rinsed with DI water. Solvent was 0.005mM acetic acid. Scan was acquired under ambient conditions using a Nanoscope III from Digital Instruments.

collagen repeatedly exhibit force profiles of species $>1\mu\text{m}$ in length. *In vitro* production of collagen fibrils is more reliable, but still does not result in a homogeneous solution.

Two *in vitro* production techniques were employed to generate the collagen fibrils used for the investigations that will be discussed in chapter 3: assembly from collagen produced by cultured human fibroblasts and reconstitution of acid-solubilized collagen extracted from mouse or rat tails. It is important to distinguish between the two production techniques in order to properly interpret the subsequent force spectroscopy data. The assembly of collagen from cell culture produces somewhat artificial fibrils that appear morphologically identical to naturally produced collagen fibrils. Although the model fibrils resemble natural fibrils in appearance, their mechanical properties may differ. Reconstituted fibrils are produced by taking naturally produced collagenous tissues from an animal, dissolving them in acetic acid, and reassembling the fibrils in a physiological buffer. Details of these assembly processes are provided below in section 2.2.5.

Although production of collagen fibrils is reliable in the sense that there will nearly always be properly assembled fibrils in the final solution, the solutions will be an equilibrium mixture of fibrils and

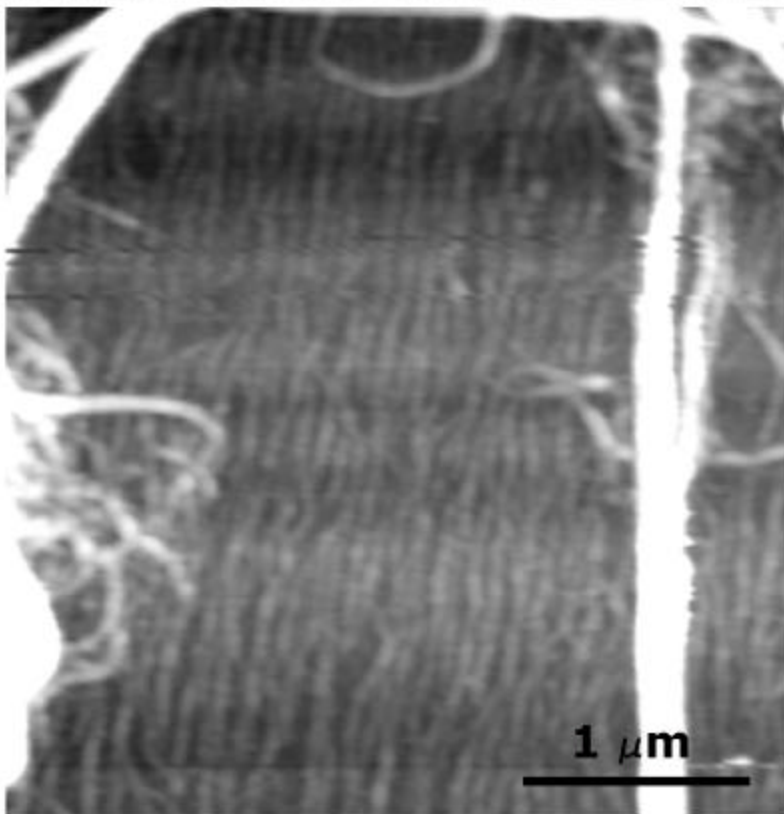
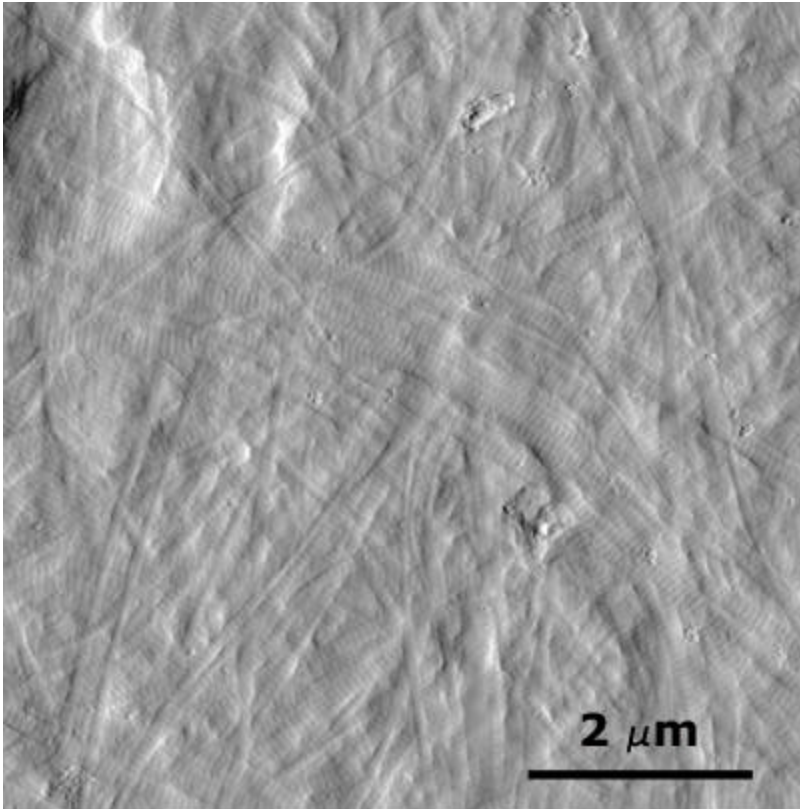


Figure 2.8. AFM scans of reconstituted collagen performed under ambient conditions. Top scan of sample taken from pellet shows an abundance of large fibrils. Note the visible banding pattern. Bottom scan shows large fibrils about the edges (bright regions) with fibrils of about 60nm diameter present in the same solution.

subfibrils. This equilibrium solution of different levels of collagen structure poses a challenge for force spectroscopy studies, in that there will typically be at least two species, possibly with differing mechanical properties, in the sample under investigation. Centrifugation attempts failed to produce homogeneous solutions, but it was realized that, after allowing the solution to stand at 4°C for approximately a week, the larger fibrils precipitated. AFM scans of the resulting pellet revealed a dense network of fibrils resembling a poorly assembled collagenous tissue (Figure 2.8A). Complementary scans of the supernatant solution revealed a mixture consisting primarily of subfibrils, with a few larger fibrils still present (Figure 2.8B). These conditions provide a rudimentary means of selecting subfibrils; by working only with the supernatant solution. Selection of *fibrils* is accomplished by simply vortexing the solution, resuspending any fibrils that have precipitated.

2.2.5 Materials and Methods

Human Collagen Fibril Production

(Fibrils were prepared by the lab of Dr. Charlotte Phillips in the Department of Biochemistry.) Collagen was purified from human dermal fibroblast culture by ethanol precipitation and dissolved in 0.5N acetic acid. Dissolved collagen was treated with pepsin at 4°C overnight to remove nonhelical telopeptide regions, in order to prevent spontaneous cross-linking in these terminal regions. Samples were lyophilized and resuspended in 5mM acetic acid to a concentration of 2mg/mL. In-vitro assembly was performed as a 1:1 mixture of collagen and 30mM NaP_i/100mM NaCl at 30°C, pH 7.0, for 6h and monitored by spectrophotometry at 313nm.

Mouse-Tail Collagen Fibril Production

(Fibrils were prepared by the lab of Dr. Charlotte Phillips in the Department of Biochemistry.) Fibrils were prepared from wt and OIM (osteogenesis imperfecta murine) mouse-tail tendons by grinding the tissue in 0.1M phosphate buffer, 20% EDTA solution. The mash was diluted 1.5X and centrifuged. The pellet was resuspended in 0.5N acetic acid for two nights at 4°C. The extract was centrifuged, and the

supernatant was subjected to a salt extraction (30% NaCl in 0.5N acetic acid) at 4°C overnight. A third centrifugation was performed, and the pellet was resuspended in 0.5N acetic acid. Assembly was performed by diluting solution with phosphate buffer to final concentrations between 250µg/mL and 2mg/mL.

Rat-Tail Collagen Fibril Production

Type I collagen from rat tail was purchased from Sigma-Aldrich (St. Louis, MO). The samples were dissolved in either 2mM or 5mM acetic acid at a concentration of 1mg/mL with gentle agitation at 4°C overnight. Reconstitution was performed at 26°C for 12h or overnight, typically at a concentration of 500µg/mL.

Force Spectroscopy of Collagen Fibrils

Samples were deposited on clean glass microscopy slides in aliquots of 10-20µL and allowed to adsorb for approximately 20min, but were not allowed to dry. Prior to beginning data acquisition, the samples were rinsed extensively with 18MΩ-cm water. Data was acquired in 1X PBS at pH 7.4. Cantilevers were used without modification.

CHAPTER 3:

Mechanical Properties of Collagen Fibrils

3.1 Force Spectroscopy Studies of Collagen Fibrils

3.1.1 Background

A large variety of vertebrate tissues have, within their structure, complex networks of collagen and elastin fibers [118] that govern their mechanical properties. Collagen must withstand elastic extension in the vasculature, skin, and lungs, as well as compression in articular cartilage. Interplay between cells and the extracellular matrix (ECM) is critical in both physiological and pathological processes such as tissue

morphogenesis [119-123], wound healing [124, 125] and tumor invasion [126]. Additionally, the pathologies of certain connective tissue disorders including osteogenesis imperfecta (OI), Ehlers-Danlos syndrome and fibrocontractive diseases [127] are believed to be directly related to defects in collagen monomer structure, which have major impacts on the biomechanical properties of cells, tissues and the organism. During their directed displacement, migrating cells exert forces against their substrates [128, 129]. On the molecular level, collagen fibrils are submitted to mechanical stresses by fibroblasts through specific cell surface integrins. Recent results obtained using a variety of force-monitoring devices indicate that individual cells can generate traction forces larger than the force required to stretch individual proteins or fibrillar assemblies [106, 107, 130]. These studies have also demonstrated that the rate of displacement of fibroblasts greatly depends on the stiffness of the matrix in which they move. For these reasons, understanding the mechanical properties of collagen at the fibrillar level is critical to understanding its role as a force-bearing structural element in the ECM.

Two primary approaches have been used to investigate the structure and role of collagen fibrils in a variety of tissues. One is a biochemical approach, which involves isolating and purifying all the

different components (type I, III and V collagens, proteoglycans, etc) of collagen fibers and fibrillar tissues, determining their structures and investigating their interactions and roles *in vitro*. The other approach is the macroscopic biomechanical engineering approach, which involves measuring the bulk mechanical properties of tissues such as tendons, skin patches, or vesicular sections [93, 97, 131]. For example, typical load-extension curves for macroscopic wildtype (wt) mouse-tail tendons (Figure 3.1) show biphasic elastic behavior characterized by a compliant region (up to 5% elongation) followed by the extension of a very stiff structure with a tensile strength as high as 100MPa at a

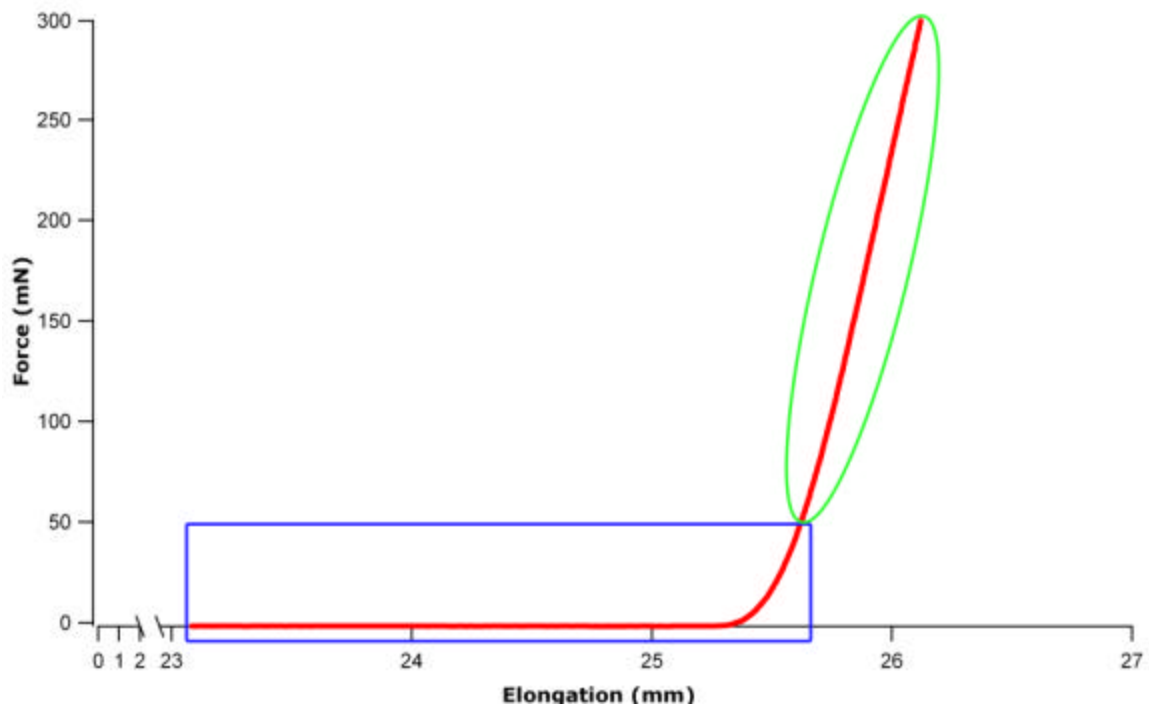


Figure 3.1. A load-extension curve for a wt mouse-tail collagen tendon. The lower boxed region corresponds to the compliant regime and the region in the oval to the regime of molecular contributions to the elasticity. *Data courtesy of Yannick Miron.*

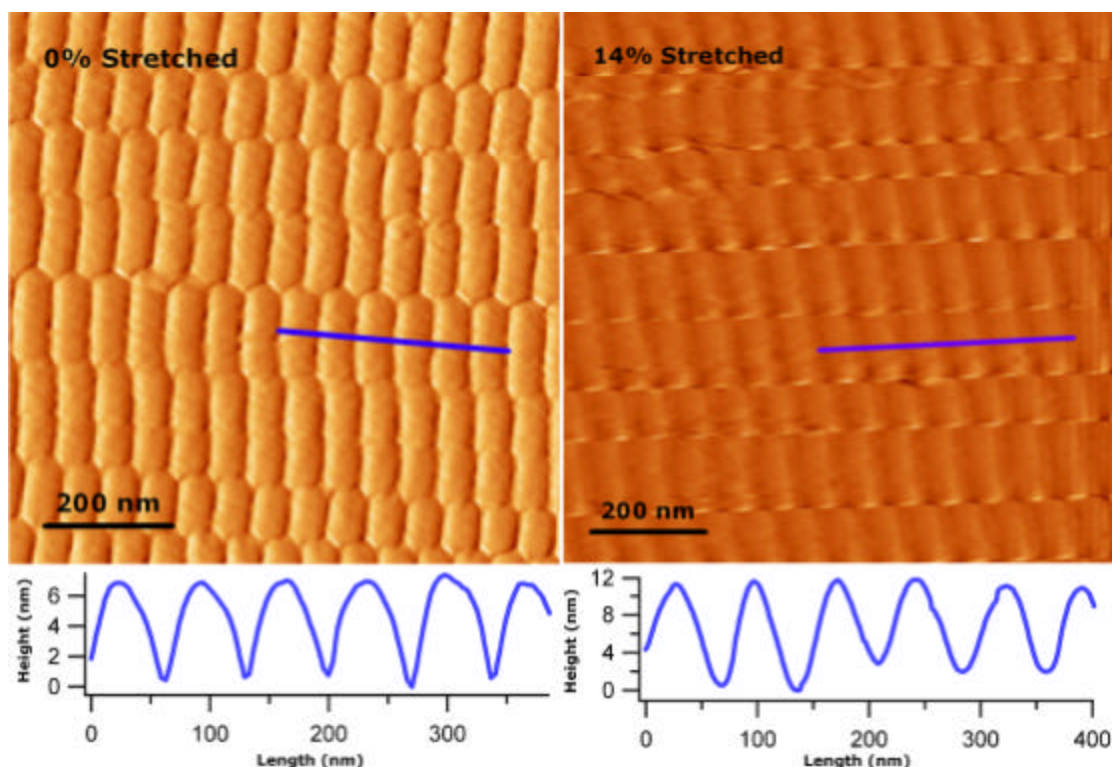


Figure 3.2. AFM scans of wt mouse-tail fibers showing 0% and 14% elongations. The 14% scan clearly shows an increase in the length of the gap region. The cross-sections below the scans indicate a length increase of 7 nm per gap. *Scans courtesy of Wonchul Shin.*

maximum elongation of 15% [132]. These ensemble measurements do not allow access to the molecular origin of the biomechanical properties, and it is very difficult to determine to what extent each molecular component and structural level (i.e. polypeptide backbone, collagen monomer and fibrils) contributes to the overall biomechanical properties of the system. AFM scans comparing 0% and 14% stretched collagen fibers are presented in figure 3.2. It is clear from the scans that the gap region exhibits a greater increase in length relative to the overlap region. The cross-sections below the scans help to quantify the

degree of stretching and indicate that, at 14% elongation, the gap region increases in length by 7nm. These scans provide significant insight into the molecular changes occurring upon stretching of collagenous tissues. In particular, it is clear that the molecular structure in the gap regions is more elastic than the structure in the overlap regions. Determination of the specific contributions of the molecular structures of the gap and overlap regions to the changes observed upon stretching, requires investigation of the individual structural elements of the fiber. AFM-based single molecule force spectroscopy provides a method to directly probe the molecular contributions of the fibrillar and monomeric levels of organization.

3.1.2 Force Spectroscopy of Model Human Type I Collagen Subfibrils

Type I collagen monomers isolated from a cultured human dermal fibroblast cell line were assembled *in vitro* into type I collagen fibrils [133]. Recall from section 2.1.4 that these solutions are heterogeneous, consisting of multiple levels of assembly, notably subfibrils and fibrils. The diameters of fibrils observed in the AFM scan of figures 2.3 and 2.8 are consistent with previous measurements performed by electron microscopy [104], AFM [134, 135] and X-ray

analysis [102]. In addition, the assembled fibrils exhibit the 67nm axial periodicity characteristic of type I collagen fibrils, indicating the assembly process generated biologically relevant fibrils.

Collagen fibril solutions in concentrations of 250 to 500 μ g/mL were allowed to adsorb onto mica or glass surfaces without drying. AFM cantilevers were used without the special preparation often required for protein or polysaccharide experiments. The elongation profiles (Figure 3.3, gray traces) exhibit a jagged pattern in the 2 - 4nN force range. This jagged pattern suggests that major reorganization of the fibril is taking place once a certain force threshold is attained. Similar features, but in a more defined manner, are often observed during the stretching of ECM proteins such as titin, tenascin and fibronectin [81, 82, 136]. In all of these single molecule experiments, the regular discontinuities in the force-elongation profile were attributed to unfolding of specific protein domains. Also notable in the collagen extension profiles, is that rather high forces up to several nano-Newtons are reached at maximum extension. In contrast, the relaxation profiles (Figure 3.3 black traces and bottom panel) exhibit a very smooth behavior over the full range of relaxation, with a characteristic plateau at approximately 300pN. The plateaus in

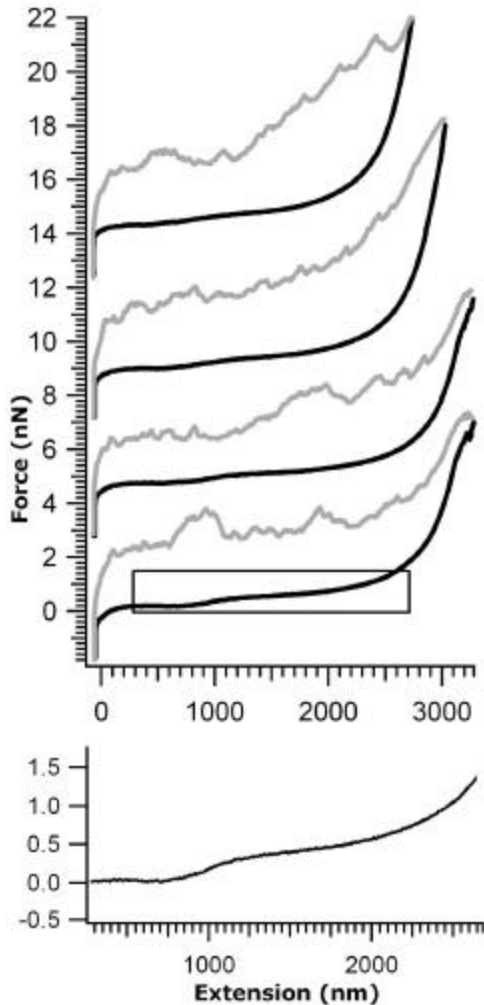


Figure 3.3. AFM force spectroscopy scans of human type I collagen subfibrils. Gray traces are the extension curves and black traces the relaxation curves. Note the jagged rupture pattern between 2nN and 4nN during stretching, and the smooth plateau at 300pN ending at approximately 1 μ m during relaxation. Bottom panel is an enlargement of the boxed region in the top panel, providing a clear view of the plateau.

the force profiles begin at approximately 1 μ m, a value consistent between experiments, indicating that the assembly being stretched has a contour length of approximately 1 μ m (see section 1.3.2 for a definition of contour length). This length scale suggests that subfibrils, known to be present in the solution (see [100, 117] and figure 2.8), are being stretched in these experiments. The length of the plateau, more than 100% of the contour length, indicates that major structural changes occur in the subfibril that are dependent upon the elongation

state. As documented for other systems [84], stretching of more than one molecule leads to ill-defined and irreproducible features in force profiles. For example, attachment of more than one molecule to the cantilever is unlikely to assume the same geometry in different experiments. Variation in the attachment geometry will produce inconsistent and irreproducible features in the force profile. Well-defined, reproducible features such as the observed plateau, result from the response of the system to an applied force and represent the mechanical fingerprint of the subfibrils.

The jagged pattern that is present over a large elongation range could potentially have more than one origin. One possible source, outside of structural changes in the subfibril, is peeling from the substrate. Such an event can be ruled out because macromolecular peeling events are characterized by a constant-force plateau and steps to lower forces as adsorbed segments of the macromolecule detach from the surface (Figure 3.4) [137-139]. Although there may be peeling within the data of figure 3.3, it does not contribute significantly to the observed profiles. It is therefore likely that substantial rearrangement of the structure is being observed as the 2nN force threshold is reached. These *in vitro* assembled collagen subfibrils are

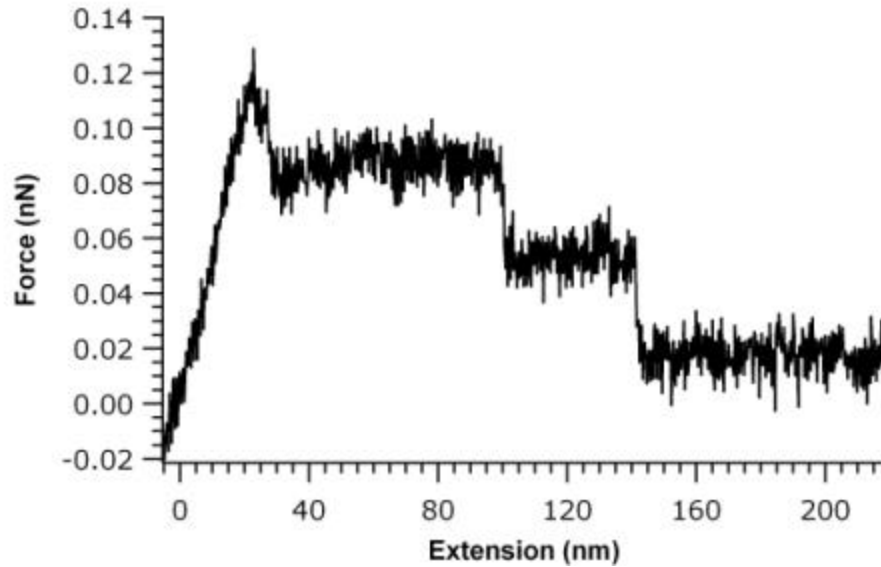


Figure 3.4. AFM force spectroscopy scan of a wt mouse-tail collagen fibril. The two plateaus with abrupt force steps at 100nm and 140nm are typical signatures of peeling a macromolecular structure from a substrate. Note that the steps are about 30pN in height, much lower than the rupture forces observed in the profiles of figure 3.3.

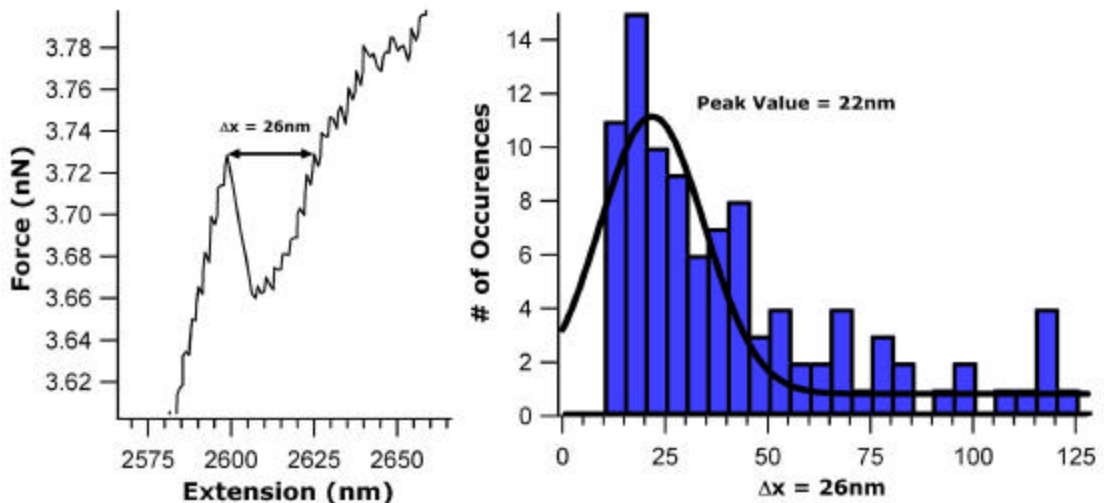


Figure 3.5. An example of the extension measurement technique showing a value of 26nm (left) and a histogram showing a peak elongation of 22nm (right).

composed of a large number of collagen monomers held together primarily via non-covalent, charge-based interactions [100, 105]. Treatment with pepsin prior to assembly served to remove the telopeptides at the ends of the monomers, as well as any lysyl oxidase present. Removal of lysyl oxidase reduces the number of covalent cross-links that may be formed. Consequently, these results strongly suggest that a large number of intra- and inter-monomer interactions are being disrupted upon the controlled elongation of the fibrils. Analysis of the extension profiles provides evidence of the origin of the ruptures. Measurement of 99 discontinuities in the elongation profiles (Figure 3.5) resulted in a histogram with Δx values ranging from 10 to 125nm and a peak value of 22nm. It is likely that these discrete elongations have their origin in a well-defined reorganization of the internal structure of the subfibril as tension is applied.

The organization of the monomers into a *D*-staggered configuration with a 67nm axial periodicity presents regions of monomer-monomer overlap with adjacent gap regions having reduced monomer packing density. Considering the observed 7nm increase in the size of the gap regions in stretched fibers (Figure 3.2), it is possible that the sequential stretching, and perhaps unfolding, of the

triple-helical polypeptides in the gap region of the fibrils is responsible for the discrete discontinuities observed in the elongation profile.

Since discontinuities are observed in the 2 to 4nN range in fibrils with cross-sectional diameters between 10 to 30nm, we can easily calculate the range of unfolding forces for individual collagen monomers (1.5nm cross-section) in fibrils to be between 4 and 90pN/monomer. Interestingly, this range of forces is similar to the force ranges measured for other single biological macromolecules. Unfolding of domains in titin and tenascin occurs between 150 and 300pN [81, 82], an alpha-helical domain in spectrin at 25pN [84], a transition in double stranded DNA occurs at forces between 50 and 200pN [36, 65], and 100 to 400pN for unfolding of an engineered calmodulin α -helical dimer [140].

In the case of simple multi-domain proteins like titin and tenascin, the increases in length exhibit a narrow distribution corresponding to the discrete unfolding of protein domains. The distribution in the case of collagen subfibrils indicates an unfolding process that may simultaneously involve disruption of helices and sliding between microfibrils. Collagen fibrils vary in cross-sectional diameter between the gap and overlap regions with the gap regions having the smallest cross-section and therefore a higher likelihood of

unfolding at a lower force than the overlap regions. In addition, there is evidence of a thermally labile domain of 66 amino acids in the gap region that would likely contribute to a sequential unfolding process [141]. However, if the gap and overlap regions unfolded sequentially, it might be expected, for example, that a series of discrete ruptures at some force F would be immediately followed by a series of discrete ruptures at a higher force $F + \mathbf{DF}$, much as the different structural changes in β -DNA occur sequentially in the force profile (see figure 1.13). However, no such pattern is evident in the collagen extension profiles. With the data currently available, it must be concluded that structural changes at the subfibrillar level do not occur in a discretely sequential manner, but may result from a cooperative unfolding process. Indeed, it was shown that, once the thermally labile domain unfolds, the entire structure will unfold [141].

An interesting parallel can be drawn between the jagged rupture pattern seen here for stretching of collagen fibrils and the rupture pattern seen for α -helices and the engineered calmodulin dimer mentioned above [140, 142]. The collagen polypeptide (hereafter α -chain) forms a left-handed helix, in contrast to the right-handed calmodulin α -helix, and cannot form *intramolecular* hydrogen bonds, but there are two *intemolecular* hydrogen bonds per 8.7Å pitch. It is

therefore likely that the disruption of intermolecular hydrogen bonds between the α -chains within a monomer is a major contributor to the observed rupture pattern. The discrete 22nm extensions may arise from stretching of *D*-periods (i.e. the 67nm banding region consisting of one gap region and one overlap region; see figure 2.3), a process that could be initiated by unfolding of the thermally labile domain of the gap region triggering a cooperative unfolding of the entire *D*-period [141]. There are approximately 250 amino acids per *D*-period with a native length of 67nm. The stretched length of an amino acid is 0.37nm giving a stretched *D*-period a length of 92.5nm, a difference of 25.5nm. This value is in agreement with the measured 22nm extensions, particularly if the tertiary helical structure is considered. Steric restrictions imparted by the intertwining of the individual α -chains will prevent them from being stretched to their full length. In light of the final extension being more than 100% of the original fibril length, it is unlikely that intermolecular hydrogen bond rupture is the only structural change occurring upon extension of a collagen fibril. It is quite likely that sliding between microfibrils (see figures 2.1c and 2.4) contributes to the observed length increase.

The long plateau at around 300pN in the relaxation profile (Figure 3.3 black traces and bottom panel) suggests that some of the

structural changes observed upon extension are reversible. Plateaus in force spectroscopy data provide useful mechanical information about structural changes occurring within a molecule submitted to tensile forces (see figures 1.11 and 1.13). In the current experiment, the plateau length is more than 100% of the extension at which it occurs ($\sim 1\mu\text{m}$). When single molecules are stretched, this type of feature is typically short compared to the total length of the polymer and is attributed to a conformational change within the molecule, such as the chair-boat transition in sugar rings, or bond rotation [52, 143]. Structural changes in the collagen monomers within the subfibrils occur axially upon extension and involve shear rupture of intermolecular hydrogen bonds, disruption of interstitial phosphate bonds [105] and sliding of microfibrils. Reformation of this ensemble of interactions occurs when the tension in the fibril is reduced to the threshold force of 300pN as evidenced by the long plateau in the relaxation profile. As structural equilibrium is regained during fibril relaxation, disruption of the interactions again requires a force of 2-4nN. Interestingly, structural equilibrium is regained within the time scale of a typical stretching experiment, which is approximately 1-5sec. It is worth noting that this is comparable to the time scale of a typical physiological response of the ECM during contractile loading.

The mechanical properties of single polymer chains can often be quantified using the worm-like chain (WLC) model, which relates the measured force to the extension through physical parameters such as the length of the molecule (contour length) and the persistence length. The structure of collagen fibrils suggests that the WLC model should be a good starting point to quantify their mechanical properties. However, attempts to fit different regions of the relaxation curve with the WLC model led to a persistence length 0.22nm resulting in an unusually low value of elasticity of 4.9Pa using the definition of the persistence length [63]:

$$p = \frac{E}{kT} I, \quad (3.1)$$

where E is the elasticity of the polymer, kT is the Boltzmann factor and I is the second moment of inertia ($I = (\rho/4)r^4$ for a right cylinder). The tensile strength for collagen arranged as tendon is reported to be 100MPa [63]. Since the WLC model assumes all contributions to polymer dynamics to be entropic in nature, it must be concluded that entropy contributes minimally to *in vitro*-assembled collagen fibril mechanics on the length scale investigated here. The collagen subfibrils investigated assemble primarily through

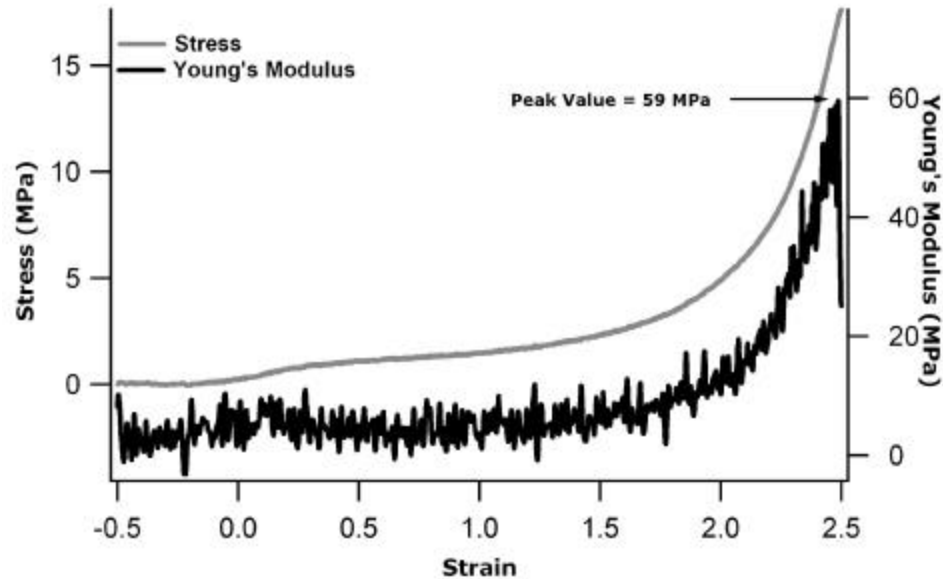


Figure 3.6. Stress versus strain plot (Gray trace) assuming a subfibril diameter of 20nm. Black trace is Young's modulus calculated from the stress/strain plot.

noncovalent interactions, allowing substantial axial reorganization during stretching (see section 2.1.5). This reorganization is believed to be enthalpic in nature and causes variation in the geometric parameters of the fibril that cannot be modeled with a standard model of polymer elasticity that assumes constant radius and purely entropic contributions to the elasticity of the chain. However, comparison of subfibril mechanics with macroscopic tendon mechanics can be achieved by evaluating Young's modulus from a stress-strain plot of individual subfibrils assuming a radius of 20nm (Figure 3.6). The Young's modulus determined from the stress strain curve undergoes major change during the fibrils' elongation and is characterized by a low elasticity regime followed by a much stiffer state of the subfibril at large elongation. The Young's modulus calculated from the large

elongation regime yields a value of 59MPa, which is consistent with the reported tensile strength for macroscopic collagen assemblies (~100MPa) where collagen fibrils are major contributors to the mechanical integrity.

3.1.3 Comparison of Wildtype and OIM Mouse Tail Collagen

Subfibrils and Fibrils

Diseases such as osteogenesis imperfecta (OI) have a significant effect on the mechanical properties of collagenous tissues [131, 144]. In order to study the changes that occur due to OI, a useful model mouse system, called osteogenesis imperfecta murine (OIM), has been developed [145]. Collagen was harvested from the tails of wildtype (wt) and OIM mice and reconstituted *in vitro*. Force spectroscopy experiments were performed as reported in section 3.1.2 with no modification of the AFM cantilever.

Data from stretching reconstituted mouse-tail fibrils is presented in figure 3.7(A&B). Noting that a transition in the relaxation profile occurs at approximately 1 μ m (Figure 3.7B) it is clear that a structure of subfibrillar length is being stretched. Overall, the force profiles for the wt-mouse subfibrils are qualitatively comparable to the profiles for

the model human subfibrils. A quantitative similarity is in the length of the transition, which is approximately 100% of the starting length (Figure 3.7B). However, there are notable quantitative differences from the model human subfibril data. Immediately apparent is the force at which the ruptures occur in the extension curve. Ruptures prior to the maximum extension occur at less than 200pN and the maximum force reached is about 800pN (Figure 3.7A). This is in sharp contrast to the maximum force of 6nN attained in the experiments

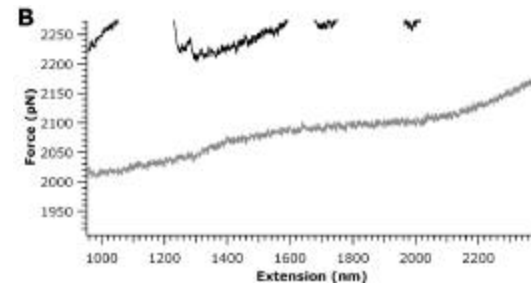
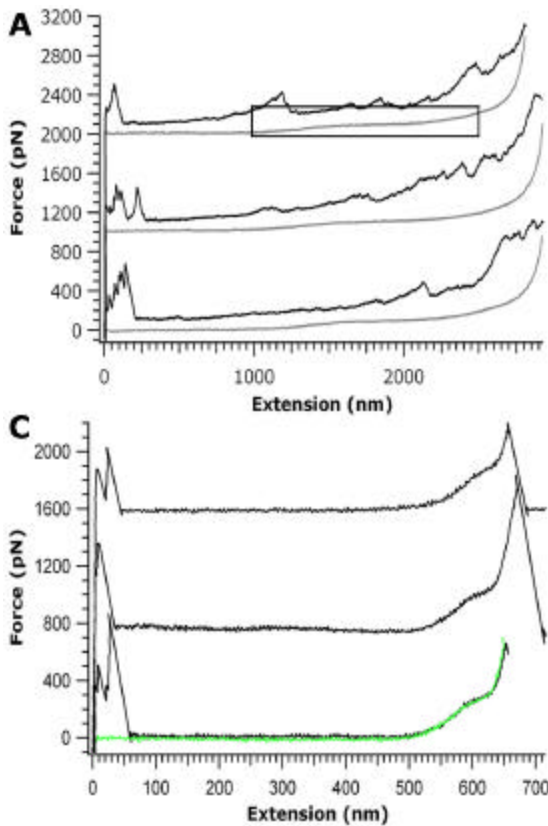


Figure 3.7. Representative curves for reconstituted mouse-tail collagen subfibrils. **A.** Wildtype mouse-tail curves. Note qualitative similarity to the model human subfibril data of figure 3.3 and the ruptures occurring at less than 200pN with a maximum force of 800pN. **B.** Enlargement of boxed region in (A) to emphasize plateau occurring at 80pN. **C.** OIM mouse-tail curves. Note the complete replacement of rupture events upon stretching with a short, smooth transition. Bottom curves are extension and relaxation curves demonstrating the transition is reversible and at equilibrium, given the absence of hysteresis.

with model human fibrils. Note that the events occurring prior to 300nm are nonspecific interactions between the tip and the substrate, a feature not visible in the model human subfibril data due to the large force at which extension-ruptures occur. The relaxation profiles also differ quantitatively, exhibiting a transition plateau at approximately 80pN (compare to 300pN for the model human subfibrils). The lower force is perhaps not surprising, first because collagen in a mouse would not be expected to endure the forces applied to collagen in humans. Second, and most important for the work presented here, the human collagen fibrils represent a model system that has been assembled through an artificial process from cultured collagen while the mouse-tail fibrils were *reconstituted* from collagen obtained directly from the animal. With this in mind, it is clear that the reconstituted fibrils will bear a greater similarity to fibrils found *in vivo* than will the model human fibrils. Assuming then that reconstituted mouse-tail subfibrils are valid representations of *in vivo* collagen, the force data for reconstituted wt mouse-tail subfibrils can be compared to data obtained from the OIM mouse.

The force profile for the OIM subfibrils is unique among the samples investigated. The striking absence of rupture events upon stretching indicates either the absence of intrafibrillar bonds that are

present in the wt fibrils, or more stable bonds that aren't disrupted when stretching these subfibrillar assemblies (Figure 3.7C). This data does confirm that there are reversible events upon stretching and, due to the lack of hysteresis between the elongation and relaxation traces, they occur at equilibrium. The curves in figure 3.7C have been normalized in length so that the transition occurs at the same extension. In actuality, the transitions begin between 550nm and 1 μ m, still on the subfibrillar length scale [100, 117]. Notably, the transitions are only an additional 15% elongation, a common value for *macroscopic* collagenous tissues. Additionally, the OIM subfibril transition occurs at a force of 200pN, closer to the model human subfibril data than is the wt mouse data. Possessing a short extension, a high transition force and a sharp force increase after the transition demonstrate the reduced elasticity of OIM collagen on a molecular scale in agreement with observations made in macroscopic tissue [97]. It is clear that subfibril-sized OIM collagen assemblies have low extensibility and a reduced number of disruptable internal bonds. It therefore seems likely that the transition plateau in the OIM subfibril data is primarily due to microfibrillar sliding within the subfibril (see figure 2.1c for a comparison of micro- and subfibrils).

In contrast to the data obtained with subfibrils, larger wt and OIM fibrils exhibit markedly similar force profiles (Figure 3.8). Measurement of the discrete extensions during stretching of both the wt and OIM fibril data resulted in values similar to those obtained for the model human subfibrils (Figure 3.9). The wt mouse-fibril data exhibits discrete extensions of 22.5nm and the OIM data a value of 18nm. Within the error of the Gaussian fits, these values are identical. The discrete ruptures in the OIM data are fewer and at a lower force than in the wt data, again suggesting there is a stabilizing element in the OIM fibrils that is absent from the wt fibrils. Since the fibrils are assemblies of subfibrils, there will be additional interactions between subfibrils stabilizing the larger structures. These additional bonds may

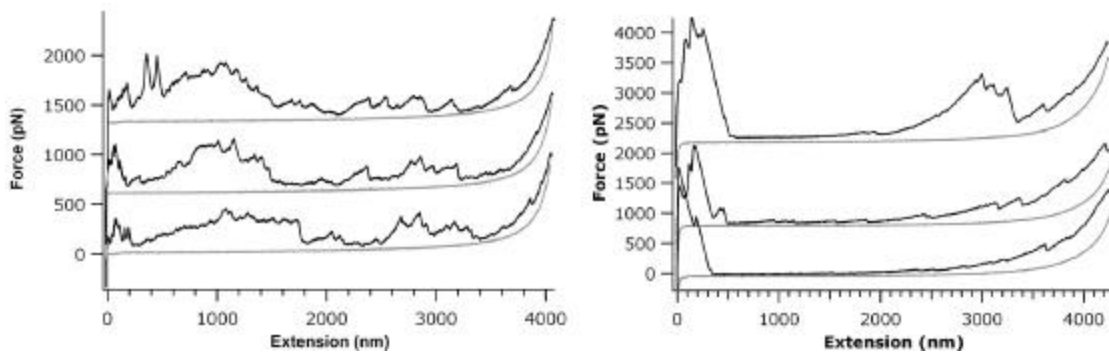


Figure 3.8. Force profiles for wt (left) and OIM (right) fibrils 2 μ m and 4 μ m long respectively. All profiles exhibit markedly similar features, with ruptures during extension (black curves) and smooth relaxation profiles (gray curves).

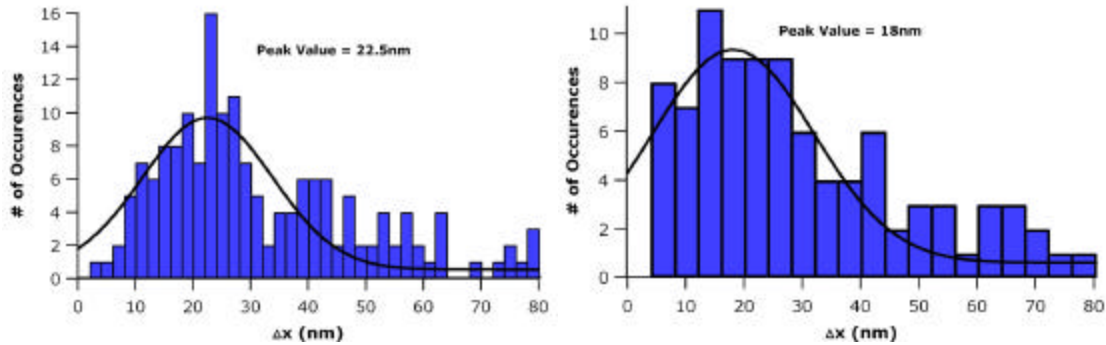


Figure 3.9. Histograms of discrete extensions for wt (left) and OIM (right) fibril data. Within the error of the fits, the values are the same and compare to the value obtained for the model human subfibrils.

be disrupted as the fibrils are stretched resulting in the observed rupture pattern (Figure 3.8B).

It is known that inorganic phosphates are required for collagen fibril formation [105, 146] and it is also believed that length, rather than cross-sectional diameter, imparts the observed mechanical properties to collagen fibrils [100]. The data presented here seem to demonstrate that length is a factor in collagen mechanics. It is likely that interstitial phosphate cross-linking is a necessary and sufficient component to promote longitudinal growth of fibrils, considering the pepsin treatment of the human collagen prior to assembly and that viable fibrils resulted (see sections 2.1.5 and 3.1.2).

Comparing the axial charge distribution for heterotrimeric collagen (i.e. wildtype) with the axial charge distribution for homotrimeric collagen (i.e. OIM), all charged regions of a homotrimeric *D*-period have an even charge while three of the seven positively charged

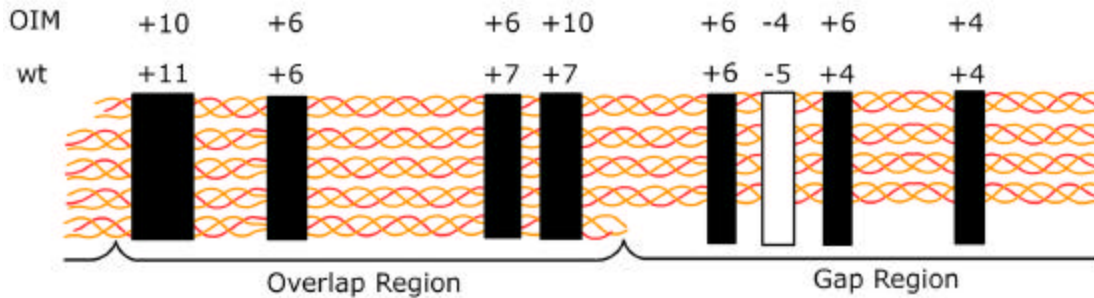


Figure 3.10. Comparison of axial charge distribution in homotrimeric (OIM) and heterotrimeric collagen (wt). Note there are only even positive charges in the homotrimeric collagen allowing more stable accommodation of divalent anions such as phosphates. Modeled after figure 8 in [105]

regions of a heterotrimeric *D*-period have an odd charge (Figure 3.10). Clearly an even number of positive charges can fully accommodate a number of divalent anions, while an odd number of positive charges leaves a charge on the anion free leading to a higher energy state and a possible trigger for unfolding of the fibrillar structure. Disruption of the phosphate bridges will almost certainly contribute to the rupture profile observed during stretching, and it is possible that the increased stability of the bound phosphates is responsible for the lower force and number of ruptures in OIM fibril data. As well, it is possible that the increased stability of interstitial phosphate cross-links accounts for the smooth, reversible transition observed for OIM subfibrils (Figure 3.7C). However, this does not explain the absence of a plateau in the fibril data.

A transition plateau in a force-extension profile is characteristic of a mechanical process occurring beyond the entropic regime.

Disrupted interactions in subfibrils are reformed during relaxation, as evidenced by the transition plateau, indicating that subfibrils regain their structural integrity in less than ~ 1.5 sec. Since the longer fibrils will have additional stability imparted by interactions introduced by the packing of subfibrils, the recovery time for fibrils would be expected to occur on a longer time scale. Since the extension ruptures reappear upon subsequent stretching of fibrils, the recovery time for fibrils is on the order of the experimental time scale. The absence of a plateau therefore suggests that the recovery process for fibrils may indeed require a longer time than for subfibrils.

3.1.4 Summary of Fibril Stretching Results

Force spectroscopy studies of model human collagen subfibrils (i.e. fibrils on the order of $1\mu\text{m}$ in length) and wildtype (wt) mouse-tail subfibrils resulted in qualitatively similar force-elongation profiles (figures 3.3 and 3.8A&B). Profiles for both exhibited discrete ruptures during extension and a long (100% extension) plateau during relaxation. Quantitatively, measurement of discrete extensions for both human and wt mouse subfibrils give the same value (22nm; Figures 3.5 and 3.9), suggesting similar structural changes are taking

place in both. However, features in the wt mouse subfibril profiles occur at lower force than features in the model human profiles indicating that mouse-tail subfibrils are more flexible than human subfibrils. Force-extension profiles for OIM subfibrils are strikingly different from the others in that they exhibit a smooth, reversible transition during elongation and relaxation (Figure 3.8C). The transition in OIM data occurs at 200pN higher than the 80pN of wildtype fibrils and closer to the 300pN of human fibrils, while the length of the transition is markedly shorter (15%). Extension data for wt subfibrils compares to data obtained on longer wt fibrils, while the relaxation profiles do not exhibit a transition plateau (Figure 3.8A). This observation suggests that within the time scale of the experiments (1.5sec), subfibrils regain their structural integrity while larger fibrils require more time to fully recover. Packing of subfibrils within fibrils will introduce intermolecular interactions that will prevent the fibrils from recovering in such a short time. Force-extension profiles for OIM fibrils qualitatively resemble profiles for wt fibrils. Discrete ruptures are observed during extension, but are fewer in number and occur at a slightly lower force than ruptures in wt fibrils, and there is no transition plateau during relaxation (Figure 3.8B). Measurement of the discrete extensions results in a value of 18nm,

comparing favorably to human and wt mouse data, again suggesting similar structural transitions are occurring. Intermolecular interactions introduced by packing of subfibrils may be responsible for the discrete ruptures in the extension profile. The reduced number, and lower force of the ruptures, and the smooth force profile seen for subfibrils may be a result of increased stability of interstitial phosphate bonds in OIM assemblies.

3.2 Exploiting Collagen Mechanics in the Production of a Self-Assembled Material

3.2.1 Motivation and Background

In section 3.1 the mechanical properties of reconstituted collagen fibrils were explored using AFM-based force spectroscopy. The relative stiffness of collagen fibrils makes them a useful choice in the production of self-assembled nanoscale materials. At its most fundamental level, the design of a supramolecular assembly that mimics naturally occurring biomaterials represents a considerable challenge to today's micro and nanoscience, and novel materials are now being designed on the microscopic and nanoscopic scales often

with the goal of providing support for tissue engineering applications. Scaffolds of biomaterials such as collagen are commonly utilized to induce the formation of tissues from dissociated masses of cells [147]. These scaffolds not only define the three-dimensional space for cells to colonize, but might also guide the development of appropriate functions. Natural extracellular matrix (ECM) molecules isolated from animal tissues such as tendon, bone and skin are often selected for the production of hybrid materials [148] because of their advantage of being readily recognized by biological systems [149]. DNA has proven to be a versatile biomolecule for the self-assembly of novel nanostructures. DNA-linked gold nanoparticle 3-D assemblies with controlled optical behavior [150] and self-supported, self-assembled 2-D DNA arrays [76, 151, 152] used as nanomechanical devices clearly demonstrate the power of the so-called bottom-up approach to build novel functional materials. Type I collagen, the most abundant protein in mammals, is extensively used as a biocompatible scaffolding material. The basic molecular unit of collagen-based materials is the triple-stranded helix 300 nm long and 1.5 nm in diameter. Under typical physiological conditions [104] collagen molecules readily self-assemble into fibrils hundreds of microns long with diameters ranging from 10 nm to 300 nm. Networks of collagen fibrils are strengthened

in vivo by intra-fibrillar enzymatic cross-linking of adjacent collagen molecules [115]. Artificial chemical cross-linking agents such as glutaraldehyde can be used to fabricate assemblies of collagen fibrils following a top to bottom approach into a variety of three-dimensional shapes and forms. These biomaterials have been intensively used in biomedical applications such as tissue engineering and wound healing [153-155]. Controlled assembly of molecules and macromolecules into self-supported 2-dimensional (2-D) materials still represents an important challenge in nanoscience and bioengineering. The availability of such materials will trigger a vast number of important new designs and applications. After mixing collagen fibrils, with a high bending rigidity, and negatively charged gold nanoparticles, spontaneous assembly of a self-supported 2-D hybrid nanostructure is observed.

3.2.2 Materials and Methods

Reconstitution of Collagen Fibrils

Collagen from rat tail tendon (type I, Sigma, St. Louis, MO) was dissolved at 1 mg/mL in 0.005 M acetic acid at 4° C overnight. The solution was diluted 1:1 with 2X PBS, resulting in a 0.5 mg/mL

solution, and placed in a water bath at 21° C. The temperature of the bath was allowed to increase to 37° C at which point the solution was returned to 4° C for storage [104].

Mesh Formation

Gold nanoparticles stabilized with [tris(hydroxymethyl)phosphine]-alanine (THA) [156] were obtained from the Nanomaterials Facility (University of Missouri-Columbia). 1 mL of a 10 or 20 µg/mL gold nanoparticle solution was added to 4 mL of a (0.5 mg/mL in PBS) collagen fibril solution (described above) to initiate formation of the collagen fibril mesh.

AFM Imaging

Samples were deposited on freshly cleaved mica discs (Structure Probe Inc., West Chester, PA) in 10 µL aliquots and allowed to adsorb for 20 to 25min, then rinsed extensively with 18MΩcm water (Millipore, Billerica, MA). Scans were acquired using a Nanoscope III (Digital Instruments, Santa Barbara, CA) in contact mode under ambient conditions.

3.2.3 Characterization of the Nanomaterial

The material has two components, *in vitro*-assembled collagen fibrils and water-soluble stabilized gold nanoparticles (AuNP). Using a bottom-up approach, AuNP and collagen fibrils (5 to 30 nm in diameter) were allowed to undergo a spontaneous self-assembly process leading to the formation of a 2-D mesh-like structure. Gold nanoparticles of well-defined diameter are available commercially, but when such AuNP were added to a collagen solution, AFM scans indicated minimal interaction between the AuNP and collagen fibrils. Production of AuNP using phosphine derivatives results in stabilized AuNP of controlled diameter [157, 158]. We used recently developed AuNP stabilized with ([tris(hydroxymethyl)phosphine]-alanine (THA, figure 3.11) [156], producing stable AuNP with a net negative charge arising from the carboxyl groups of alanine. When placed in the presence of these gold nanoparticles, reconstituted collagen fibrils assemble into large 2-D networks. The originality of the approach resides in the fact that the assembly process takes place in solution requiring no solid surfaces to act as two-dimensional templates, and can result in the formation of a macroscopic structure. This self-

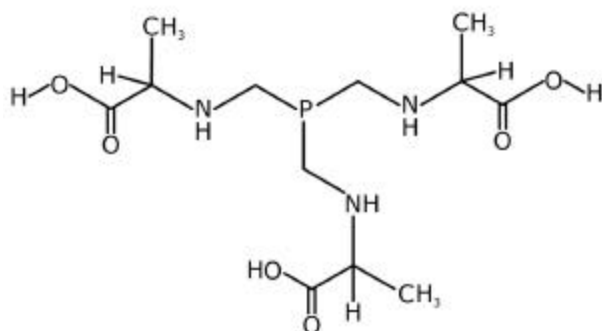


Figure 3.11. Chemical structure of THA used as the stabilizing agent in the synthesis of the gold nanoparticles.

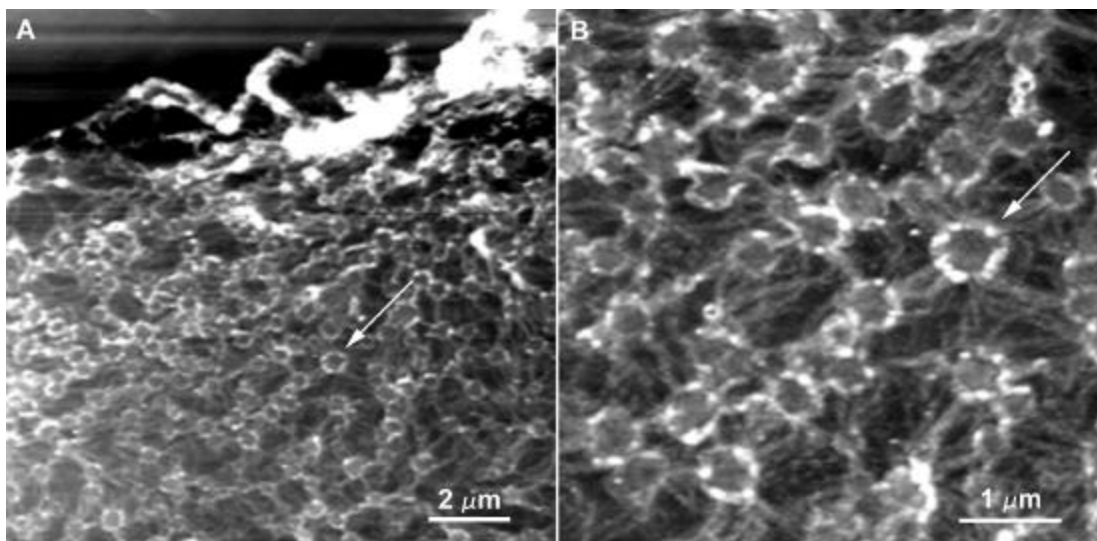


Figure 3.12. A. AFM micrograph (height mode) of a collagen fibril/AuNP assembly showing a two-dimensional network of collagen fibrils with a diameter estimated to be several hundred microns. The 2-D network self-assembles from a solution containing collagen fibrils and THA-stabilized gold nanoparticles (10 μ g/mL). The average thickness (30nm) is consistent with the diameter of individual collagen fibrils indicating the 2-D nature of the assembly. **B.** Enlargement of a region from (A). The collagen fibrils are arranged into a mesh-like structure interconnected by a network of fibrils. The density of the composite mesh appears to be rather low as indicated by the omnipresence of large gaps within the structure. The multivalent properties of the AuNP appear to be a stringent requirement for the mesh-like structure to assemble. The AuNP seem to organize the nodes creating discrete jumps in height. The arrows in both panels point to the same node.

nucleation and growth is particularly intriguing as it implies the ability of the 2-D network to behave as a self-supported macroscopic material.

Structural information on the composite collagen fibril/AuNP mesh was obtained from AFM imaging of the material extracted from the bulk solution and adsorbed onto a freshly cleaved mica substrate. A low resolution AFM micrograph showing a large collagen fibril/AuNP mesh with overall size estimated to be several hundred microns is presented in figure 3.12A. Deposition onto a glass slide revealed that

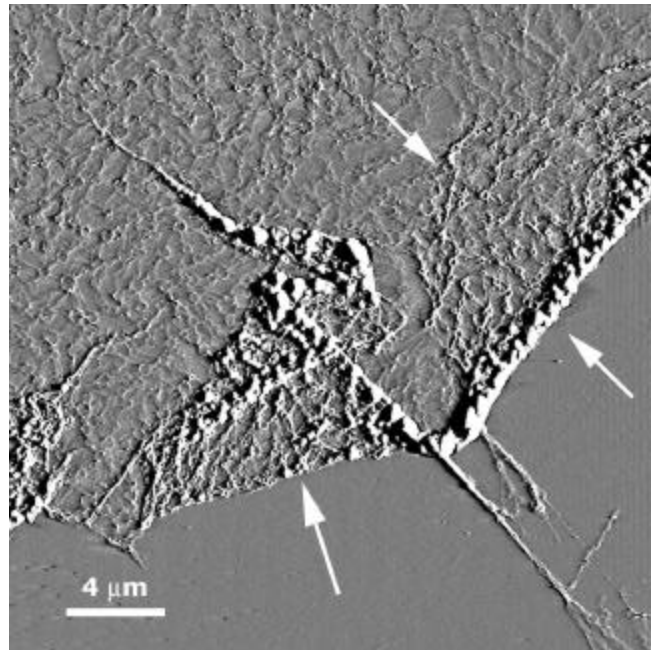


Figure 3.13. AFM micrograph (height mode) of a collagen fibril/AuNP assembly showing well-defined folds indicating that the 2-D structure was formed and stable in solution prior to its adsorption onto the mica surface.

the technique produces meshes as large as several hundred microns in diameter. The meshes have a nearly uniform thickness consistent with the diameter of the collagen fibrils (~30nm) suggesting the assembly is two-dimensional. A closer look at the sample reveals an organization with distinct node-like structures (see Fig 3.12B). The AuNP appear to act as cross-linking agents inter-connecting collagen fibrils through nodes ranging from 100nm to 500nm in diameter. Figure 3.13 reveals the occurrence of folds in the collagen fibril/AuNP mesh. Whether the folds occur in solution prior to, or during the process of adsorption, remains an open question. However, the presence of folds clearly indicates the assembly is two-dimensional, and was formed in solution. The two-dimensional assembly of collagen fibrils represents an important example of broken symmetry in matters of self-assembly. Other well-known self-supported 2-D structures include natural phospholipid cellular membranes, cellulose sheets composing cell walls and various artificial DNA assemblies [151, 152]. In these systems, hydrophobic and other intra- and intermolecular interactions are the driving forces allowing the assembly of a self-supported 2-D structure. In most artificial applications of 2-D self-assembly processes, an interface is required to act as a template and to provide, at least to some extent, the nucleation energy to drive the assembly [159]. The

stringent requirement of a solid/liquid, solid/gas, or liquid/gas interface for the self-assembly of monomolecular films prepared by conventional Langmuir-Blodgett related technologies limits their use as self-supported objects and somewhat limits their technological application.

In the case of the collagen fibril/AuNP mesh, the nucleation energy is charge-based. With a net negative charge on the AuNP, positively charged amino acids can bind to them irreversibly [160]. Since collagen fibrils contain many regions possessing a net positive charge [105], it is clear that a Coulombic attraction exists between the AuNP and the fibrils. With assembly of the mesh initiated by charge interactions, it remains to explain the preferential 2-D geometry. Constraint of the assembly to 2-dimensions likely arises from the mechanical properties of the collagen fibrils. This is perfectly reasonable considering that collagen fibrils of 15nm in diameter have a persistence length of approximately 1mm [63]. Since polymers behave as entropically rigid rods when observed at scales smaller than their persistence length, the collagen fibrils will be restricted in their flexibility and orientation on scales smaller than 1mm. The structural features present in the mesh are on a sub-micron scale and therefore in the rigid rod regime of flexibility. With this lack of flexibility, any

fibrils binding the mesh by at least two anchoring points would essentially behave like a rigid rod oriented parallel to the structure. In contrast, macromolecules such as polysaccharides or DNA have persistence lengths much smaller with typical values of 0.2nm and 50nm respectively [52, 63]. While 1-D and 2-D DNA/metal hybrid materials have been formed *in vitro*, these structures required significant manipulation in addition to a solid surface to control the molecular orientation [161, 162]. Attempts at spontaneous formation of composite materials by combining these polymers with AuNP or silica beads in the absence of a solid template systematically led to

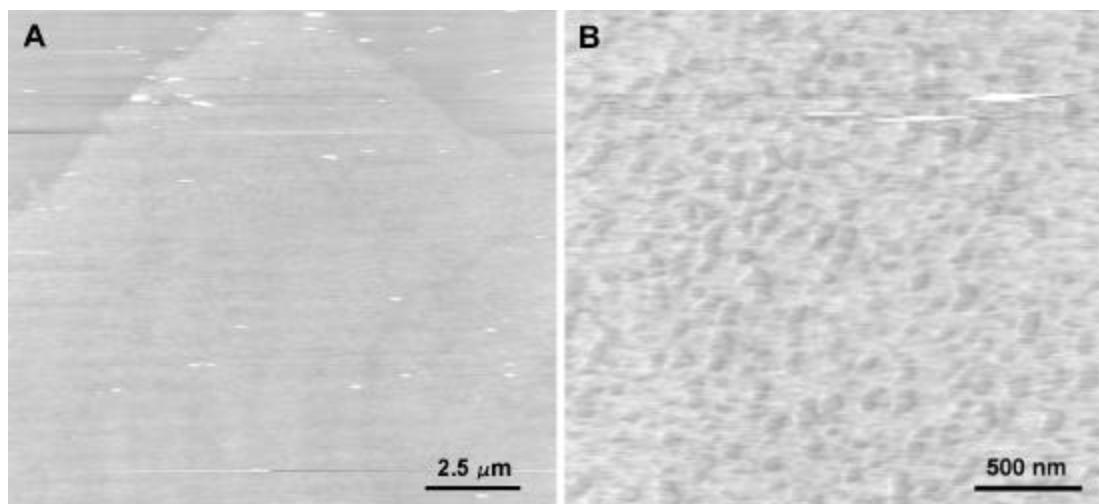


Figure 3.14. **A.** AFM micrograph (height mode) of a collagen fibril/AuNP assembly produced with a AuNP concentration of 20μg/mL, double the concentration used for the assembly presented in figures 3.12 and 3.13. At this scale it is clear that the mesh produced has a higher density as no nodes are obvious. **B.** Enlargement of a region from (A). The mesh-like structure is apparent at this scale as is the increased density of the assembly.

three-dimensional assemblies [150]. The three-dimensional growth is due to the high flexibility of polysaccharide and DNA chains allowing for a comparable growth rate in all directions.

Clearly, control over the growth process of the mesh is desirable, and control over the density of the mesh is indeed available by adjusting the initial concentrations of the solution components. The two scans in figure 3.14 show a mesh much higher in density than the one presented in figures 3.12 and 3.13. In this case the concentration of gold nanoparticles was increased to 20 μ g/mL leading to incorporation of more collagen fibrils into the mesh. This approach is the most practical for increasing the density of a mesh since an increase in collagen fibril concentration much beyond the 0.5mg/mL used here will result in a solution so viscous as to make incorporation of any other solute impractical.

In summary, stabilized, water-soluble AuNP and reconstituted collagen fibrils were used to generate a self-assembled 2-D mesh structure in solution. The AuNP play a central role in the assembly process as demonstrated by the higher density mesh created upon increasing the AuNP concentration in the initial solution. The multivalent nature and large size of the AuNP when compared to conventional cross-linking agents such as glutaraldehyde or poly-

maleimide make them desirable cross-linkers for the synthesis of composite materials. In these experiments, a phosphine-based stabilization agent incorporating the amino acid alanine was used to stabilize AuNP. Attachment of the AuNP to the collagen fibrils is primarily charge-based since there are several sections of net positive charge along the length of the fibrils [105] that will interact strongly with the negative charge on the AuNP [160]. The capability of cross-linking a large number of fibrils at particular points in space through individual AuNP appears to be a critical factor for 2-D assembly. Indeed, polymeric cross-linkers such as chondroitin sulfate invariably produce isotropic 3-D networks of collagen fibrils [155, 163]. This top to bottom approach has permitted considerable advances in the material sciences, particularly in bioengineering. However, it does not provide sufficient control over the assembly process to result in a 2-D construct. The 2-D network of collagen fibrils presented here resembles cross-sections of natural composite materials such as bone and various shells, as well as collagen networks associated with highly layered tissues such as the dermis and various basement membranes. Nano-scale 2-D composite materials made from collagen or other stiff biological fibrils, such as cellulose or actin filaments, could readily find applications in tissue engineering as a micro-scaled building block for a

variety of organs such as the skin and the vasculature. Using collagen meshes, one could envision the sequential assembly of organs from self-supported patches of cells in suspension.

CHAPTER 4:

Cell Membrane Mechanics: The Effect of the Glycocalyx and Intracellular Processes

4.1 Motivation and Background

Interactions between cells are vital in many natural processes as well as artificially generated tissue engineering environments. Particularly interesting are the forces involved in intercellular binding via binding proteins such as cadherins [164]. Knowledge of the intercellular

binding forces between specific cell binding proteins is of interest in developmental biology as well as tissue engineering research in which intercellular binding processes are vital to the successful generation of a viable biological system. Many specific cell binding proteins such as cadherins are transmembrane proteins and, consequently, investigation of intercellular binding forces between living cells requires intimate knowledge of plasma membrane mechanics. The plasma membrane of mammalian cells is a complex, dynamic structure constantly interacting with numerous proteins and other polymeric structures (Figure 4.1A). While much work has been devoted to the understanding of the dynamics of lipid bilayers, more attention to the plasma membrane of living cells is required to fully understand its

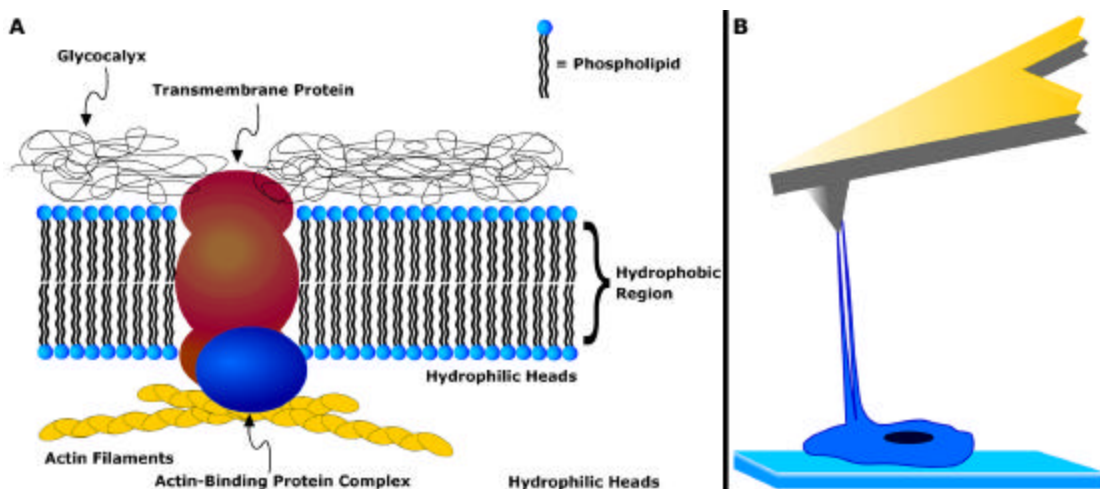


Figure 4.1. **A.** Schematic illustrating some important components of the plasma membrane. **B.** Schematic illustrating two membrane tethers being extracted from a cell.

contribution to the mechanics of tissues and any other associations of interacting cells.

The mechanical properties of the plasma membrane are vital to the regulation of many cellular functions, such as adhesion, migration, signaling and morphology [165]. The ability of these membranes to form tethers, thin nanotubes on the order of 10nm in diameter (Figure 4.1B), is an especially interesting phenomenon. Membrane tethers have been shown to participate in cell-cell adhesion [166] and recent studies suggest they might also provide a pathway for intracellular and intercellular communication [167-169].

A particularly dynamic process in which tethers form in vivo is the primary adhesion and rolling motion of activated leukocytes on vascular endothelial cells or platelets along the walls of blood vessels [166, 170, 171]. Such adhesion leads to the extravasation of activated white blood cells at the site of inflammatory reactions [172]. This process is an example of membrane tethers originating from pre-existing microvilli through a specific selectin/glycoprotein bond formation [173]. Recent findings provide evidence that tethers also exist on membrane bound structures inside cells [167], in particular the Golgi apparatus and endoplasmic reticulum (ER) [169]. With the

results of [168], these studies suggest the involvement of tethers in both intercellular and intracellular communication.

Tether formation is a ubiquitous phenomenon, having been observed between liposomes and readily formed in red blood cells [174, 175], neutrophils [176], neurons [177], fibroblasts [178, 179], and epithelial cells [180]. In experiments using optical tweezers, membrane tethers are generally observed as well-defined constant-force plateaus. Cells possess a significant membrane reservoir, a store of lipid bilayer that is accessed to maintain normal membrane tension in the event of mechanical stress on the cell, that is depleted through constant-velocity extraction of tethers resulting in the observed constant-force plateaus [178]. The actin cytoskeleton (hereafter cytoskeleton) is one macromolecular network associated with the plasma membrane (Figure 4.1A) that regulates the depletion of the reservoir primarily through its contribution to membrane tension [178]. Another macromolecular network that may contribute to membrane reservoir regulation is the glycocalyx (Figure 4.1A). It is therefore reasonable to assume that the effect of the glycocalyx, or any membrane-associated macromolecular network, on membrane mechanics could also be investigated through tether extraction. Upon depletion of the membrane reservoir, there will be a dramatic increase

in membrane tension and the contribution of the elastic properties of the membrane will become significant, resulting in an exponential increase in force [178]. Interaction of the membrane with the cytoskeleton has been investigated through tether formation using micropipette aspiration [174, 175, 181-184] and optical tweezers [180, 185, 186]. These studies showed that tether length (i.e. available membrane reservoir) and the force required to extract a tether are influenced by the various components of the cytoskeleton. Most often in these studies only single tethers are extracted, although a recent report indirectly demonstrated the simultaneous extraction of two tethers using micropipette aspiration [187]. Because of the technical limitations of optical tweezers and micropipette aspiration techniques, it is unlikely that they could reliably be employed to directly measure multiple tether extraction.

Intercellular binding interactions occur in many locations on the surface of a cell causing multiple perturbations of membrane tension, and creating the possibility for multiple tether formation. Two important issues regarding the extraction of multiple tethers are their ability to exist simultaneously without fusing and the potential that must be overcome to initiate extraction. Theoretical and experimental results provide evidence of tether fusion due to an attractive force

between the tethers during extraction from lipid vesicles [188, 189]. However, in the case of a living cell, the cytoskeleton and glycocalyx provide counter forces acting to separate the tethers, thereby diminishing the probability of tether fusion. One may view the attractive force between tethers as a surface energy minimization potential. The presence of this minimizing potential suggests that tether formation is not a spontaneous event. While application of a constant energy allows a single membrane tether to be extracted from the reservoir, *initiation* of tether formation requires a higher energy (i.e. a higher force), and therefore requires application of either chemical or mechanical energy [188, 190, 191] (Figure 4.2). Consequently, to initiate extraction of *multiple* tethers a force beyond the approximately 100pN accessible to optical tweezers is typically required. Investigation of multiple tether extraction therefore requires the use of a force actuator capable of overcoming such a potential yet sensitive enough to detect the piconewton-scale forces of tether extraction.

AFM-based force spectroscopy was previously employed to measure cell-cell interaction forces [192, 193] and plateaus visible in the data are acknowledged as indicative of membrane tether formation, but details of tether extraction are not addressed. The

broad range of forces accessible to the AFM (pN to nN) provides the opportunity to overcome the mechanical potential necessary to form multiple tethers and to measure the force necessary to extract a single tether. Using AFM-based force spectroscopy, tether formation and the effect of the cytoskeleton, glycocalyx and the drug thapsigargin on the mechanical properties of the plasma membrane were investigated in an immortalized endothelial cell line (EAhy926) [194].

The cytoskeleton provides a dynamic internal cellular scaffold regulating membrane tension by association through a variety of protein complexes. The influence of cytoskeletal integrity on the force needed to form tethers was investigated by measuring the effect of latrunculin A (LATA), an actin polymerization inhibitor [195-197]. Intracellular signaling processes may also affect cytoskeletal integrity. In particular, the drug thapsigargin is known to cause an increase in intracellular calcium ($[Ca^{2+}]_i$) in a signaling process triggered by inactivation of the ER-associated Ca^{2+} -ATPase [198]. Increased $[Ca^{2+}]_i$ will affect many cellular processes. Notably, it promotes the formation of actin filaments thereby strengthening the cytoskeleton [199], an effect detectable through an increase in tether extraction force. Externally, the cell membrane is covered by a glycosaminoglycan and proteoglycan network, the glycocalyx. The contribution of the

glycocalyx to membrane mechanics was investigated through the formation of membrane tethers by enzymatic cleavage of the glycocalyx backbone, the glycosaminoglycan hyaluronan.

4.1.1 Materials and Methods

Cell Culture

An immortalized endothelial cell line (EAhy926) was a generous gift of C. J. Edgell [194]. Cells were cultured in Dubelco's Modification of Eagle's Medium (DMEM, Wisent, Inc.) with 10% fetal bovine serum (FBS) at 37 °C for approximately 24 hours. Cells were seeded to minimize cell-cell interactions.

Cell Treatments

Disruption of the cytoskeleton was achieved by incubating cells with 1 μ M latrunculin A (LATA) at 37 °C for 30 min. The culture media was exchanged for media without LATA or FBS prior to tether-pulling experiments performed at room temperature (~24 °C).

Removal of the glycocalyx was accomplished by incubating cells with 500 U/mL of hyaluronidase at 37 °C for 30 min. The culture media was

exchanged for media without hyaluronidase or FBS prior to tether-pulling experiments performed at room temperature (~24 °C).

Detection of intracellular signaling was performed by treating cells with 200nM thapsigargin for 15min at 37 °C or room temperature (~24 °C). Time-course experiments were performed by treating the cells with 10⁻⁶ M thapsigargin at room temperature and beginning tether extraction experiments immediately.

4.1.2 Formation and Dynamics of Membrane Tethers

To show that tether formation between the AFM cantilever and the cells was indeed being achieved, endothelial cell membranes were functionalized with sulfo-NHS-biotin and incubated with streptavidin conjugated Q-dots (Quantum Dot Corp., Hayward, CA). The cells were then placed on an inverted epifluorescence microscope and probed with an AFM cantilever using a method similar to that employed in force measurements. The top edge of a cell was approached with the cantilever until contact was achieved. After several seconds of contact, the cantilever was retracted in the focal plane of the microscope so

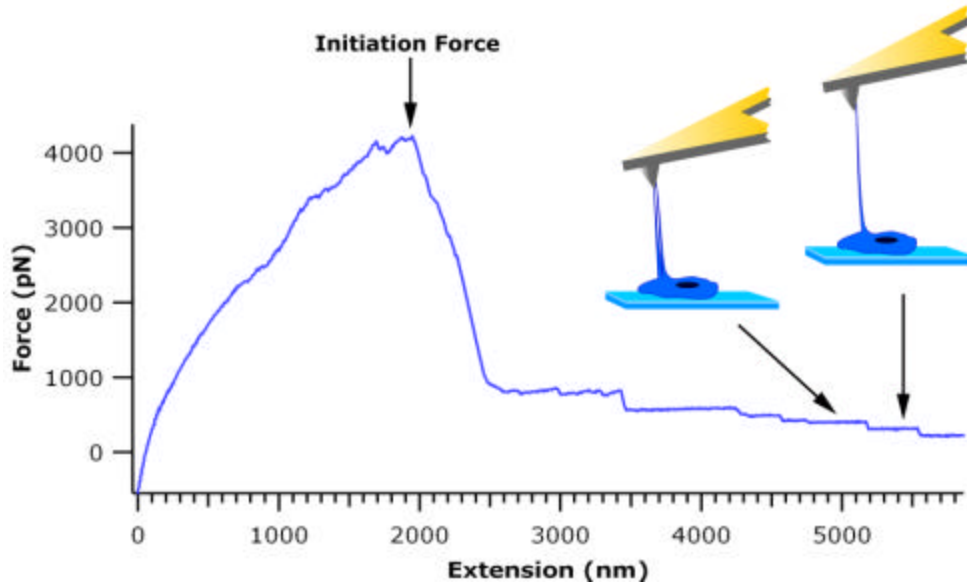


Figure 4.2 Schematics of an AFM tether pulling experiment illustrating the extraction of multiple tethers and a typical force profile.

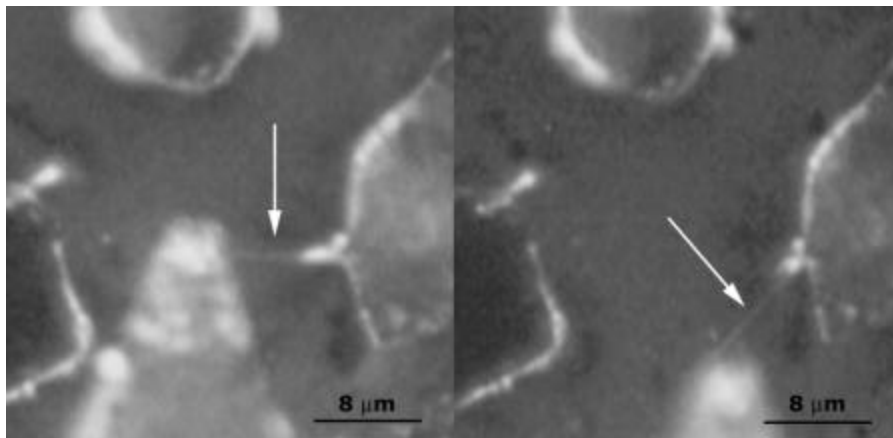


Figure 4.3. Tether formation in endothelial cells initiated by an AFM cantilever and visualized through fluorescent quantum dot labeling. Tether is identified by arrows.

that the tether could be seen. The extracted tether was approximately 8 μ m long and clearly formed a bridge between the cantilever and the cell (Figure 4.3).

In experiments performed with optical traps, plateaus in the force profile have been associated with the pulling of membrane

tethers composed of freely diffusing membrane components, mainly phospholipids and membrane proteins [178]. In AFM experiments, multiple constant-force plateaus separated by discrete force steps (ΔF) of comparable magnitude are observed along the entire extension (Figure 4.2). Such force profiles are characteristic of the simultaneous extraction of multiple membrane tethers attached to the cantilever via non-specific interactions (Figure 4.4), with the abrupt force steps resulting from a diminishing number of tethers remaining attached to the cantilever as the extension increases. Importantly, the exponential phase observed in optical trap experiments ascribed to the depletion of the membrane reservoir [178] is not present in AFM experiments. Therefore, it cannot be assumed *a priori* that the membrane reservoir is depleted at each force step, so the origin of the force steps must be determined.

Three possible explanations for the loss of tethers during pulling are tether rupture, tether fusion and detachment from the cantilever. Given the abrupt nature of the force steps, the most obvious assumption is that the tethers rupture. It is tempting to immediately dismiss this possibility under the premise that in order to rupture a tether, the lysis tension of the membrane must be overcome.

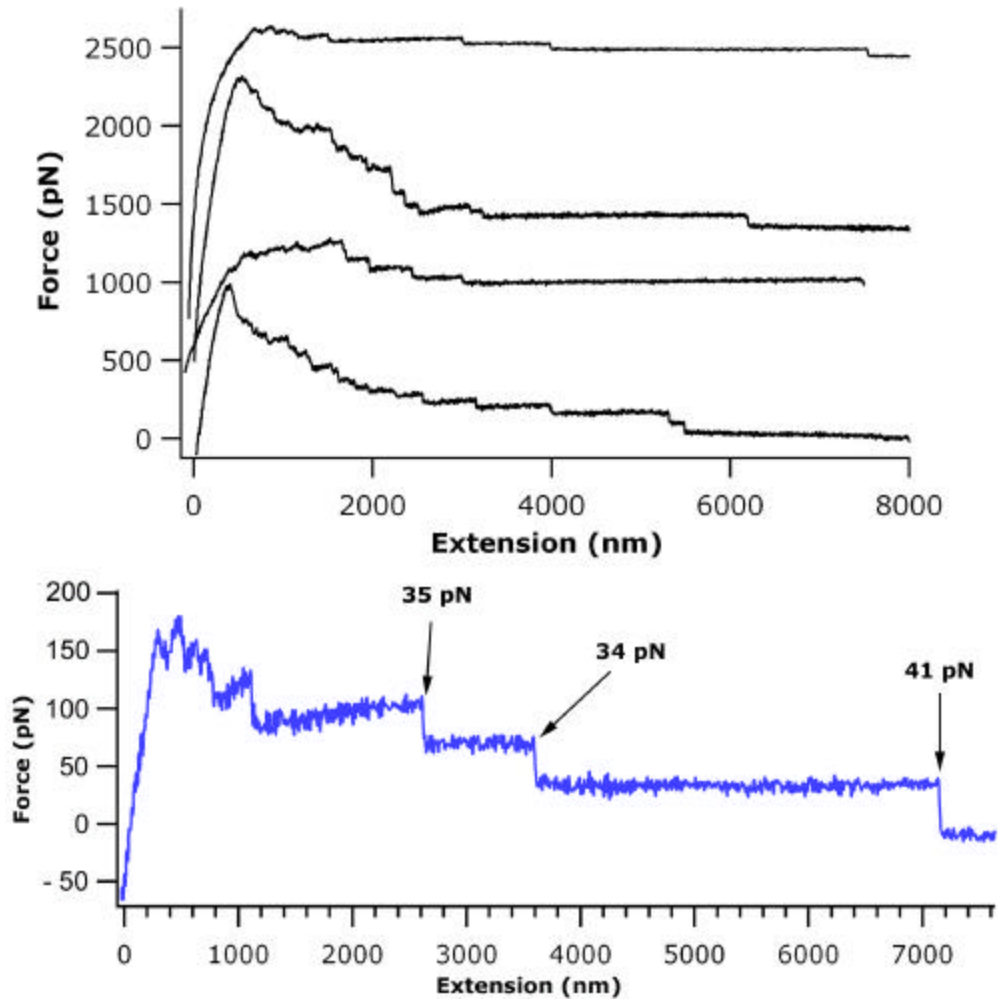


Figure 4.4. Typical force data for endothelial cells illustrating the consistent force values for the individual force steps.

Overcoming the lysis tension would result in forces on the order of 100 pN, more than three times the force measured here [177, 200]. However, one could imagine a severe curvature at the end of the tether attached to the cantilever. The more severe this curvature, the greater the material strain on the membrane and the greater the likelihood of rupture at a force below 100 pN. Rupture of a tether at forces below 100 pN might also be induced by proteins or other

macromolecular “contaminants” that may be present in the tethers [201]. It is natural to expect that these macromolecule-induced instabilities would be cell-type dependent and therefore detectable through differing DF values. However, experiments with five different cell types resulted in comparable DF values ([202] and unpublished data^{*}), suggesting that macromolecular “contaminants”, if present in the tethers, are not introducing instabilities leading to rupture. Additionally, tether rupture would be expected to leave a lipid residue on the cantilever. Fluorescence experiments have so far been inconclusive in demonstrating residual lipids on the cantilever tip. At present, it must be concluded that tether rupture is an unlikely source of the observed force steps.

A recent theoretical paper predicts an attractive force between tethers formed in membrane vesicles, resulting in tether fusion [188]. Experimental work measuring the forces and times involved in tether fusion demonstrated that in vesicles tether fusion is a function of extraction rate and the half-angle between the longitudinal axes of two adjacent tethers (Figure 4.5)[189]. The angle at which coalescence

* Three cell types were investigated in the cited reference. The remaining two types are L-929 cells (ATCC, Manassas, VA), and macrophages.

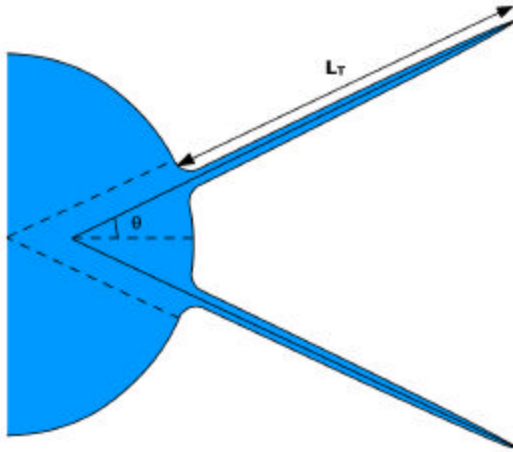


Figure 4.5. Schematic based on figure 5 in [189] showing the angle θ and the tether length. Extraction of tethers decreases the angle until it reaches a critical value (defined by equation 4.1) at which tether fusion occurs.

occurs was determined to be:

$$\theta = 2 \sqrt{\frac{R_t}{R_v \left(1 + \frac{R_v}{L_T} \right)}}, \quad (4.1)$$

where R_t is the radius of the tether, R_v is the radius of the vesicle, and L_T is the tether length. While the condition for tether coalescence appears to be a purely geometric argument, it must be realized that due to the viscoelastic nature of a membrane vesicle, a local perturbation will affect the curvature of the entire vesicle [188, 191]. This effect has also been demonstrated in optical trap experiments on living cells [178]. Pertinent to the extraction of two tethers is the fact that the presence of a second tether will affect the curvature of the membrane between the two tethers, and therefore the membrane tension, causing an attractive force between the tethers. This concept

can be extended to the case of multiple tether extraction by realizing that each tether will affect the mechanical behavior of all other tethers. A natural question that arises in considering equation 4.1 is how long it takes until the critical angle θ_c is reached. Again considering the viscoelasticity of a membrane vesicle, the time for coalescence to occur will depend on the scanning rate. The tether length, L_T , can be defined as the product of the scanning rate and time, $L_T = st$. With this definition, and solving equation 4.1 for t , the time for two tethers to coalesce is:

$$t = - \frac{\theta_c^2 R_v^2}{s(-4R_T + \theta_c^2 R_v)}. \quad (4.2)$$

For a given vesicle (or cell type), the only variant parameter is the scanning rate, s . Since the time for a tether to coalesce is a function of s^{-1} , it is clear that a 10 times decrease in scanning rate should result in a 10 times increase in the time required for two tethers to coalesce. The geometric parameters in equation 4.2 can be eliminated by comparing two scanning rates through the ratio:

$$t_2 = t_1 \frac{s_1}{s_2}. \quad (4.3)$$

Knowing two scanning rates and the time for coalescence of tethers at one of the scanning rates, the time expected for coalescence at the other scanning rate can be determined. This result was tested using the data from reference [189]. From direct observation of the data, at 100nm/sec tether fusion occurs in 15sec. Using this result and equation 4.3, at a scanning rate of 12.6nm/sec fusion should occur in 119sec for tethers extracted from a membrane vesicle. It remains to test the AFM data to determine if tether fusion is a possible origin for the observed force steps.

In order to maximize the time for the occurrence of tether fusion, force versus time scans of endothelial cells were made at constant extension. The piezo extension was halted near the apex of the initial hump (that is, at the apex of the tether initialization potential; Figure 4.6 Inset) to maintain a constant extension. Under this condition, the relaxation rate of the cell membrane becomes analogous to the pulling rate of a typical experiment. The relaxation rate was determined by converting voltage-time data to distance-time data using the calibration curve for the cantilever (with units of V/nm as described in section 1.2). Slopes were determined at the beginning and just prior to the last force step in several distance-time data

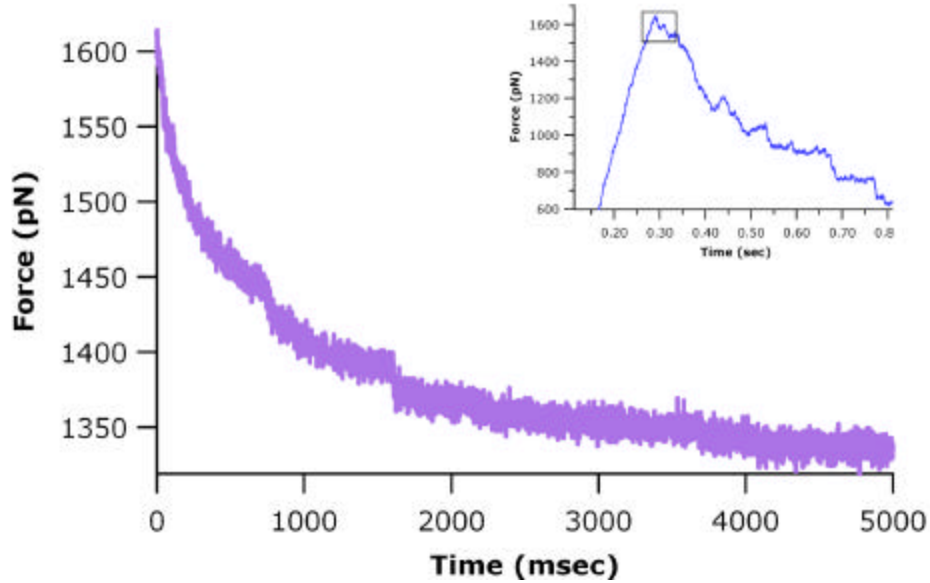


Figure 4.6. Constant extension scan showing multiple force steps within 5 sec, with several occurring within 1 sec. Inset is typical tether pulling data with a box indicating the apex region where extension was halted to acquire constant extension data.

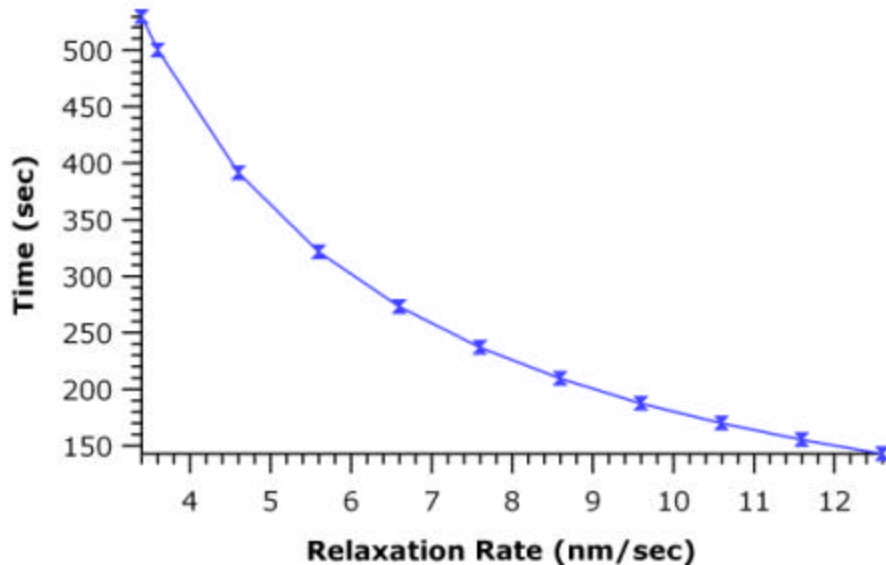


Figure 4.7. Time for fusion as a function of relaxation rate for constant extension data. The minimum time for tether fusion is 143 sec. The relaxation rate was determined by converting voltage-time data to distance time data using the calibration curve for the cantilever and subsequently determining the slopes near the beginning and end of the distance-time curves. Interstitial data was generated artificially by simply adding 1 to the previous data point until 12.6nm/sec was reached. *Note: second data point is 3.4nm/sec + 0.2nm/sec to simplify the data generation.*

curves to arrive at the maximum and minimum relaxation rates of 12.6nm/sec and 3.4nm/sec, respectively. These relaxation rates are substantially lower than the typical scanning rate of 6000nm/sec. The apex of the tether initialization force at 6000nm/sec is typically reached in 0.3sec (Figure 4.6 Inset). Using the highest relaxation rate in the constant extension experiments (12.6nm/sec) for s_2 , 0.3sec and 6000nm/sec for t_1 and s_1 respectively, and assuming no tether fusion occurs prior to 0.3sec (since no independent tethers should yet exist), the first fusion event should occur in no less than 143sec (Figure 4.7). However, in the constant extension experiments, all of the tethers appear to be released from the cantilever in less than 5sec (Figure 4.6), and no fusion event should be observed in such a short time. It is important to note that this conclusion was drawn based on data for tether fusion in pure phospholipid vesicles. Vesicles lack the complex scaffolding provided by the cytoskeleton and glycocalyx, which are present in living cells. These macromolecular networks regulate the motion of the membrane and will slow, if not prevent, the fusion process. Consequently, the 143 sec minimum determined above for the first fusion event is actually an underestimate of the time expected for such an event in living cells. Considering that the several force

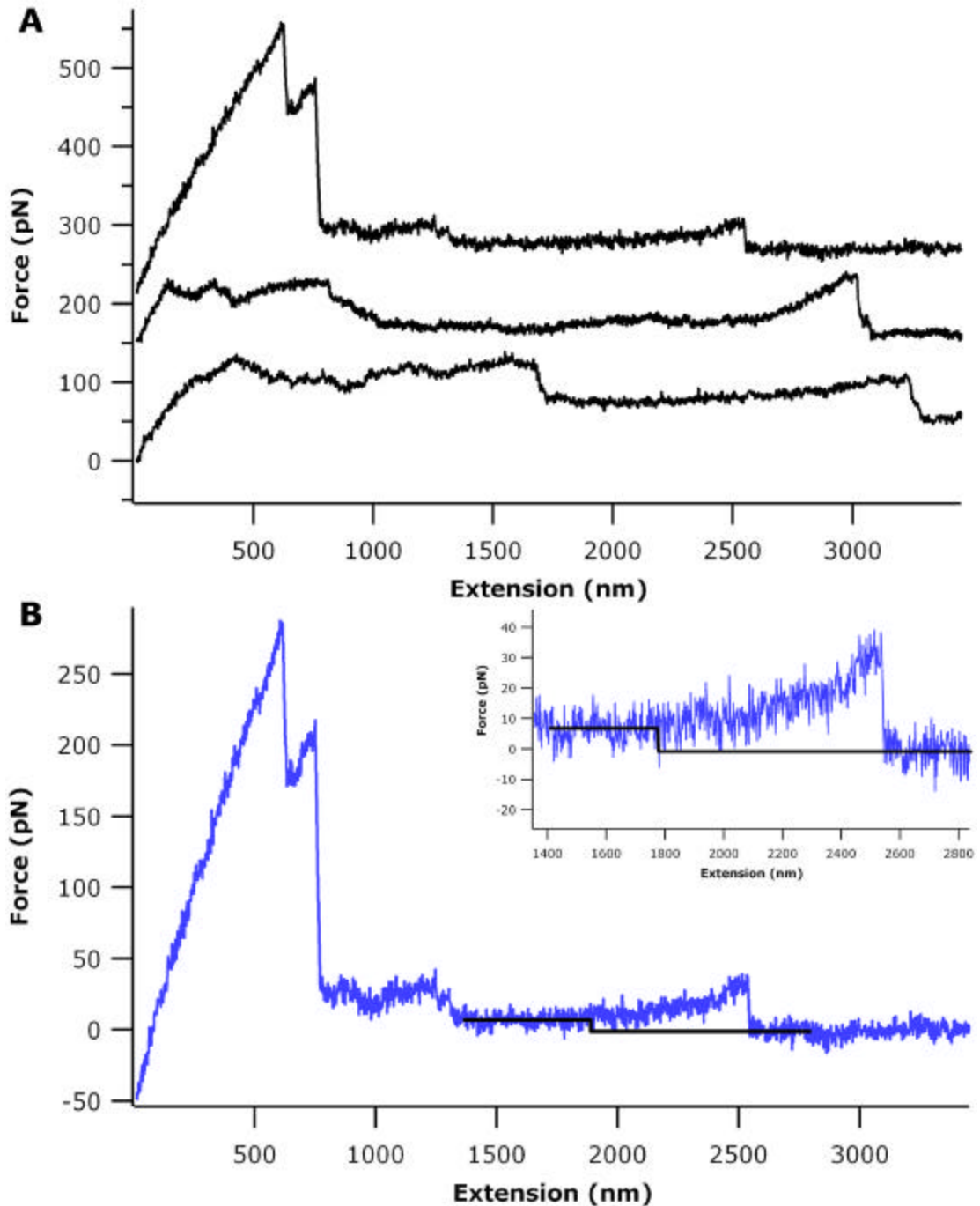


Figure 4.8. A. Force profiles recorded at 1000 nm/sec after hyaluronidase treatment to eliminate the glycocalyx (see section 4.1.1 for details). Force increases are seen immediately prior to most force steps at this scanning rate. **B.** Analysis of top curve in (A). Overlay on longest plateau is a schematic illustrating the profile that would be expected at 6000nm/sec. Inset is an enlargement of the schematic area to emphasize that there is a finite difference between the force on the plateau and the force after the force step.

drops in the constant extension experiment occurred prior to the underestimated time of 143 sec, it is unlikely that tether fusion is responsible for the observed force steps.

The remaining explanation is that the tethers detach from the cantilever. At a glance, "dropping" a tether appears to be a stochastic event. However, it is more likely that detachment would occur due to depletion of the cell's membrane reservoir. The plateaus are observed over several microns, a length consistent with tether formation that has been attributed the gradual depletion of the cell's membrane reservoir. In experiments using optical tweezers, depletion of the reservoir was directly observed as the onset of an exponential phase indicating that the elastic regime of tether mechanics had been reached [178, 180]. The exponential phase is not visible in AFM experiments performed at 6000nm/sec, but a short exponential phase is seen at the end of almost every plateau observed in scans performed at 1000nm/sec (Figure 4.8). Depletion of the membrane reservoir would result in an impulse being delivered to a tether by the force actuator being employed. Therefore, comparison of the optically trapped bead with the AFM cantilever should provide some insight into this possibility.

A likely reason for the absence of the exponential phase is that the force constants of the tether and the cantilever differ by four orders of magnitude, while the force constants of a tether and a bead in an optical tweezers differ by only three orders of magnitude. The force constant of a cell membrane was determined to be 2×10^{-7} N/m [203], and the approximate force constant for an optical tweezers apparatus is 2×10^{-4} N/m estimated from information in reference [178]. The beads used are $1 \mu\text{m}$ in diameter and the maximum force accessible is on the order of 100pN. To escape from the trap, the bead needs to move less than $0.5 \mu\text{m}$, so the approximate force constant is:

$$\frac{1 \cdot 10^{-10} \text{ N}}{5 \cdot 10^{-7} \text{ m}} = 2 \cdot 10^{-4} \frac{\text{N}}{\text{m}}. \quad (4.3)$$

The nominal force constant for the cantilever as provided by the manufacturer is 1×10^{-2} N/m, in agreement with numerous calibration measurements and 50X higher than the optical tweezers force constant. The force constants embody the intrinsic properties of the force actuators and are therefore static quantities. Stretching a macromolecule and pulling a tether are dynamic processes, so it is more useful to consider the temporal force response of the force actuators.

For an actuator with a force constant k flexed at a scanning rate r , the loading rate in units of N/sec is defined as [204]:

$$\dot{F} = kr . \quad (4.4)$$

For $r = 4000\text{nm/sec}$ (the pulling rate used in reference [178]), the loading rates for the optical trap bead and AFM cantilever are respectively, 0.8nN/sec and 40nN/sec . It is now worth considering the impulse that would be delivered to a tether by each actuator upon depletion of the membrane reservoir. Again using the data in reference [178], the impulse time can be estimated to be on the order of 100msec . Using the loading rate (equation 4.4), the impulse is given by:

$$J = \int_0^{0.1} \dot{F} dt , \quad (4.5)$$

and using the loading rate values for the optical trap and AFM the impulses are 4×10^{-12} Nsec and 2×10^{-10} Nsec for the optical trap and AFM cantilever respectively. For an impulse time of 100msec (as determined from figure 1d in [178]) these are the equivalent of applying the respective forces of 40pN and 2000pN to the tether, a 50X difference in force resulting from the 50X difference in force constants. If a scanning rate of 1000nm/sec is used for the AFM

experiment, the values become:

$$\begin{aligned} \dot{F} &= 10 \text{ nN/sec}, \\ J &= 5 \cdot 10^{-11} \text{ N sec}, \\ F &= 500 \text{ pN}, \end{aligned} \tag{4.6}$$

resulting in a force only 12X higher than the optical tweezers impulse force. Table 4.1 summarizes the values for the different impulse parameters discussed here. From the values presented in the table, it is apparent that at a high scanning rate the AFM has the potential to deliver an impulse force 50X higher than the optical tweezers. In contrast, at a relatively low scanning rate of 1000nm/sec, the impulse force delivered by the AFM is significantly lower suggesting that different observations might be expected at a low scanning rate.

Considering that increases in force are observed at 1000nm/sec in keeping with features in optical tweezers data attributed to reservoir

Table 4.1. Summary of impulse values discussed in the text.

Instrument	Force Constant (N/m)	Scan Rate (nm/sec)	Loading Rate (nN/sec)	Impulse Force (pN)
Optical Tweezers	2×10^{-4}	4000	0.8	40
AFM	1×10^{-2}	4000	40	2000
		1000	10	500

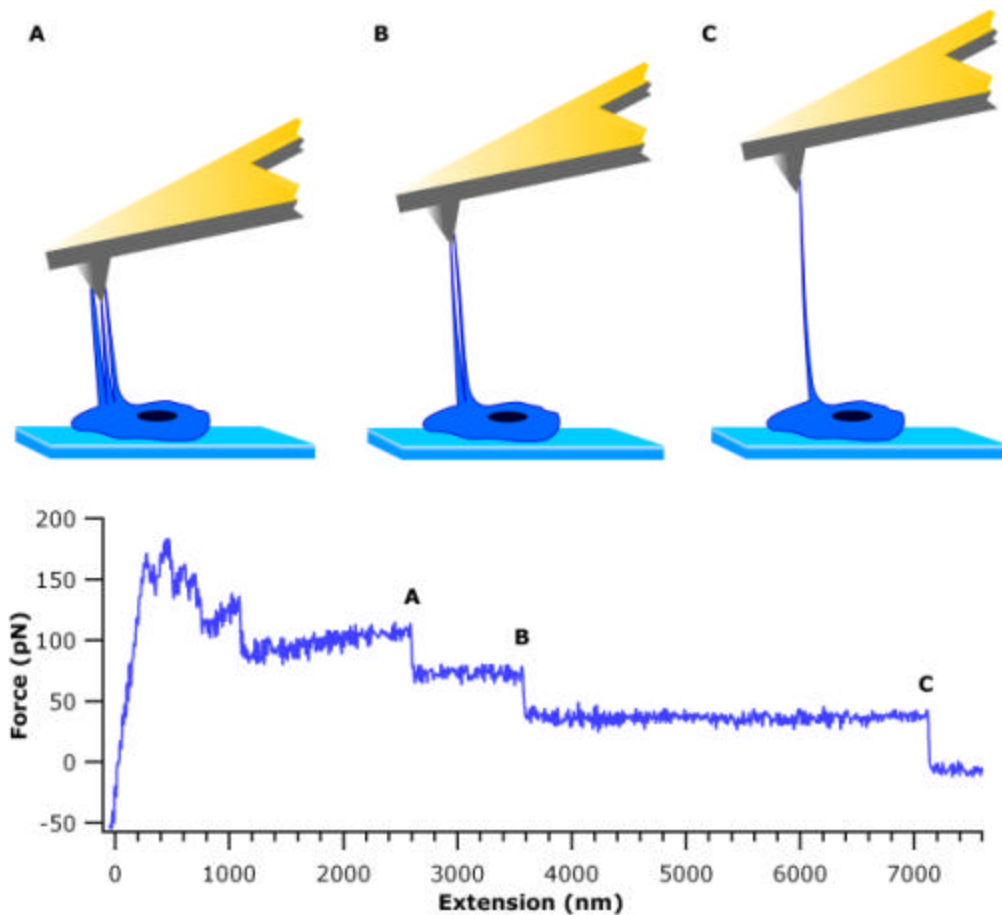


Figure 4.9. A force curve from figure 4.3 with schematics showing the number of tethers attached at each plateau. The measured lengths provide evidence that the reservoir is depleted at each step. Summary values are: $C = 7.81 \text{ m}$, $B = 2 \times (3.6) = 7.21 \text{ m}$, $A = 3 \times (2.4) = 7.21 \text{ m}$.

depletion, and that for an impulse to be delivered to a tether something sudden must occur to stop its extraction, it is quite likely that reservoir depletion is the primary cause of the observed force steps. Tethers dropped from the cantilever will be reincorporated into the reservoir [177] and, assuming reservoir depletion causes the force steps, should provide further evidence of reservoir depletion.

The magnitude of the force steps, \mathbf{DF} , is the force needed to pull a single tether and the total force at which a given plateau occurs ($\mathbf{DF}_t = n\mathbf{DF}$) corresponds to the force necessary to pull n tethers. Assuming all of the tethers extracted in a single experiment are from the same reservoir, the size of the reservoir will correspond to the extension at which the last force step occurs. This assumes no tethers remain attached after the final force step. The second to last force step will occur at a length corresponding to $\frac{1}{2}$ the size of the reservoir since two tethers will be attached, and so on. The size of the membrane reservoir can then be calculated:

$$L_R = n(\text{extension}), \quad (4.7)$$

where L_R is the size of the reservoir. Figure 4.9 shows a force curve and schematics illustrating the detachment of three tethers. This is an example of the situation where all tethers have been dropped. Frequently, due to the limited extension of the instrument, one or more tethers will remain attached to the cantilever. In such cases, the error in the calculations increases dramatically as it is difficult to determine exactly how many tethers remain attached. If the tethers are not all dropped, the cantilever cannot return to its equilibrium position at the end of data acquisition and it is extremely difficult to determine the level of zero force. It is therefore not always reasonable

to use this length analysis as a means to measure the absolute size of the membrane reservoir. However, the fact that it works well in the cases where zero or a couple of tethers remain attached to the cantilever does suggest that the reservoir is being depleted and this is a likely source of the increase in tension causing the tethers to be dropped.

4.2 Influence of the Cytoskeleton, the Glycocalyx and Intracellular Signaling on Tether Formation

4.2.1 Tether Forces, the Cytoskeleton and the Glycocalyx

The force required to extract a tether from a membrane vesicle at a scanning rate of $6\ \mu\text{m}/\text{sec}$ is on the order of 10pN [205]. The primary origin of this force was proposed to be friction caused by slippage between the membrane leaflets due to the high curvature at the tether-membrane junction (Figure 4.10) [205]. Because of the macromolecular networks surrounding the membrane in living cells (i.e. the cytoskeleton and glycocalyx), the force required to extract tethers from cells is approximately 30pN . The precise contributions of the cytoskeleton and glycocalyx are still being explored, but one likely

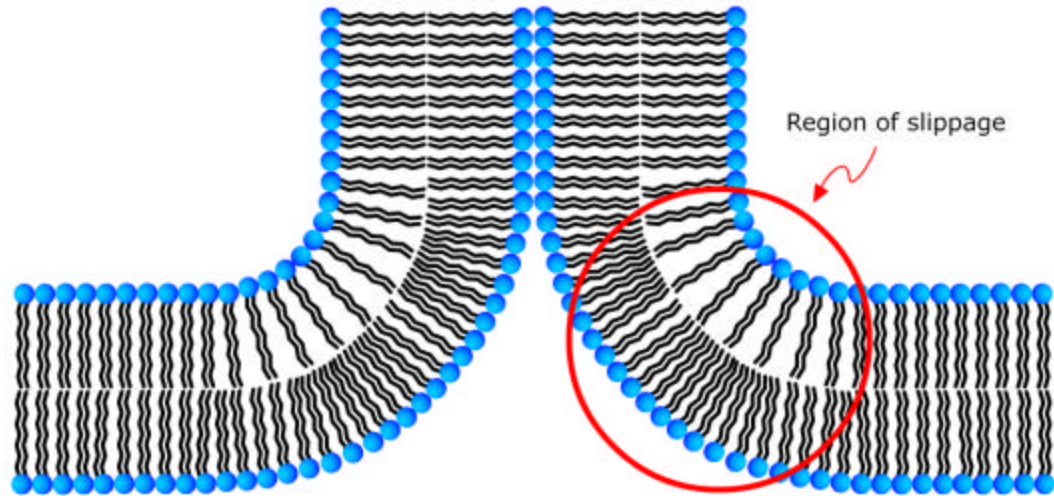


Figure 4.10. Illustration of region where leaflets slip during tether extraction.

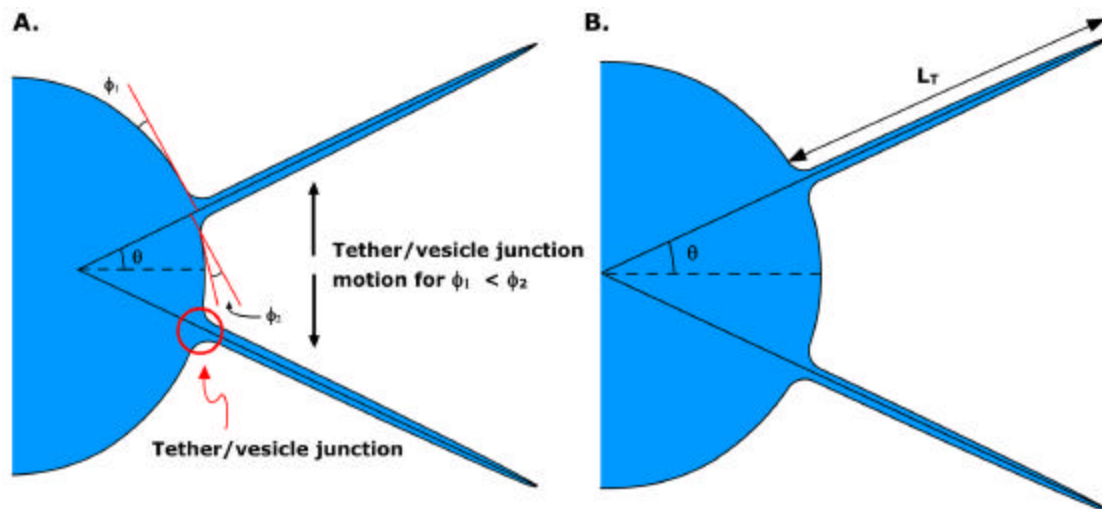


Figure 4.11. **A.** Schematic showing one nonequilibrium position and tether/vesicle angles defining motion of the junction. **B.** Schematic showing tether/vesicle junction equilibrium position. Once this equilibrium position is attained the angles ϕ_1 and ϕ_2 will no longer change. The angle θ will continue to change until it reaches the critical value of θ_c when the tethers will fuse.

contribution is the restriction of tether/plasma membrane junction motion along the cell surface.

When the tether axis is perpendicular to the vesicle surface the tether/vesicle junction is in equilibrium (Figure 4.11A). During extraction of a tether from a vesicle, if the tether axis is not perpendicular to the vesicle surface, it will move along the surface until it is (Figure 4.11B). In a living cell, this motion will be inhibited, in part, by the cytoskeleton, which is bound to the membrane through membrane-associated proteins. Binding to this internal scaffold will restrict motion of the membrane in all directions. Additional restrictions are provided by the glycocalyx, which is also bound to the membrane through membrane proteins. This external scaffold forms a semipermeable layer on top of the cell membrane, restricting motion in all directions, although it will have the greatest effect restricting lateral motion of membrane tethers. The effect of these macromolecular networks was investigated through comparison of tether forces recorded for untreated, latrunculin-A (LATA) treated and hyaluronidase treated endothelial cells.

Tether extraction from endothelial cells was performed at room temperature on many different cells. A histogram of tether forces

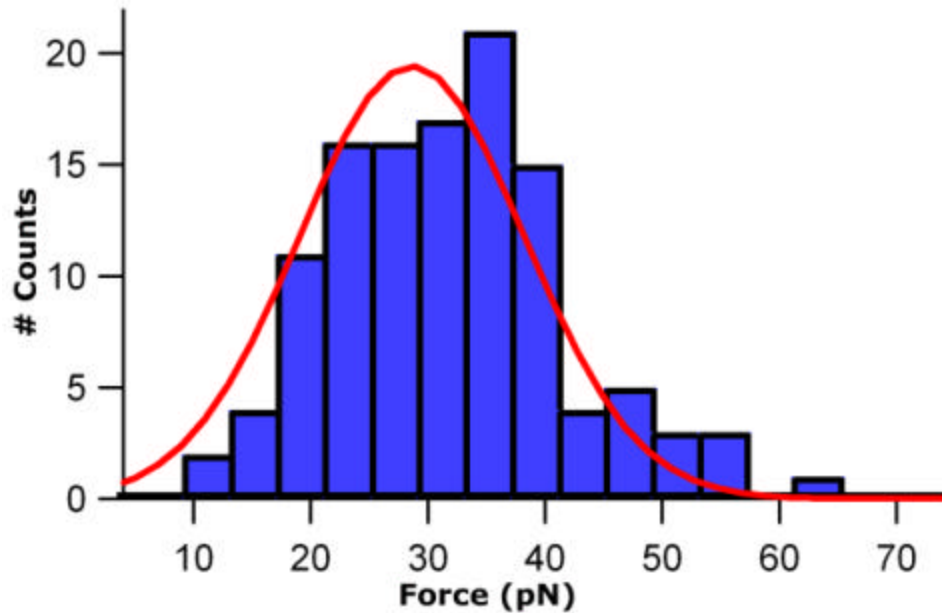


Figure 4.12. Histogram of the tether forces for untreated endothelial cells. The tether force determined by the Gaussian fit is $29 \pm 10\text{pN}$.

measured between distinct plateaus, ΔF , for untreated endothelial cells is presented in Figure 4.12. Identification of the pulling force of a single tether was accomplished using a Gaussian fit giving a value of $29 \pm 10\text{pN}$. The broad distribution of the forces observed in the histogram likely arises from heterogeneities in the mechanical properties of the membrane at the cell surface that are introduced by the cytoskeleton and glycocalyx.

Confirmation that the influence of the cytoskeleton is measurable using the AFM required disruption of the cytoskeleton and its association with the membrane. It is well known that treatment of cells with LATA will disrupt the actin cytoskeleton (Figure 4.13, left

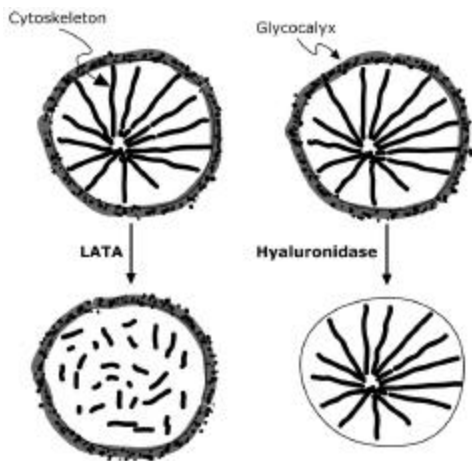


Figure 4.13. Schematics of cells showing the effect of latrunculin-A treatment (left) and hyaluronidase treatment (right) on the cytoskeleton and glycocalyx respectively.

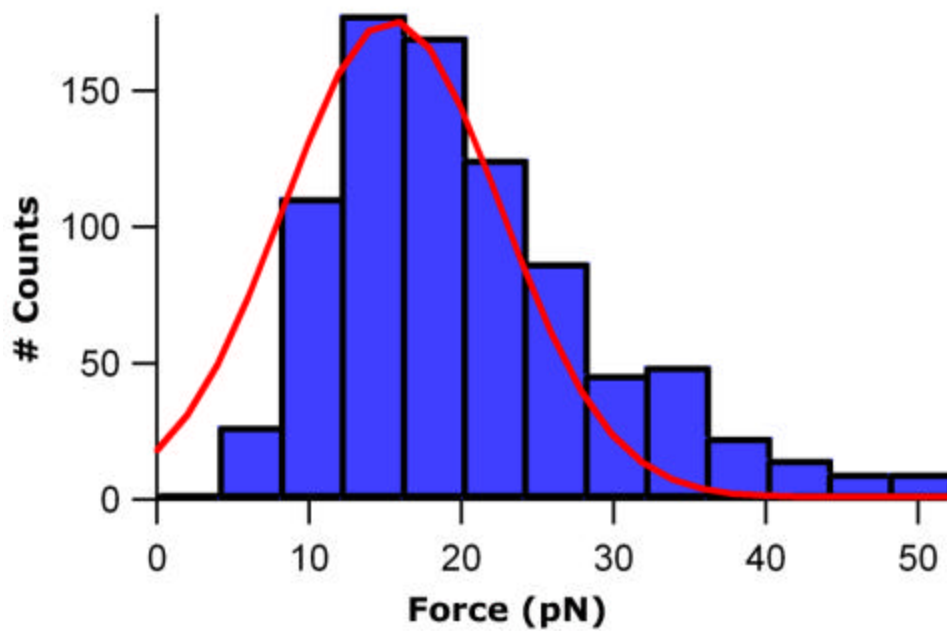


Figure 4.14. Histogram of the tether force for 1 μM LATA treated endothelial cells. The tether force of 15 ± 6 pN (determined by the Gaussian fit) is approximately 50% of the force measured for the untreated cells. The distribution of forces is also notably narrower.

illustration) leading to significant changes in overall morphology [195, 196, 206]. Importantly, after LATA treatment, transmembrane proteins (e.g. cadherins, integrins) lose their attachment to F-actin [207, 208]. Treatment with LATA will therefore result in the decoupling of the actin cytoskeleton from the plasma membrane. This effect is evident from the rounding of the cells and is also manifest in the reduced magnitude of the observed tether force (Figure 4.14). After treatment, the tether force at room temperature was measured to be 15 ± 6 pN, a reduction of approximately 50% from the untreated value of 29 ± 10 pN. The 8 pN change in width (± 4 pN) given by the Gaussian fit demonstrates that the cytoskeleton introduces a heterogeneity into the mechanical response of the plasma membrane to an external force. The decrease in force is consistent with previous studies [180] and clearly demonstrates that AFM tether force measurements can be used to directly probe changes in the association of the cytoskeleton and the membrane.

Investigations of cell membrane mechanics often focus on the influence of the cytoskeleton ignoring the influence of the glycocalyx. Intuition suggests that due to its association with the plasma membrane, the glycocalyx must have an influence on membrane

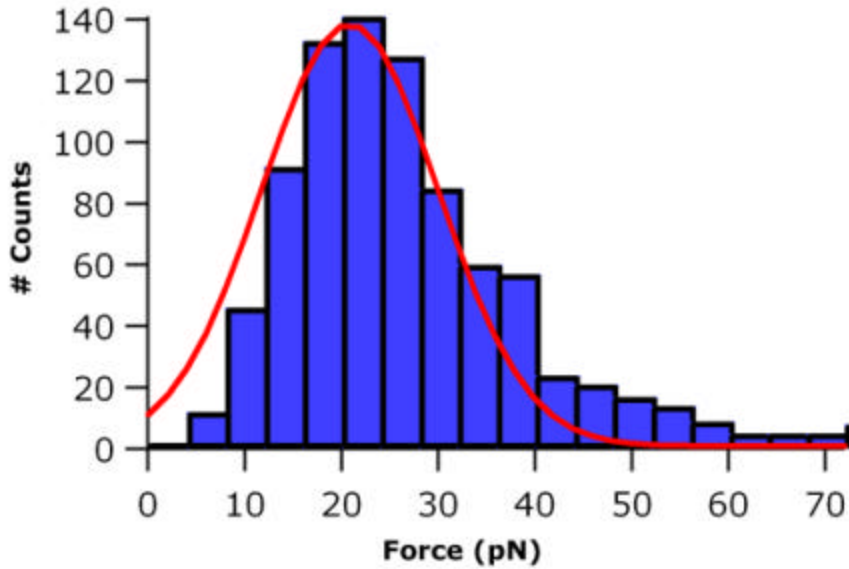


Figure 4.15. Histogram of the tether force for hyaluronidase treated endothelial cells. The tether force of 21 ± 10 pN (determined by the Gaussian fit) is reduced by approximately 30% from the force measured for untreated cells. The force distribution is not notably narrower.

mechanics. It is also important to note that the force profiles recorded in these experiments are reminiscent of data obtained by peeling a polymer from a surface [209]. To confirm that tethers are being extracted and that the force profiles are not the result of peeling a polymer from the cell surface, the macromolecules forming the glycocalyx were removed. The backbone of the glycocalyx is the glycosaminoglycan hyaluronan. The enzyme hyaluronidase cleaves hyaluronan into disaccharides, which in the present case is equivalent to digesting the glycocalyx (Figure 4.13 right illustration). Qualitatively, the force profiles after hyaluronidase treatment were unchanged suggesting that the profiles for untreated and LATA treated cells are not the result of peeling polymers from the cell surface.

Quantitatively, the tether force measured after hyaluronidase treatment was 21 ± 10 pN, approximately 30% lower than for untreated cells (Figure 4.15). This result demonstrates that the glycocalyx contributes significantly to cell membrane mechanics, although the effect is less dramatic than that of the cytoskeleton. Notably, the width of the histogram after hyaluronidase treatment is unchanged compared to the histogram for untreated cells, while the LATA histogram exhibits a significant change in width. It is worth discussing the possible origins of the spread of forces in these histograms.

It is not surprising that with intact molecular scaffolding a membrane tether would face its greatest dynamical restriction. In untreated cells, tether dynamics are regulated by the cytoskeleton and glycocalyx, while after removal of either the glycocalyx or cytoskeleton the entire regulatory role is filled by the remaining molecular scaffolding. While the average force results from interactions between the membrane and the cytoskeleton and glycocalyx, the width of the peaks arises from heterogeneities imparted to the cell membrane by these molecular scaffolds. One likely source of the heterogeneity is asymmetry in the tether pulling geometries (Figure 4.16). Only one possible geometry is illustrated in figure 4.16, but there will clearly be

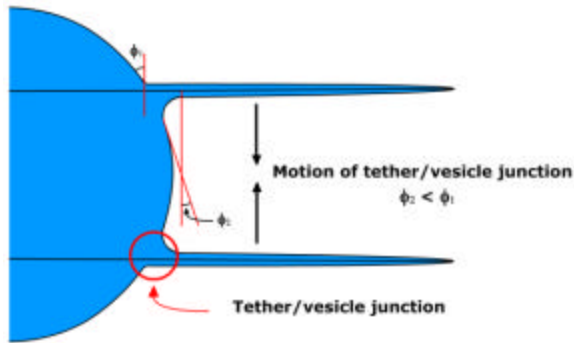


Figure 4.16. Schematic of one likely tether pulling geometry in an AFM experiment.

many different tether orientations due to the shape and size of the cantilever tip. Recalling the dynamics discussed in section 4.1.2, the tether/cell junctions will tend to move along the surface of the cell toward the equilibrium geometry in which the tether axes are perpendicular to the cell surface. Restriction of motion due to the cytoskeleton and glycocalyx will increase the pulling force above the force required for tether extraction from pure lipid vesicles by limiting motion of the tether/cell junctions through frictional effects due to the cytoskeleton and lateral tension provided by the glycocalyx.

Variations in the pulling geometry will result in variations in the pulling force leading to broadening of the histogram. Considering that the widths of the histograms for untreated and hyaluronidase treated cells are approximately the same, it must be concluded that the cytoskeleton imparts the greatest restriction of tether/vesicle junction motion. Indeed, removal of the cytoskeleton through LATA treatment reduces the spread of measured forces demonstrating that the

glycocalyx has minimal effect on tether/cell junction motion. This result is not surprising considering the compressibility of the glycocalyx and its reported intercellular lubricating effect [60]. In addition to the bonds between the cytoskeleton and the plasma membrane, it is likely that a significant contribution of the cytoskeleton to the tether force is due to curvature imparted to the membrane through regulation of the membrane reservoir. Such an additional curvature would promote interleaflet slippage of a nature similar to the slippage responsible for the 10pN required to extract a tether from a membrane vesicle as illustrated in figure 4.9.

The histograms presented in figures 4.12, 4.14 and 4.15 represent forces measured between plateaus at each force step resulting in a Gaussian average force for extraction of a single tether. Measurement of the forces between the baseline ($F = 0$) and each plateau will result in a multi-peak histogram with peaks separated by the average forces shown in figures 4.12, 4.14 and 4.15, for the respective cell states. As an example, extraction of multiple tethers from a pure phospholipid vesicle would result in force peaks at 10pN, 20pN, 30pN etc. Histograms of untreated, 0.5 μ M LATA treated and 500units/mL hyaluronidase treated endothelial cells are presented in figure 4.17. Although slightly obscured due to the spread of forces

discussed above, the histograms of figure 4.17 clearly exhibit multiple peaks separated by the Gaussian average tether force for each particular state of the cell.

Since the cytoskeleton and glycocalyx are mechanically coupled through mutual association with transmembrane proteins, their contributions to membrane mechanics will be convoluted making determination of specific contributions quite difficult. However, the current goal is to demonstrate that multiple membrane tethers can be extracted from living cells and that such measurements can provide information about the influence of any membrane associated macromolecule affecting membrane mechanics. Therefore, whatever *specific* contributions the surrounding scaffolds make to membrane dynamics, the histograms in figure 4.17 provide further evidence that

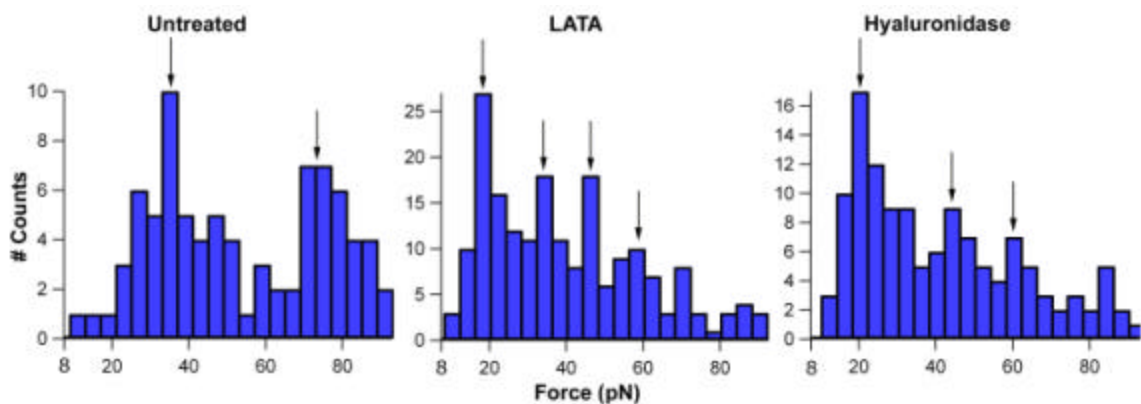


Figure 4.17. Multiple peak histograms for the three cell states investigated. Treatments were 0.5 iM LATA and 500units/mL hyaluronidase. Note the occurrence of peaks at integer multiples of the initial peak value.

multiple tethers are indeed being simultaneously extracted in an AFM experiment and that the effect of the contributions can be detected. It is important to compare the forces measured by AFM to what is presented in the literature and determine if the membrane vesicle tether force can be recovered.

Considering that elimination of both the cytoskeleton/membrane and glycocalyx/membrane associations would approximately create a membrane vesicle, it may be anticipated that subtraction of the contributions of these structures from the tether force recorded for untreated cells would result in the expected value for a pure phospholipid vesicle [180]. Using the approach of reference [180] the contributions of the cytoskeleton, F_{cyt} , glycocalyx, F_{glyc} , and the value for untreated cells, F_{nt} are considered:

$$F_{vesicle} = F_{nt} - F_{cyt} - F_{glyc} \quad (4.8)$$

Importantly, F_{cyt} and F_{glyc} are not the forces measured after LATA and hyaluronidase treatment respectively, they are the *difference* between F_{nt} and the forces measured after the respective treatments:

$$F_{cyt} = F_{nt} - F_{LATA}$$

$$F_{glyc} = F_{nt} - F_{hyaluronidase}$$

The values for F_{nt} , F_{cyt} and F_{glyc} are 29pN, 14pN and 8pN respectively. Using these values and equation 4.8, a value of 7pN is obtained for $F_{vesicle}$. This result is consistent with the value measured for a cell bleb in [180] further demonstrating that the AFM measurements have indeed measured the contributions of the cytoskeleton and glycocalyx and can be used to determine the degree to which multiple tether formation is influenced by these associations.

4.2.2 Summary: Overview of Tether Dynamics

At this point a brief summary of tether dynamics in AFM experiments is in order. Initial evidence for tether extraction by AFM was obtained through fluorescence visualization. Subsequent evidence was provided through analysis of the recorded force profiles. Ensemble histograms of measured force step values, ΔF , demonstrated that the force steps within profiles for each cell state have similar values suggesting that all plateaus have similar origins. Values for untreated endothelial cells and cells in which the cytoskeleton and glycocalyx were disrupted are respectively, 29pN, 15pN and 21pN. The primary origin of the force drops was determined by several means to be desorption from the cantilever. First, tether rupture was ruled out

since the forces recorded were between 10% and 30% of the membrane lysis force of 100pN and evidence of lipid remaining on the cantilever was inconclusive. Tether fusion was negated through comparison between the time required for a force step to occur at 6000nm/sec and the time required for a step to occur during a constant extension experiment (i.e. ~12.6nm/sec maximum). It was shown that in the constant extension experiment many steps occurred prior to 1sec instead of the 143sec minimum that was expected for tether fusion. Elimination of tether rupture and fusion left only desorption from the cantilever, and the need to determine its cause. Comparison of data acquired at 1000nm/sec to data acquired at 6000nm/sec and measurement of tether lengths considering the number of tethers attached to the cantilever at each plateau, led to the conclusion that desorption was triggered by depletion of the membrane reservoir. Measurement of the height of each plateau with respect to the $F = 0$ baseline resulted in histograms exhibiting multiple peaks separated by a single tether force. Peak width was shown to be indicative of asymmetries in pulling geometry influenced by the cytoskeleton and glycocalyx. Altogether, multiple tethers were extracted using AFM-based force spectroscopy, the origin of the force steps was determined and the effects of the cytoskeleton and

glycocalyx on the tether force were measured. These measurements suggest that any cellular process that affects membrane mechanics is detectable using this technique.

4.2.3 Tether Force Measurement: Application to Monitoring

Intracellular Processes

The endoplasmic reticulum (ER) is a large organelle surrounding the nucleus of a cell that performs several important functions, including the storage of calcium (Ca^{2+}). These ER calcium stores can be used by the cell to regulate the entry of external Ca^{2+} through a process termed store-mediated calcium entry (SMCE). The drug thapsigargin has been shown to activate SMCE in endothelial cells by blocking the ER associated Ca^{2+} -ATPase, causing release of the calcium stores [199]. The binding of thapsigargin to the Ca^{2+} -ATPase on the ER is the beginning of a signaling process that results in an influx of external Ca^{2+} . The details of this signaling process are not well understood, but are not important in the context of demonstrating that the influence of thapsigargin is detectable via AFM tether pulling experiments. It is enough to know that one result of the thapsigargin-induced signaling cascade is an increase in actin filament formation.

While an increase in internal calcium concentration ($[Ca^{2+}]_i$) can affect many cellular processes, it was shown in [199] that the cells contracted indicating increased actin polymerization. With the knowledge that the AFM can be used to measure changes in tether extraction force due to disruption of the cytoskeleton, it seems likely that a process known to strengthen the cytoskeleton could be detected with the same technique. Two methods were used to demonstrate the ability to detect this process: a time-course analysis and post-treatment tether extraction.

For the temporal analysis, endothelial cells were prepared as normal and the culture medium was exchanged for medium containing 10^{-6} M thapsigargin. The thapsigargin-containing medium was brought to 37°C prior to the exchange to reduce shock to the cells. Preparation of the experiment took between 5 and 6min, allowing the cells to equilibrate to 25°C . For each petri dish, data was acquired on several cells, as in previous sections, for 20 to 22min. The force curves were analyzed as in previous sections, but with the data separated into bins based on the time of acquisition. Each bin of data, corresponding to one minute of data acquisition, was averaged, and the results plotted versus time (Figure 4.18). The average force for untreated cells was

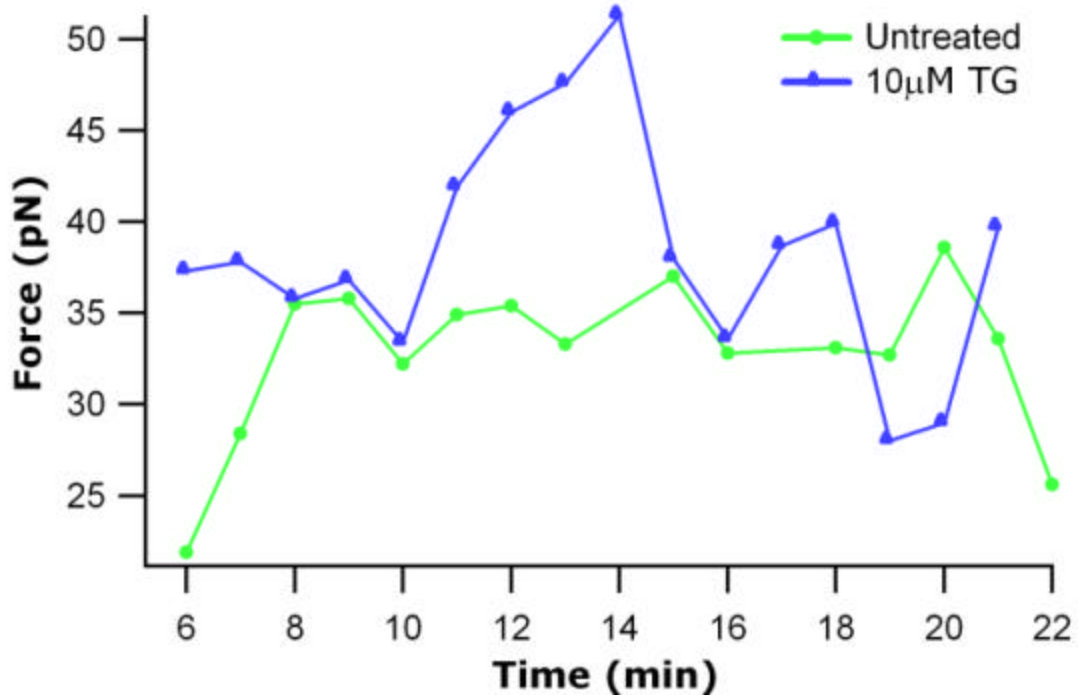


Figure 4.18. Average force versus time plot for treatment of endothelial cells with 10 μM thapsigargin at room temperature. Effect begins at 11min and lasts for 3min after which there is an abrupt drop back to the level of untreated cells.

consistent over the course of the experiment, fluctuating between 32 and 35pN (lower curve in figure 4.18). For cells treated with thapsigargin, the force begins increasing at about 11min reaching a peak at 14min after which there is a sharp drop back to the level of the untreated cells. Considering that this experiment was performed at room temperature, the behavior is consistent with published results measuring the time-course of $[Ca^{2+}]_i$ increase after thapsigargin treatment [210, 211]. This analysis uses average forces determined at each time point, so in order to compare these results with the tether

extraction experiments discussed in section 4.2.1, force histograms need to be analyzed.

Complete calcium store release has been reported for 200nM thapsigargin [212]. Therefore, endothelial cells were treated with 200nM thapsigargin at 37°C for 15min, after which tether pulling experiments were performed. A histogram of measured tether forces is presented in figure 4.19, and two distinct peaks are present at 20pN and 40pN. An immediate inclination is to assume that there are two populations of cells, one affected by thapsigargin and one not. The

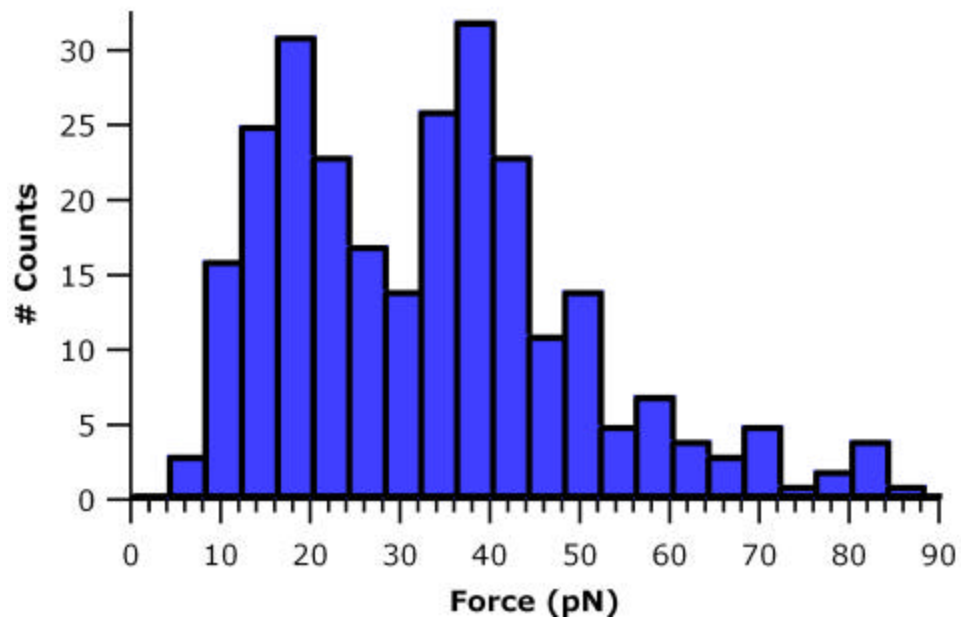


Figure 4.19. Histogram of tether forces measured at room temperature, after 15 min incubation in 200nM thapsigargin at 37 °C. Note the presence of two peaks at 20pN and 40pN.

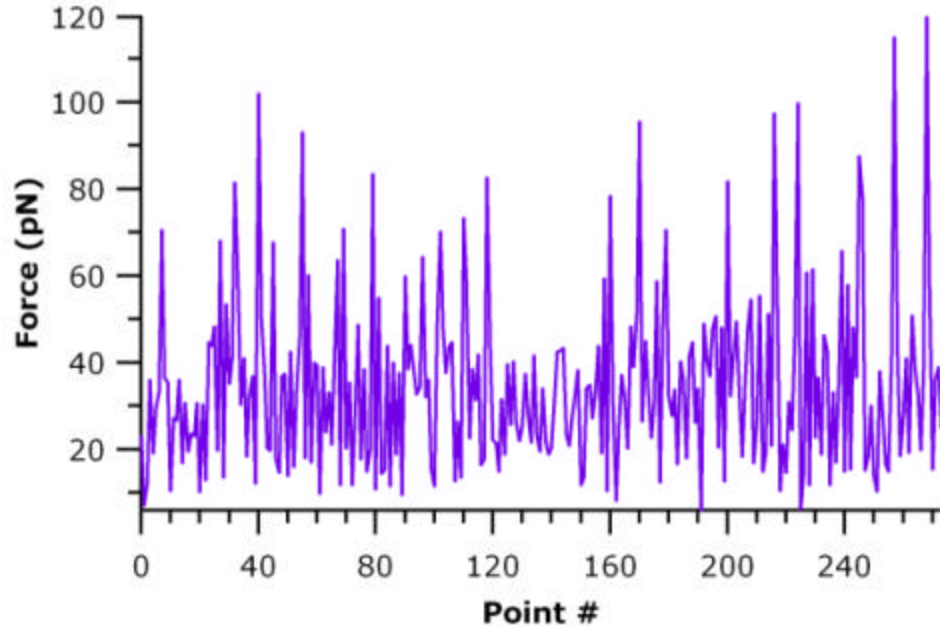


Figure 4.20. Plot of force versus point number to demonstrate that the two peaks in figure 4.19 are not the result of nonuniform treatment. The region between points 120 and 160 contains less than 40 data points and is possibly from a single cell. The number of points in this region is too small to account for the peak at 20 pN in figure 4.19.

force data used to produce the histogram of figure 4.19, arranged in order of acquisition, is plotted versus point number in figure 4.20. By arranging the data in the order it was acquired, it is also arranged sequentially by cell so that all data from the first cell is at the beginning, all data from the second cell immediately following, and so on. Since at least 20 data sets were acquired per cell, there will be more than 50 data points from each cell. Consequently, if two distinct populations of cells were being probed, the plot in figure 4.20 would exhibit large, discrete regions of low force separated by large, discrete regions of high force. With the exception of the data between points

120 and 160, such large discrete regions are not present indicating that there are not two distinct populations of cells. The low force data between points 120 and 160 may be from a single cell, but with less than 40 data points in this region, it cannot be responsible for the 20pN peak in figure 4.19. More interesting is the clear increase in mechanical heterogeneity of individual cell membranes evident from the spread of forces in figure 4.19 and the scatter of forces presented in figure 4.20. It is possible that the lower force peak is due to early stages of recovery after the peak effect of the treatment. It is

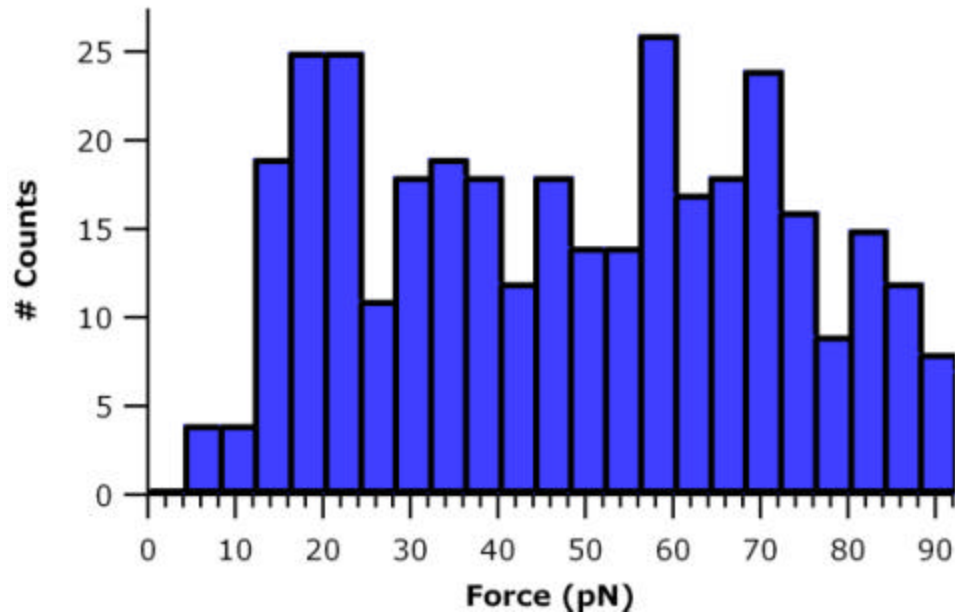


Figure 4.21. Histogram of tether forces recorded under ambient conditions after room temperature treatment with 200nM thapsigargin for 15min. Peaks at 18pN and 35pN are present as in the histogram of figure 4.19. The data occurring at higher forces is not surprising as the effect should be slowed by the ~10 °C reduction in temperature from the treatment at 37 °C.

interesting to note, however, that the higher force peak is double the force value of the lower force peak, and that the lower peak at 20pN is about 30% lower than forces measured on untreated cells. This result suggests that activation of the SMCE process causes a rearrangement of the cytoskeleton producing regions of the plasma membrane with reduced cytoskeletal association, while other regions experience an increase in cytoskeletal binding.

To slow the process and attempt to determine the origin of the dual peaks and compare the data of figure 4.19 with that presented in figure 4.18, the same experiment was performed at room temperature. The histogram for this experiment is presented in figure 4.21. Two peaks at 18pN and 35pN are visible as are a significant number of data points at higher forces. It is clear from this data that the dual peaks are not the result of recovery from treatment. Increased heterogeneities in cytoskeletal association with the membrane after thapsigargin treatment may indeed be responsible for the observed tether force separation [199]. The increase in stress fiber formation after treatment with thapsigargin is almost certainly the primary source of the forces above 40pN. Importantly, as mentioned above, many cellular processes are affected by $[Ca^{2+}]_i$ and these

processes cannot be discounted as possible sources for the peaks at 20 and 40pN.

The time course of the effect of thapsigargin as measured in AFM tether extraction experiments coincides with the time course in previous experiments in which either $[Ca^{2+}]_i$ or F-actin formation was monitored [210, 211]. Here, tether force began to increase at 10min lasting for 3min with a maximum average force of approximately 52pN. Following the peak was a sharp drop back to the force level of the untreated cells. Force histograms plotted for thapsigargin treatment at both 37°C and room temperature exhibit a peak at about 20pN and a second peak at approximately 40pN, double the force of the first peak. Additionally, the histogram for the room temperature experiment exhibits numerous points at forces higher than 40pN, a property absent from the 37°C experiment. It is likely that these higher forces are missing from the 37°C experiment due to recovery from the treatment. It is not clear why the dual peaks at 20 and 40pN are present. It is entirely possible that some other cellular process affected by $[Ca^{2+}]_i$ is responsible. Nevertheless, these experiments clearly demonstrate the ability to measure intracellular processes via multiple tether extraction with AFM. This method could conceivably

complement established techniques such as patch clamp providing a more robust interpretation of cellular processes affected by fluctuating ion concentrations.

REFERENCES

1. Binnig, G., C.F. Quate, and C. Gerber, "Atomic Force Microscope". *Physical Review Letters*, 1986. **56**(9): p. 930-933.
2. *Scanning Probe Microscopy Training Notebook*. 3.0 ed. 2000: Digital Instruments, Veeco Metrology Group. 56.
3. Meyer, G. and N.M. Amer, "Erattum: Novel optical approach to atomic force microscopy [Appl. Phys. Lett. 53, 1054 (1988)]". *Applied Physics Letters*, 1988. **53**(24): p. 2400-2402.
4. Albrecht, T.R., S. Akamine, T.E. Carver, and C.F. Quate, "Microfabrication of cantilever styli for the atomic force microscope". *Journal of Vacuum Science and Technology A*, 1990. **8**(4): p. 3386-3396.
5. Wolter, O., T. Bayer, and J. Greschner, "Micromachined silicon sensors for scanning force microscopy". *Journal of Vacuum Science and Technology B*, 1991. **9**(2): p. 1353-1357.
6. Meyer, E. and H. Heinzelmann, *Preparations of Cantilevers*, in *Scanning Tunneling Microscopy II*, H.-J. Geuntherodt, Editor. 1992, Springer-Verlag: Berlin/Heidelberg. p. 101-103,
7. Albrecht, T.R. and C.F. Quate, "Atomic resolution imaging of a nonconductor by atomic force microscopy". *Journal of Applied Physics*, 1987. **62**(7): p. 2599-2602.
8. Sader, J.E., "Susceptibility of atomic force microscope cantilevers to lateral forces". *Review of Scientific Instruments*, 2003. **74**(4): p. 2438-2443.

9. *Bio-Lever data sheet*. 2003, Olympus Optical Co., LTD.
10. Alexander, S., L. Hellemans, O. Marti, J. Schneir, V. Elings, P.K. Hansma, M. Longmire, and J. Gurley, "An atomic-resolution atomic-force microscope implemented using an optical lever". *Journal of Applied Physics*, 1989. **65**(1): p. 164-167.
11. Weisenhorn, A.L., P.K. Hansma, T.R. Albrecht, and C.F. Quate, "Forces in atomic force microscopy in air and water". *Applied Physics Letters*, 1989. **54**(26): p. 2651-2653.
12. Grandbois, M., H. Clausen-Schaumann, and H. Gaub, "Atomic Force Microscope Imaging of Phospholipid Bilayer Degradation by Phospholipase A₂". *Biophysical Journal*, 1998. **74**: p. 2398-2404.
13. Mueller, D.J. and A. Engel, "Voltage and pH-induced Channel Closure of Porin OmpF Visualized by Atomic Force Microscopy". *Journal of Molecular Biology*, 1999. **285**: p. 1347-1351.
14. Revenko, I., F. Sommer, D.T. Minh, R. Garrone, and J.-M. Franc, "Atomic force microscopy study of the collagen fibre structure". *Biology of the Cell*, 1994. **80**: p. 67-69.
15. Khurana, R., C. Ionescu-Zanetti, M. Pope, J. Li, L. Nielson, M. Ramirez-Alvarado, L. Regan, A.L. Fink, and S.A. Carter, "A General Model for Amyloid Fibril Assembly Based on Morphological Studies Using Atomic Force Microscopy". *Biophysical Journal*, 2003. **85**: p. 1135-1144.
16. Bustamante, C., J. Vesenka, C.L. Tang, W. Rees, M. Guthold, and R. Keller, "Circular DNA Molecules Imaged in Air by Scanning Force Microscopy". *Biochemistry*, 1992. **31**: p. 22-26.

17. Drygin, Y.F., O.A. Bordunova, M.O. Gallyamov, and I.V. Yaminsky, "Atomic force microscopy examination of tobacco mosaic virus and virion RNA". *FEBS Letters*, 1998. **425**: p. 217-221.
18. Florin, E.L., V.T. Moy, and H.E. Gaub, "Adhesion forces between individual ligand receptor pairs". *Science*, 1994. **264**: p. 415-417.
19. Hutter, J.L. and J. Bechhoefer, "Calibration of atomic-force microscope tips". *Reviews of Scientific Instruments*, 1993. **64**(7): p. 1868-1873.
20. Sader, J.E., "Frequency response of cantilever beams immersed in viscous fluids with applications to the atomic force microscope". *Journal of Applied Physics*, 1998. **84**(1): p. 64-76.
21. Proksch, R., T.E. Schäffer, J.P. Cleveland, R.C. Callahan, and M.B. Viani, "Finite optical spot size and position corrections in thermal spring constant calibration". *Nanotechnology*, 2004. **15**: p. 1344-1350.
22. Grandbois, M., W. Dettmann, M. Benoit, and H.E. Gaub, "Affinity Imaging of Red Blood Cells Using an Atomic Force Microscope". *The Journal of Histochemistry and Cytochemistry*, 2000. **48**(5): p. 719-724.
23. Li, F., S.D. Redick, H.P. Erickson, and V.T. Moy, "Force Measurements of the $\alpha_5\beta_1$ Integrin-Fibronectin Interaction". *Biophysical Journal*, 2003. **84**: p. 1252-1262.
24. Baumgartner, W., P. Hinterdorfer, W. Ness, A. Raab, D. Vestweber, H. Schindler, and D. Drenckhahn, "Cadherin interaction probed by atomic force microscopy". *Proceedings of*

the National Academy of Sciences of the United States of America, 2000. **97**(8): p. 4005-4010.

25. Dobrucki, J., *Applications of Confocal Microscopy*. 2003.
26. Alberts, B., A. Johnson, J. Lewis, M. Raff, K. Roberts, and P. Walter, *The Cytoskeleton*, in *Molecular Biology of the Cell*. 2002, Garland Science: New York. p. 907-927,
27. Fritz, M., M. Radmacher, J.P. Cleveland, M.W. Allersma, R.J. Stewart, R. Gieselmann, P. Janmey, C.F. Schmidt, and P.K. Hansma, "Imaging Globular and Filamentous Proteins in Physiological Buffer Solutions with Tapping Mode Atomic Force Microscopy". *Langmuir*, 1995. **11**: p. 3529-3535.
28. Palmer, A.F., P. Wingert, and J. Nickels, "Atomic Force Microscopy and Light Scattering of Small Unilamellar Actin-Containing Liposomes". *Biophysical Journal*, 2003. **85**: p. 1233-1247.
29. Kacher, C.M., I.M. Weiss, R.J. Stewart, C.F. Schmidt, P.K. Hansma, M. Radmacher, and M. Fritz, "Imaging microtubules and kinesin decorated microtubules using tapping mode atomic force microscopy in fluids". *European Biophysics Journal*, 2000. **28**: p. 611-620.
30. Alberts, B., A. Johnson, J. Lewis, M. Raff, K. Roberts, and P. Walter, *The Extracellular Matrix of Animals*, in *Molecular Biology of the Cell*. 2002, Garland Science: New York. p. 1090-1113,
31. Reichl, L.E., *Binomial Random Walk*, in *A Modern Course in Statistical Physics*. 1998, John Wiley & Sons: New York. p. 194-197,

32. Pathria, R.K., *The Statistics of Paramagnetism*, in *Statistical Mechanics*. 1972, Pergamon Press: Oxford. p. 79-81,
33. Goodstein, D.L., in *States of Matter*. 1985, Dover: New York. p. 419-421,
34. Kuhn, W. and F. Grun, *Kolloid Z*, 1942. **101**: p. 248.
35. Smith, S.B., L. Finzi, and C. Bustamante, "Direct Mechanical Measurements of the Elasticity of Single DNA Molecules by Using Magnetic Beads". *Science*, 1992. **258**: p. 1122-1126.
36. Smith, S.B., Y. Cui, and C. Bustamante, "Overstretching B-DNA: The Elastic Response of Individual Double-Stranded and Single-Stranded DNA Molecules". *Science*, 1996. **271**: p. 795-799.
37. Ortiz, C. and G. Hadziioannou, "Entropic Elasticity of Single Polymer Chains of Poly(methacrylic acid) Measured by Atomic Force Microscopy". *Macromolecules*, 1999. **32**: p. 780-787.
38. Doi, M. and S. Edwards, *The Theory of Polymer Dynamics*. International Series of Monographs on Physics, ed. J. Birman, et al. Vol. 73. 1986, Oxford: Clarendon Press.
39. Kratky, O. and G. Porod, "Rontgenuntersuchung geloster fadenmolekule". *Recl. Trav. Chim.*, 1949. **68**: p. 1106-1122.
40. Grosberg, A.Y. and A.R. Khokhlov, *Statistical Physics of Macromolecules*. AIP Series in Polymers and Complex Materials, ed. R. Larson and P.A. Pincus. Vol. 1. 1994, New York: AIP Press.

41. Flory, P.J., *Statistical Mechanics of Chain Molecules*. 1989, Cincinnati: Hanser.
42. Fixman, M. and J. Kovac, "Polymer conformational statistics. III. Modified Gaussian models of stiff chains". *The Journal of Chemical Physics*, 1973. **58**(4): p. 1564-1568.
43. Kovac, J. and C.C. Crabb, "Modified Gaussian Model for Rubber Elasticity. 2. The Wormlike Chain". *Macromolecules*, 1982. **15**: p. 537-541.
44. Bustamante, C., J.F. Marko, and S. Smith, "Entropic Elasticity of λ -Phage DNA". *Science*, 1994. **265**: p. 1599-1600.
45. Marko, J.F. and E.D. Siggia, "Stretching DNA". *Macromolecules*, 1995. **28**: p. 8759-8770.
46. Odijk, T., "Stiff Chains and Filaments under Tension". *Macromolecules*, 1995. **28**: p. 7016-7018.
47. Fujii, T., Y.-L. Sun, K.-N. An, and Z.-P. Luo, "Mechanical properties of single hyaluronan molecules". *Journal of Biomechanics*, 2002. **35**: p. 527-531.
48. de Gennes, P.G., "Conformations of Polymers Attached to an Interface". *Macromolecules*, 1980. **13**: p. 1069-1075.
49. Rief, M., F. Oesterhelt, B. Heymann, and H.E. Gaub, "Single Molecule Force Spectroscopy on Polysaccharides by Atomic Force Microscopy". *Science*, 1997. **275**: p. 1295-1297.

50. Marszalek, P.E., H. Li, and J.M. Fernandez, "Fingerprinting polysaccharides with single-molecule atomic force microscopy". *Nature Biotechnology*, 2001. **19**: p. 258-262.
51. Lee, G.U., D.A. Kidwell, and R.J. Colton, "Sensing Discrete Streptavidin-Biotin Interactions with Atomic Force Microscopy". *Langmuir*, 1994. **10**: p. 354-357.
52. Marszalek, P.E., A.F. Oberhauser, Y.-P. Pang, and J.M. Fernandez, "Polysaccharide Elasticity Governed by Chair-boat Transitions of the Glucopyranose Ring". *Nature*, 1998. **396**: p. 661-664.
53. Xu, Q., W. Zhang, and X. Zhang, "Oxygen Bridge Inhibits Conformational Transition of 1,4-Linked α -D-Galactose Detected by Single-Molecule Atomic Force Microscopy". *Macromolecules*, 2002. **35**: p. 871-876.
54. Li, H., M. Rief, F. Oesterhelt, H.E. Gaub, X. Zhang, and J. Shen, "Single-molecule force spectroscopy on polysaccharides by AFM - nanomechanical fingerprint of α -(1,4)-linked polysaccharides". *Chemical Physics Letters*, 1999. **305**: p. 197-201.
55. Marszalek, P.E., Y.-P. Pang, H. Li, J.E. Yazal, A.F. Oberhauser, and J.M. Fernandez, "Atomic levers control pyranose ring conformations". *Proceedings of the National Academy of Sciences*, 1999. **96**: p. 7894-7898.
56. Henry, C.B.S. and B.R. Duling, "Permeation of the luminal capillary glycocalyx is determined by hyaluronan". *American Journal of Physiology*, 1999. **277**: p. H508-H514.
57. Vogel, K.G., "Effects of hyaluronidase, trypsin, and EDTA on surface composition and topography during detachment of cells in culture". *Experimental Cell Research*, 1978. **113**: p. 345-357.

58. Yang, B.B., Y. Zhang, and L. Cao, "Aggrecan and Link Protein Affect Cell Adhesion to Culture Plates and to Type II Collagen". *Matrix Biology*, 1998. **16**: p. 541-561.
59. Delpech, B., M.-N. Courel, C. Maingonnat, C. Chauzy, R. Sesboué, and G. Pratesi, "Hyaluronan digestion and synthesis in an experimental model of metastatic tumour". *The Histochemical Journal*, 2001. **33**: p. 553-558.
60. Goebeler, M., D. Kaufmann, E.-B. Bröcker, and C.E. Klein, "Migration of highly aggressive melanoma cells on hyaluronic acid is associated with functional changes, increased turnover and shedding of CD44 receptors". *Journal of Cell Science*, 1996. **109**: p. 1957-1964.
61. Lüke, H.-J. and P. Prehm, "Synthesis and shedding of hyaluronan from plasma membranes of human fibroblasts and metastatic and non-metastatic melanoma cells". *Biochemical Journal*, 1999. **343**: p. 71-75.
62. *DNA Structure*, in *Molecular Biology Web Book*<http://www.web-books.com/MoBio/Free/Ch3B3.htm>.
63. Howard, J., *Mechanics of Motor Proteins and the Cytoskeleton*. 2001, MA: Sinauer Associates, Inc.
64. Bensimon, A., A. Simon, A. Chiffaudel, V. Croquette, F. Heslot, and D. Bensimon, "Alignment and Sensitive Detection of DNA by a Moving Interface". *Science*, 1994. **265**: p. 2096-2098.
65. Clausen-Schaumann, H., M. Rief, C. Tolksdorf, and H.E. Gaub, "Mechanical Stability of Single DNA Molecules". *Biophysical Journal*, 2000. **78**: p. 1997-2007.

66. Cluzel, P., A. Lebrun, C. Heller, R. Lavery, J.-L. Viovy, D. Chatenay, and F. Caron, "DNA: An Extensible Molecule". *Science*, 1996. **271**: p. 792-794.
67. Harnau, L. and P. Reineker, "Relaxation dynamics of partially extended single DNA molecules". *New Journal of Physics*, 1999. **1**(3): p. 3.1-3.6.
68. Rief, M., H. Clausen-Schaumann, and H.E. Gaub, "Sequence-dependent mechanics of single DNA molecules". *Nature Structural Biology*, 1999. **6**(4): p. 346-349.
69. Strunz, T., K. Oroszlan, R. Schäfer, and H.-J. Gütherodt, "Dynamic force spectroscopy of single DNA molecules". *Proceedings of the National Academy of Sciences*, 1999. **96**: p. 11277-11282.
70. Gerland, U., R. Bundschuh, and T. Hwa, "Force-Induced Denaturation of RNA". *Biophysical Journal*, 2001. **81**: p. 1324-1332.
71. Liphardt, J., B. Onoa, S.B. Smith, I.T. Jr., and C. Bustamante, "Reversible Unfolding of Single RNA Molecules by Mechanical Force". *Science*, 2001. **292**: p. 733-737.
72. Cai, X.-E. and J. Yang, "Molecular Forces for the Binding and Condensation of DNA Molecules". *Biophysical Journal*, 2002. **82**: p. 357-365.
73. Maier, B., D. Bensimon, and V. Croquette, "Replication by a single DNA polymerase of a stretched single-stranded DNA". *Proceedings of the National Academy of Sciences*, 2000. **97**(22): p. 12002-12007.

74. Onoa, B., S. Dumont, J. Liphardt, S.B. Smith, I.T. Jr., and C. Bustamante, "Identifying Kinetic Barriers to Mechanical Unfolding of the *T. thermophila* Ribozyme". *Science*, 2003. **299**: p. 1892-1895.
75. Sarkar, A. and J.F. Marko, "Removal of DNA-bound proteins by DNA twisting". *Physical Review E*, 2001. **64**(6): p. 061909-1-061909-10.
76. Mao, C., W. Sun, Z. Shen, and N.C. Seeman, "A nanomechanical device based on the B-Z transition of DNA". *Nature*, 1999. **397**: p. 144-146.
77. Albrecht, C., K. Blank, M. Lalic-Mülthaler, S. Hirler, T. Mai, I. Gilbert, S. Schiffmann, T. Bayer, H. Clausen-Shaumann, and H.E. Gaub, "DNA: A Programmable Force Sensor". *Science*, 2003. **301**: p. 367-370.
78. *Protein Structure and Function - α -helix*, in *Molecular Biology Web Book*<http://www.web-books.com/MoBio/Free/Ch2C4.htm>.
79. *Protein Structure and Function - Beta Sheet*, in *Molecular Biology Web Book*<http://www.web-books.com/MoBio/Free/Ch2C6.htm>.
80. Kellermayer, M.S., S.B. Smith, H.L. Granzier, and C. Bustamante, "Folding-Unfolding Transitions in Single Titin Molecules Characterized with Laser Tweezers". *Science*, 1997. **276**: p. 1112-1116.
81. Oberhauser, A.F., P.E. Marszalek, H.P. Erickson, and J.M. Fernandez, "The molecular elasticity of the extracellular matrix protein tenascin". *Nature*, 1998. **393**: p. 181-185.

82. Rief, M., M. Gautel, F. Oesterhelt, J.M. Fernandez, and H.E. Gaub, "Reversible Unfolding of Individual Titin Immunoglobulin Domains by AFM". *Science*, 1997. **276**: p. 1109-1112.
83. Li, H., A.F. Oberhauser, S.B. Fowler, J. Clarke, and J.M. Fernandez, "Atomic force microscopy reveals the mechanical design of a modular protein". *Proceedings of the National Academy of Sciences*, 2000. **97**(12): p. 6527-6531.
84. Rief, M., J. Pascual, M. Saraste, and H.E. Gaub, "Single Molecule Force Spectroscopy of Spectrin Repeats: Low Unfolding Forces in Helix Bundles". *Journal of Molecular Biology*, 1999. **286**: p. 553-561.
85. Thie, M., R. Röspe, W. Dettmann, M. Benoit, M. Ludwig, H.E. Gaub, and H.-W. Denker, "Interactions between trophoblast and uterine epithelium: monitoring of adhesive forces". *Human Reproduction*, 1998. **13**(11): p. 3211-3219.
86. Benoit, M. and H.E. Gaub, "Measuring Cell Adhesion Forces with the Atomic Force Microscope at the Molecular Level". *Cells Tissues Organs*, 2002. **172**: p. 174-189.
87. Adelman, K., A.L. Porta, T.J. Santangelo, J.T. Lis, J.W. Roberts, and M.D. Wang, "Single molecule analysis of RNA polymerase elongation reveals uniform kinetic behavior". *Proceedings of the National Academy of Sciences*, 2002. **99**(21): p. 13538-13543.
88. Fisher, T.E., M. Carrion-Vazquez, A.F. Oberhauser, H. Li, P.E. Marszalek, and J.M. Fernandez, "Single Molecule Force Spectroscopy of Modular Proteins in the Nervous System". *Neuron*, 2000. **27**: p. 435-446.

89. Bustamante, C., S.B. Smith, J. Liphardt, and D. Smith, "Single-molecule studies of DNA mechanics". *Current Opinion in Structural Biology*, 2000. **10**: p. 279-285.
90. Alberts, B., A. Johnson, J. Lewis, M. Raff, K. Roberts, and P. Walter, *Collagens are the Major Proteins of the Extracellular Matrix*, in *Molecular Biology of the Cell*. 2002, Garland Science: New York. p. 1096,
91. Kadler, K.E., Y. Hojima, and D.J. Prockop, "Assembly of collagen fibrils de novo by cleavage of the type I pC- collagen with procollagen C-proteinase. Assay of critical concentration demonstrates that collagen self-assembly is a classical example of an entropy-driven process". *The Journal of Biological Chemistry*, 1987. **262**: p. 15696-15701.
92. Breen, E.C., "Mechanical strain increases type I collagen expression in pulmonary fibroblasts in vitro". *Journal of Applied Physiology*, 2000. **88**: p. 203-209.
93. Sasaki, N. and S. Odajima, "Stress-Strain Curve and Young's Modulus of a Collagen Molecule as Determined by the X-ray Diffraction Technique". *Journal of Biomechanics*, 1996. **29**(5): p. 655-658.
94. Sasaki, N. and S. Odajima, "Elongation Mechanism of Collagen Fibrils and Force-Strain Relations of Tendon at Each Level of Structural Hierarchy". *Journal of Biomechanics*, 1996. **29**(9): p. 1131-1136.
95. Alberts, B., A. Johnson, J. Lewis, M. Raff, K. Roberts, and P. Walter, *After Secretion, Fibrillar Procollagen Molecules Are Cleaved to Collagen Molecules, Which Assemble into Fibrils*, in *Molecular Biology of the Cell*. 2002, Garland Science: New York. p. 1099,

96. Alberts, B., A. Johnson, J. Lewis, M. Raff, K. Roberts, and P. Walter, *Elastin Gives Tissues Their Elasticity*, in *Molecular Biology of the Cell*. 2002, Garland Science: New York. p. 1102-1103,
97. Vouyouka, A.G., B.J. Pfeiffer, T.A. Taylor, T.K. Liem, J. Mudaliar, and C.L. Phillips, "The Role of Type I Collagen in Aortic Wall Strength using a Homotrimeric $[\alpha 1(I)]_3$ Collagen Mouse Model". *Journal of Vascular Surgery*, 2001. **33**: p. 1263-1270.
98. *Biochemistry and Biomechanics*. Collagen, ed. M.E. Nimni. Vol. 2. 1988, Boca Raton: CRC Press. 297.
99. *Biochemistry*. Collagen, ed. M.E. Nimni. Vol. 1. 1988, Boca Raton: CRC Press. 299.
100. Christiansen, D.L., E.K. Huang, and F.H. Silver, "Assembly of type I collagen: fusion of fibril subunits and the influence of fibril diameter on mechanical properties". *Matrix Biology*, 2000. **19**: p. 409-420.
101. Baldock, C., C.J. Gilpin, A.J. Koster, U. Ziese, K.E. Kadler, C.M. Kielty, and D.F. Holmes, "Three-dimensional reconstructions of extracellular matrix polymers using automated electron tomography". *Journal of Structural Biology*, 2002. **138**(1-2): p. 130-136.
102. Holmes, D.F., C.J. Gilpin, C. Baldock, U. Ziese, A.J. Koster, and K.E. Kadler, "Corneal collagen fibril structure in three dimensions: Structural insights into fibril assembly, mechanical properties, and tissue organization". *Proceedings of the National Academies of Science*, 2001. **98**(13): p. 7307-7312.
103. Siegel, R.C., "Lysyl Oxidase". *International Review of Connective Tissue Research*, 1979. **8**: p. 73-118.

104. Kadler, K.E., D.F. Holmes, J.A. Trotter, and J.A. Chapman, "Collagen Fibril Formation". *Biochemical Journal*, 1996. **316**(1): p. 1-11.
105. Mertz, E.L. and S. Leikin, "Interactions of Inorganic Phosphate and Sulfate Anions with Collagen". *Biochemistry*, 2004. **43**: p. 14901-14912.
106. Galbraith, C.G. and M.P. Sheetz, "A Micromachined Device Provides a New Bend on Fibroblast Traction Forces". *Proceedings of the National Academies of Science*, 1997. **94**: p. 9114-9118.
107. Lee, G.M. and R.F. Loeser, "Cell Surface Receptors Transmit Sufficient Force to Bend Collagen Fibrils". *Experimental Cell Research*, 1999. **248**: p. 294-305.
108. Leikin, S., D.C. Rau, and V.A. Parsegian, "Temperature-favoured assembly of collagen is driven by hydrophilic not hydrophobic interactions". *Nature Structural Biology*, 1995. **2**: p. 205-210.
109. Wess, T.J., L. Hammersley, L. Wess, and A. Miller, "Molecular Packing of Type I Collagen in Tendon". *Journal of Molecular Biology*, 1998. **275**: p. 255-267.
110. Ottani, V., D. Martini, M. Franchi, A. Ruggeri, and M. Raspanti, "Hierarchical structures in fibrillar collagens". *Micron*, 2002. **33**: p. 587-596.
111. Gerstenfeld, L.C., A. Riva, K. Hodgens, D.R. Eyre, and W.J. Landis, "Post-translational control of collagen fibrillogenesis in mineralizing cultures of chick osteoblasts". *Journal of Bone and Mineral Research*, 1993. **8**(9): p. 1031-1043.

112. Howard, E.W., R. Benton, J. Ahern-Moore, and J.J. Tomasek, "Cellular Contraction of Collagen Lattices Is Inhibited by Nonenzymatic Glycation". *Experimental Cell Research*, 1996. **228**: p. 132-137.
113. Ulrich, P. and A. Cerami, "Protein Glycation, Diabetes, and Aging". *Recent Progress in Hormone Research*, 2001. **56**(1): p. 1-21.
114. Stulz, C.M. and E.R. Edelman, "A Structural Model that Explains the Effects of Hyperglycemia on Collagenolysis". *Biophysical Journal*, 2003. **85**: p. 2198-2204.
115. Kagan, H.M. and P.C. Trackman, "Properties and Function of Lysyl Oxidase". *American Journal of Respiratory Cell and Molecular Biology*, 1991. **5**: p. 206-210.
116. Goh, M.C. and A.C. Lin, "Collagen Fibrillar Constructs: New Ideas on their Formation and Ultrastructure via a Parallel AFM, TEM, ESI and NMR approach". *Biophysical Journal*, 2002. **82**(1): p. 503.
117. Gale, M., M.S. Pollanen, P. Markiewicz, and M.C. Goh, "Sequential Assembly of Collagen Revealed by Atomic Force Microscopy". *Biophysical Journal*, 1995. **68**(5): p. 2124-2128.
118. Brown, R.E., J.P. Butler, R.A. Rogers, and D.E. Leith, "Mechanical Connections Between Elastin and Collagen". *Connective Tissue Research*, 1994. **30**: p. 295-308.
119. Eschenhagen, T., F. Christine, U. Remmers, H. Scholz, J. Wattchow, J. Weil, W. Zimmerman, H. Dohmen, H. Schaefer, N. Bishopric, T. Wakatsuki, and E.L. Elson, "Three-dimensional reconstruction of embryonic cardiomyocytes in a collagen

matrix: a new heart muscle model system". *The FASEB Journal*, 1997. **11**: p. 683-694.

120. Harris, A.K., D. Stopak, and P. Wild, "Fibroblast traction as a mechanism for collagen morphogenesis". *Nature*, 1981. **290**: p. 249-251.
121. Harris, A.K., *Multicellular mechanics in the creation of anatomical structures*, in *Biomechanics of Active Movements and Division of Cells*, N. Akkas, Editor. 1994, Springer: Berlin. p. 87-129,
122. Hay, E.D., "Interaction of migrating embryonic cells with extracellular matrix". *Experimental Biology and Medicine*, 1985. **10**: p. 174-193.
123. Hay, E.D., "Extracellular matrix, cell skeletons and embryonic development". *American Journal of Medical Genetics*, 1989. **34**: p. 14-29.
124. Jester, J.V., W.M. Petroll, P.A. Barry, and H.D. Cavanagh, "Temporal, three-dimensional, cellular anatomy of corneal wound tissue". *Journal of Anatomy*, 1995. **186**: p. 301-311.
125. Yannas, I.V., E. Lee, D.P. Orgill, E.M. Skrabut, and G.F. Murphy, "Synthesis and characterization of a model extracellular matrix that induces partial regeneration of adult mammalian skin". *Proceedings of the National Academies of Science*, 1989. **86**: p. 933-937.
126. Friedl, P. and E.-B. Broecker, "The biology of cell locomotion within three-dimensional extracellular matrix". *Cellular and Molecular Life Sciences*, 2000. **57**: p. 41-64.

127. Freyman, T.M., Yannas, I. V., Pek, Y-S, Yokoo, R., and Gibson, L. J., "Micromechanics of Fibroblast Contraction of a Collagen-GAG Matrix". *Experimental Cell Research*, 2001. **269**: p. 140-153.
128. Lauffenburger, D.A. and A.F. Horwitz, "Cell migration: A physically integrated molecular process". *Cell*, 1996. **84**: p. 359-369.
129. Roy, P., W.M. Petroll, H.D. Cavanagh, C.J. Chuong, and J.V. Jester, "An *in vitro* force measurement assay to study the early mechanical interaction between corneal fibroblasts and collagen matrix". *Experimental Cell Research*, 1997. **232**: p. 106-117.
130. Freyman, T.M., I.V. Yannas, R. Yokoo, and L.J. Gibson, "Fibroblast Contractile Force is Independent of the Stiffness Which Resists the Contraction". *Experimental Cell Research*, 2002. **272**: p. 153-162.
131. Phillips, C.L., D.A. Bradley, C.L. Schlotzhauer, M. Bergfeld, C. Libreros-Minotta, L.R. Gawenis, J.S. Morris, L.L. Clarke, and L.S. Hillman, "*Oim* Mice exhibit Altered Femur and Incisor Mineral Composition and Decreased Bone Mineral Density". *Bone*, 2000. **27**: p. 219-226.
132. Kastelic, J., I. Palley, and E. Baer, "A Structural Mechanical Model for Tendon Crimping". *Biomechanics*, 1979. **13**: p. 887-893.
133. Graham, J.S., A.N. Vomund, C.L. Phillips, and M. Grandbois, "Structural changes in human type I collagen fibrils investigated by force spectroscopy". *Experimental Cell Research*, 2004. **299**: p. 335-342.

134. Taatjes, D.J., A.S. Quinn, and E.G. Bovill, "Imaging of Collagen Type III in Fluid by Atomic Force Microscopy". *Microscopy Research and Technique*, 1999. **44**(5): p. 347-352.
135. Paige, M.F., J.K. Rainey, and M.C. Goh, "Fibrous Long Spacing Collagen Ultrastructure Elucidated by Atomic Force Microscopy". *Biophysical Journal*, 1998. **74**(6): p. 3211-3216.
136. Rief, M., M. Gautel, A. Schemmel, and H.E. Gaub, "The Mechanical Stability of Immunoglobulin and Fibronectin III Domains in the Muscle Protein Titin Measured by Atomic Force Microscopy". *Biophysical Journal*, 1998. **75**: p. 3008-3014.
137. Seitz, M., C. Friedsam, W. Jöstl, T. Hugel, and H.E. Gaub, "Probing Solid Surfaces with Single Polymers". *ChemPhysChem*, 2003. **4**: p. 986-990.
138. Friedsam, C., A.D.C. Bécares, U. Jonas, M. Seitz, and H.E. Gaub, "Adsorption of polyacrylic acid on self-assembled monolayers investigated by single-molecule force spectroscopy". *New Journal of Physics*, 2004. **6**: p. 1-16.
139. Hugel, T., M. Grosholz, H. Clausen-Schaumann, A. Pfau, H.E. Gaub, and M. Seitz, "Elasticity of Single Polyelectrolyte Chains and Their Desorption from Solid Supports Studied by AFM Based Single Molecule Force Spectroscopy". *Macromolecules*, 2001. **34**: p. 1039-1047.
140. Idiris, A., M.T. Alam, and A. Ikai, "Spring mechanics of α -helical polypeptide". *Protein Engineering*, 2000. **13**(11): p. 763-770.
141. Miles, C.A. and A.J. Bailey, "Thermally labile domains in the collagen molecule". *Micron*, 2001. **32**: p. 325-332.

142. Lantz, M.A., S.P. Jarvis, H. Tokumoto, T. Martynski, T. Kusumi, C. Nakamura, and J. Miyake, "Stretching the α -helix: a direct measure of the hydrogen-bond energy of a single-peptide molecule". *Chemical Physics Letters*, 1999. **315**: p. 61-68.
143. Grandbois, M., M. Beyer, M. Rief, H. Clausen-Schaumann, and H.E. Gaub, "How Strong is a Covalent Bond?" *Science*, 1999. **283**: p. 1727-1730.
144. Pfeiffer, B.J., C.L. Franklin, F.-h. Hsieh, R.A. Bank, and C.L. Phillips, "Alpha 2(I) collagen deficient *oim* mice have altered biomechanical integrity, collagen content, and collagen crosslinking of their thoracic aorta". *Matrix Biology*, 2005. **In Press**.
145. Chipman, S.D., H.O. Sweet, D.J. McBride Jr., M.T. Davisson, S.C. Marks Jr., A.R. Shuldiner, R.J. Wenstrup, D.W. Rowe, and J.R. Shapiro, "Defective pro α 2(I) collagen synthesis in a recessive mutation in mice: A model of human osteogenesis imperfecta". *Proceedings of the National Academies of Science*, 1993. **90**: p. 1701-1705.
146. Williams, B.R., R.A. Gelman, D.C. Poppke, and K.A. Piez, "Collagen fibril formation. Optimal in vitro conditions and preliminary kinetic results." *Journal of Biological Chemistry*, 1978. **253**(18): p. 6578-6585.
147. Birchall, I.E., V.W.K. Lee, and V. Ketharanathan, "Retention of endothelium on ovine collagen biomatrix vascular conduits under physiological shear stress". *Biomaterials*, 2001. **22**: p. 3139-3144.
148. Courey, M.S., "Homologous Collagen Substances for Vocal Fold Augmentation". *The Laryngoscope*, 2001. **111**: p. 747-758.

149. Keilhoff, G., F. Stang, G. Wolf, and H. Fansa, "Bio-compatibility of type I/III collagen matrix for peripheral nerve reconstruction". *Biomaterials*, 2003. **24**: p. 2779-2787.
150. Storhoff, J.J., A.A. Lazarides, R.C. Mucic, C.A. Mirkin, R.J. Letsinger, and G.C. Schatz, "What Controls the Optical Properties of DNA-Linked Gold Nanoparticle Assemblies". *Journal of the American Chemical Society*, 2000. **122**: p. 4640-4650.
151. Mao, C., W. Sun, and N.C. Seeman, "Designed Two-Dimensional DNA Holliday Junction Arrays Visualized by Atomic Force Microscopy". *Journal of the American Chemical Society*, 1999. **121**: p. 5437-5443.
152. Yan, H., S.H. Park, G. Finkelstein, J.H. Reif, and T. LaBean, "DNA-Templated Self-Assembly of Protein Arrays and Highly Conductive Nanowires". *Science*, 2003. **301**: p. 1882-1884.
153. Huynh, T., G. Abraham, J. Murray, K. Brockbank, P.-O. Hagen, and S. Sullivan, "Remodeling of an acellular collagen graft into a physiologically responsive neovessel". *Nature Biotechnology*, 1999. **17**: p. 1083-1086.
154. Ma, L., C. Gao, Z. Mao, J. Zhou, J. Shen, X. Hu, and C. Han, "Collagen/chitosan porous scaffolds with improved biostability for skin tissue engineering". *Biomaterials*, 2003. **24**: p. 4833-4841.
155. Kikuchi, M., H.N. Matsumoto, T. Yamada, Y. Koyama, K. Takakuda, and J. Tanaka, "Glutaraldehyde cross-linked hydroxyapatite/collagen self-organized nanocomposites". *Biomaterials*, 2004. **25**: p. 63-69.
156. Raghuraman, K., K.K. Katti, L.J. Barbour, N. Pillarsetty, C.L. Barnes, and K.V. Katti, "Characterization of Supramolecular (H₂O)₁₈ Water Morphology and Water-Methanol (H₂O)₁₅(CH₃OH)₃

Clusters in a Novel Phosphorous Functionalized Trimeric Amino Acid Host". *Journal of the American Chemical Society*, 2003. **125**: p. 6955-6961.

157. Moores, A., F. Goettmann, C. Sanchez, and P. Le Floch, "Phosphine stabilised gold nanoparticles; synthesis and Immobilisation on mesoporous materials". *Chemical Communications*, 2004(24): p. 2842-2843.
158. Weare, W.W., S.M. Reed, M.G. Warner, and J.E. Hutchison, "Improved Synthesis of Small ($d_{core} \sim 1.5$ nm) Phosphine-Stabilized Gold Nanoparticles". *Journal of the American Chemical Society*, 2000. **122**: p. 12890-12891.
159. Wong, G.C.L., A. Lin, J.X. Tang, Y. Li, P.A. Janmey, and C.R. Safinya, "Lamellar Phase of Stacked Two-Dimensional Rafts of Actin Filaments". *Physical Review Letters*, 2003. **91**: p. 018103.
160. Zhao, H., B. Yuan, and X. Dou, "The effects of electrostatic interaction between biological molecules and nano-metal colloid on near-infrared surface-enhanced Raman scattering". *Journal of Optics A: Pure and Applied Optics*, 2004. **6**: p. 900-905.
161. Nakao, H., H. Shiigi, Y. Yamamoto, S. Tokonami, T. Nagaoka, S. Sugiyama, and T. Ohanti, "Highly Ordered Assemblies of Au Nanoparticles Organized on DNA". *Nano Letters*, 2003. **3**(10): p. 1391-1394.
162. Deng, Z. and C. Mao, "DNA-Templated Fabrication of 1D Parallel and 2D Crossed Metallic Nanowire Arrays". *Nano Letters*, 2003. **3**(11): p. 1545-1548.
163. Freyman, T.M., I.V. Yannas, R. Yokoo, and L.J. Gibson, "Fibroblast contraction of a collagen-GAG matrix". *Biomaterials*, 2001. **22**: p. 2883-2891.

164. Takeichi, M., "Morphogenetic roles of classic cadherins". *Current Opinion in Cell Biology*, 1995. **7**(5): p. 619-627.
165. Sheetz, M.P., "Cellular Plasma Membrane Domains". *Molecular Membrane Biology*, 1995. **12**(1): p. 89-91.
166. Schmidtke, D.W. and S.L. Diamond, "Direct Observation of Membrane Tethers Formed during Neutrophil Attachment to Platelets or P-selectin under Physiological Flow". *Journal of Cell Biology*, 2000. **149**(3): p. 719-730.
167. Iglic, A., H. Hägerstrand, M. Bobrowska-Hägerstrand, V. Arrigler, and V. Kralj-Iglic, "Possible role of phospholipid nanotubes in directed transport of membrane vesicles". *Physics Letters A*, 2003. **310**(5-6): p. 493-497.
168. Rustom, A., R. Saffrich, I. Markovic, P. Walther, and H.-H. Gerdes, "Nanotubular Highways for Intercellular Organelle Transport". *Science*, 2004. **303**: p. 1007-1010.
169. Upadhyaya, A. and M.P. Sheetz, "Tension in Tubulovesicular Networks of Golgi and Endoplasmic Reticulum Membranes". *Biophysical Journal*, 2004. **86**: p. 2923-2928.
170. Giuffrè, L., A.-S. Cordy, N. Monai, Y. Tardy, M. Schapira, and O. Spertini, "Monocyte Adhesion to Activated Aortic Endothelium: Role of L-Selectin and Heparan Sulfate Proteoglycans". *The Journal of Cell Biology*, 1997. **136**(4): p. 945-956.
171. Sanders, W.J., E.J. Gordon, O. Dwir, P.J. Beck, R. Alon, and L.L. Kiessling, "Inhibition of L-selectin-mediated Leukocyte Rolling by Synthetic Glycoprotein Mimics". *The Journal of Biological Chemistry*, 1999. **274**(9): p. 5271-5278.

172. DeGrendele, H.C., P. Estess, L.J. Picker, and M.H. Siegelman, "CD44 and its Ligand Hyaluronate Mediate Rolling under Physiologic Flow: A Novel Lymphocyte-Endothelial Cell Primary Adhesion Pathway". *The Journal of Experimental Medicine*, 1996. **183**(3): p. 1119-1130.
173. Chen, S. and T.A. Springer, "An Automatic Braking System That Stabilizes Leukocyte Rolling by an Increase in Selectin Bond Number with Shear". *The Journal of Cell Biology*, 1999. **144**(1): p. 185-200.
174. Evans, E.A. and R.M. Hochmuth, "Membrane viscoelasticity". *Biophysical Journal*, 1976. **16**: p. 1-12.
175. Evans, E.A. and R.M. Hochmuth, "Membrane viscoplastic flow". *Biophysical Journal*, 1976. **16**: p. 13-26.
176. Zhelev, D.V. and R.M. Hochmuth, "Mechanically stimulated cytoskeleton rearrangement and cortical contraction". *Biophysical Journal*, 1995. **68**: p. 2004-2014.
177. Dai, J., M.P. Sheetz, X. Wan, and C.E. Morris, "Membrane Tension in Swelling and Shrinking Molluscan Neurons". *The Journal of Neuroscience*, 1998. **18**(17): p. 6681-6692.
178. Raucher, D. and M.P. Sheetz, "Characteristics of a Membrane Reservoir Buffering Membrane Tension". *Biophysical Journal*, 1999. **77**(4): p. 1992-2000.
179. Raucher, D. and M.P. Sheetz, "Phospholipase C activation by anesthetics decreases membrane-cytoskeleton adhesion". *Journal of Cell Science*, 2001. **114**: p. 3759-3766.

180. Dai, J. and M.P. Sheetz, "Membrane Tether Formation from Blebbing Cells". *Biophysical Journal*, 1999. **77**(6): p. 3363-3370.
181. Hochmuth, R.M., N. Mohandas, and P.L. Blackshear, "Measurement of the Elastic Modulus for Red Cell Membrane Using a Fluid Mechanical Technique". *Biophysical Journal*, 1973. **13**: p. 747-762.
182. Hwang, W.C. and R.E. Waugh, "Energy of dissociation of lipid bilayer from the membrane skeleton of red blood cells". *Biophysical Journal*, 1997. **72**: p. 2669-2678.
183. Shao, J.Y. and R.M. Hochmuth, "Micropipette suction for measuring piconewton forces of adhesion and tether formation from neutrophil membranes". *Biophysical Journal*, 1996. **71**: p. 2892-2901.
184. Waugh, R.E., A. Mantalaris, R.G. Bauserman, W.C. Hwang, and J.H.D. Wu, "Membrane instability in late-stage erythropoiesis". *Blood*, 2001. **97**(6): p. 1869-1875.
185. Dai, J. and M.P. Scheetz, "Mechanical properties of neuronal growth cone membrane studied by tether formation with laser optical tweezers". *Biophysical Journal*, 1995. **68**: p. 988-996.
186. Li, Z., B. Anvari, M. Takashima, P. Brecht, J.H. Torres, and W.E. Brownell, "Membrane Tether Formation from Outer Hair Cells with Optical Tweezers". *Biophysical Journal*, 2002. **82**(3): p. 1386-1395.
187. Xu, G. and J.Y. Shao, "Double Tether Extraction from Human Neutrophils and its Comparison with CD4+ T Lymphocytes". *Biophysical Journal*, 2005. **88**: p. 661-669.

188. Derényi, I., F. Jülicher, and J. Prost, "Formation and Interaction of Membrane Tubes". *Physical Review Letters*, 2002. **88**(23): p. 238101.
189. Cuvelier, D., I. Derényi, P. Bassereau, and P. Nassoy, "Coalescence of membrane tethers: experiments, theory, and applications". *Biophysical Journal*, 2005. **86**: p. 2714-2726.
190. Koster, G., M. VanDuijn, B. Hofs, and M. Dogterom, "Membrane tube formation from giant vesicles by dynamic association of motor proteins". *Proceedings of the National Academy of Science of the United States of America*, 2003. **100**: p. 15583-15588.
191. Powers, T.R., G. Huber, and R.E. Goldstein, "Fluid-membrane tethers: Minimal surfaces and elastic boundary layers". *Physical Review E*, 2002. **65**: p. 041901.
192. Benoit, M., D. Gabriel, G. Gerisch, and H. Gaub, "Discrete interactions in cell adhesion measured by single-molecule force spectroscopy". *Nature Cell Biology*, 2000. **2**: p. 313-317.
193. Benoit, M. and H. Gaub, "Measuring cell adhesion forces with the atomic force microscope at the molecular level". *Cells Tissues Organs*, 2002. **172**(3): p. 174-189.
194. Edgell, C.-J.S., C.C. McDonald, and J.B. Graham, "Permanent cell line expressing human factor VIII-related antigen established by hybridization". *Proceedings of the National Academy of Science of the United States of America*, 1983. **80**: p. 3734-3737.
195. Coue, M., S.L. Brenner, I. Spector, and E.D. Korn, "Inhibition of actin polymerization by latrunculin A". *FEBS Letters*, 1987. **213**(2): p. 316-318.

196. Spector, I., N.R. Shochet, D. Blasberger, and Y. Kashman, "Latrunculins-novel marine macrolides that disrupt microfilament organization and affect cell growth: I. Comparison with cytochalasin D". *Cell Motility and the Cytoskeleton*, 1989. **13**(3): p. 127-144.
197. Yarmola, E.G., T. Somasundaram, T.A. Boring, I. Spector, and M.R. Bubb, "Actin-Latrunculin A Structure and Function". *The Journal of Biological Chemistry*, 2000. **275**(36): p. 28120-28127.
198. Kijima, Y., E. Ogunbunmi, and S. Fleischer, "Drug Action of Thapsigargin on the Ca²⁺ Pump Protein of Sarcoplasmic Reticulum". *The Journal of Biological Chemistry*, 1991. **266**(34): p. 22912-22918.
199. Moore, T.M., G.H. Brough, P. Babal, J.J. Kelly, M. Li, and T. Stevens, "Store-operated calcium entry promotes shape change in pulmonary endothelial cells expressing Trp1". *American Journal of Physiology*, 1998. **275**: p. L574-L582.
200. Evans, E. and F. Ludwig, "Dynamic strengths of molecular anchoring and material cohesion in fluid biomembranes". *Journal of Physics: Condensed Matter*, 2000. **12**: p. A315-A320.
201. Allain, J.-M., C. Storn, A. Roux, M. Ben Amar, and J.-F. Joanny, "Fission of a Multiphase Membrane Tube". *Physical Review Letters*, 2004. **93**(15): p. 158104-1 - 158104-4.
202. Sun, M., J.S. Graham, B. Hegedüs, F. Marga, Y. Zhang, G. Forgacs, and M. Grandbois, "Multiple Membrane Tethers Probed by Atomic Force Microscopy". *Biophysical Journal*, 2005. **(submitted)**.

203. Lee, C.-H., C.-L. Guo, and J. Wang, "Optical measurement of the viscoelastic and biochemical responses of living cells to mechanical perturbation". *Optics Letters*, 1998. **23**(4): p. 307-309.
204. Evans, E. and K. Ritchie, "Dynamic strength of molecular adhesion bonds". *Biophysical Journal*, 1997. **72**: p. 1541-1555.
205. Evans, E. and A. Yeung, "Hidden dynamics in rapid changes of bilayer shape". *Chemistry and Physics of Lipids*, 1994. **73**: p. 39-56.
206. Rotsch, C. and M. Radmacher, "Drug-Induced Changes of Cytoskeletal Structure and Mechanics in Fibroblasts: An Atomic Force Microscopy Study". *Biophysical Journal*, 2000. **78**: p. 520-535.
207. Chiappuis-Flament, S., E. Wong, L.D. Hicks, C.M. Kay, and B.M. Gumbiner, "Multiple cadherin extracellular repeats mediate homophilic binding adhesion". *The Journal of Cell Biology*, 2001. **154**: p. 231-243.
208. Critchley, D.R., "Focal Adhesions-the cytoskeletal connection". *Current Opinion in Cell Biology*, 2000. **12**: p. 133-139.
209. Cui, S., C. Liu, and X. Zhang, "Simple Method to Isolate Single Polymer Chains for the Direct Measurement of the Desorption Force". *Nano Letters*, 2003. **3**(2): p. 245-248.
210. Alfonso, A., Y. Román, M.R. Vieytes, K. Ofuji, M. Satake, T. Yasumoto, and L.M. Botana, "Azaspiracid-4 inhibits Ca^{2+} entry by stored operated channels in human T lymphocytes". *Biochemical Pharmacology*, 2005. **69**: p. 1627-1636.

211. Redondo, P.C., G.M. Salido, J.A. Pariente, and J.A. Rosado, "Dual effect of hydrogen peroxide on store-mediated calcium entry in human platelets". *Biochemical Pharmacology*, 2004. **67**: p. 1065-1076.

212. Treiman, M., C. Caspersen, and S.B. Christensen, "A tool coming of age: thapsigargin as an inhibitor of sarco-endoplasmic reticulum Ca²⁺-ATPases". *Trends in Pharmacological Sciences*, 1998. **19**: p. 131-135.

VITA

John Stephen Graham was born on November 26, 1965, in Kansas City, Missouri. He earned B.S. Degrees in Biochemistry and Physics at the University of Missouri-Columbia in 1998. He went on to earn his Doctorate in Biological Physics also from the University of Missouri-Columbia in 2005. After earning his Doctorate, he joined the group of Dr. John Marko at the University of Illinois-Chicago as a Postdoctoral Fellow.